Evolution of Coupled Hydrodynamic and Bed Instabilities

by

Özgür Güngördü and James T. Kirby

RESEARCH REPORT NO. CACR-01-04
July, 2001

Center for Applied Coastal Research
University of Delaware
Newark, DE 19716

Acknowledgements

This document was submitted to the University of Delaware by the first author as a thesis for the degree of Master of Civil Engineering. This work has been supported by the Coastal Dynamics Program of the Office of Naval Research, Grant N00014-99-1-0398.

Abstract

This thesis describes a hydrodynamic model extended with sediment transport capability in order to study bedform changes on time scales up to several days. The hydrodynamic model treats the nonlinear shallow water equations, and the sediment transport equation used is a basic formula relating the current velocity raised to some power to the volumetric sediment transport rate. The bottom change is computed through a standard sediment conservation equation.

This coupled model is mainly used to study the evolution of rhythmic topographic bed forms in a rectangular channel with nonerodible side banks. The onset of the topographic instabilities is achieved by initially introducing perturbations to the bed. A linear stability analysis of the flow field and bed forms for the rectangular channel case is presented. The initial channel geometry and bed perturbations are chosen according to the results obtained from this analysis. The resulting wave number to frequency relations provide information on the growth/decay and propagation speed of the bed forms within the finite amplitude limit. The numerical results reveal information beyond this limit for more complicated flow structures.

Parameters like the bottom friction coefficient, the power of the velocity in the sediment transport equation, or the channel width-to-depth ratio affect the results significantly. These are discussed considering both the analytical linear stability analysis along with results from previous related studies, and also the results from the current numerical model.

Results are compared to laboratory data, which are discussed qualitatively.

The model is also used for a planar beach geometry, with forcing terms in the hydrodynamic part appropriate for the coastal region. These results are compared to related analytical results and field observations.

Further improvements of the model for a truly representative surfzone morphology requires the utilization of a sediment transport equation which can represent wave-dominated cross-shore processes as well. The improvements and the problems associated with the inclusion of such a formulation are all discussed along with some preliminary results. The applicability of the current coupled model is discussed considering the sediment transport equation used and also numerical issues which are related to the stability of the code and the computational power required.

Contents

List of Figures

Chapter 1

INTRODUCTION

Morphodynamics in any flow environment depends on complex, mostly nonlinear processes including currents, waves in the coastal region, and sediment transport all interacting with each other. This interaction results in the change of the bottom topography. Flow field patterns both in the coastal region and river environment are generally associated with rhythmic topographic features. There exists a constant feedback between the flow field and bottom. Considering basic steady conditions, it is not possible to describe these patterns observed in nature. Some perturbation in the flow field, or in the topography causes the onset of irregularities not found for basic equilibrium cases. A small gap dividing two bars in the surf zone may act as a perturbation causing the formation of rip currents commonly observed in the field. The meandering of alongshore or along river currents can be associated with transverse/oblique bar formations, cresendic bars, or ridge and runnel systems.

Analytical studies on the interaction between the flow and the bed are generally based on stability analysis type of investigations. The momentum and mass conservation equations are used to describe the flow in a two-dimensional-horizontal domain. The analysis of instabilities of only the flow field over a nonerodible bed can be extended by the inclusion of the interaction between the flow and the bottom through a sediment transport and a sediment conservation equation. Due to the complex physics involved, the sediment transport equations used are fairly simple. They usually relate the volumetric sediment transport rate to the current velocity raised to some power. Although useful in investigating the initial growth stages of the perturbations, a stability analysis is only valid in the small amplitude limit and may not reveal details about the geometric form of features which have reached large amplitude. More complicated flow and sediment transport patterns require a more complete treatment of the problem. This, in turn, requires a direct numerical approach of solving the combined governing equations.

The mechanisms behind hydrodynamic processes are fairly well understood. Numerical modeling of these processes using the depth and time averaged momentum and mass conservation equations are very common both in research areas and engineering practice. The physical understanding of sediment transport and it's relation to hydrodynamics, however are still not that well established. Although based on physical grounds, many sediment transport formulations involve some empirically adjusted factors due to the fact that the

whole process is physically very complicated. Hence, as stated in the previous paragraph, sediment trasnport equations are mostly simple relations between the flow velocity and the sediment transport rate.

1.1 Instabilities of the flow field

Alongshore or along river currents can be considered as a two dimensional horizontal flow since they are generally weakly dependent on depth. It is known that these flows can show unstable features such as meandering. The meandering of longshore currents with very high periods, showing behavior beyond the gravity wave limit, was first observed by Oltman-Shay *et al.* (1989) during the SUPERDUCK field experiment. Several studies analyzing this unstable behaviour followed, and different features of this instability were investigated.

The analytic study by Bowen and Holman (1989) showed that the shear instability of the mean longshore current can reproduce the meandering nature of the observed motions, referred to as shear waves. This analysis was carried out for a simplified current profile applied over a constant depth.

In a numerical study by Putrevu and Svendsen (1992) a similar analysis was done for a more realistic current profile and bottom topography. The results show that the topography is an important factor, and that the presence of a bar enhances the strength of the instability. The dispersion relationship found for the shear waves is almost linear and it is rather unaffected by the topography.

Falqués and Iranzo (1994) performed another numerical study for vorticity waves arising from the same shear instability of the mean current. Their method allowed for an arbitrary current profile and bathymetry, but remaining constant alongshore. Their results agreed with the ones by Bowen and Holman (1989) for the simplified case, but the details in the flow profile and bathymetry were found to significantly affect the instability process. The eddy viscosity and friction factor were also found to be affecting the wavenumber span and growth rate of the instabilities. Certain constant eddy viscosity values and realistic values of the Chezy coefficient were able to remove the entire instability.

A similar more recent analysis by Allen *et al.* (1996) revealed properties of the propagating finite-amplitude shear waves that are not directly related to linear theory. Their results depend on a dimensionless parameter Q which is the ratio of an advective to a frictional time scale. For certain small values of Q corresponding to a higher frictional time scale the disturbances equilibriated with constant amplitude. For larger values corresponding to a lower frictional time scale the disturbances equilibriated with time-varying amplitude.

Özkan-Haller and Kirby (1999) performed a series of numerical simulations of shear waves, with the main goal of studying the long-time nonlinear behavior of shear instabilities of the longshore current over a plane and barred beach (see also Özkan-Haller, 1997). The nonlinear shallow water equations including bottom friction and lateral mixing were used.

Their results for a plane beach show that the initial development of the instabilities is dominated by vortex collision and pairing events. The flow structure exhibits offshore directed velocity vectors with an alongshore propagation at a fraction of the longshore peak

current, which suggests the presence of migrating rip currents. Similar vortex collisions were found in the barred beach results. The vortices are frequently shed offshore in this case, suggesting transient rip current motions.

Although the alongshore length scales of the fluctuations were unaffected by the value of the friction factor, more energetic fluctuations were associated with a lower value. The mixing coefficient had almost no effect on the propagation speed of the shear waves, but caused longer alongshore length scales together with weaker vorticies. They found that in general, lateral mixing caused by shear waves is of comparable magnitude to mixing caused by turbulence or Taylor dispersion.

For alluvial channels, stability analysis studies are generally directly in conjunction with the resulting channel geometry. Although there are studies solely on the general flow instability; the main concern is it's relation to sediment transport and the resulting bed forms in the channel.

1.2 Instabilities of the bed

The extension of the general hydrodynamic stability problem with a sediment transport and sediment conservation equation provides information on the behavior of the resulting bed perturbations and their interaction with the flow. This approach is the most general form of stability analysis performed considering morphodynamic processes.

The mechanics of dunes and antidunes in channels for potential flow was addressed by Kennedy (1963). Considering a two-dimensional-vertical channel he used an analytic model of free-surface flow over an erodible bed. His results show that the type, wavelength and propagation velocity of bed forms depend on the Froude number, the flow depth, and the phase lag between the local sediment transport and local velocity, as well as the sediment transport rate itself.

River environments provide examples of large amplitude bed features, such as alternating bar configurations. Flume experiments by Chang *et al.* (1971) show that alternating sand bars often observed in nature can be reproduced experimentally in straight laboratory flumes. They also point out the significant relation between alternate bar formation and river meandering. They observed that the width-depth ratio of the channel is an important factor for the formation of bars.

The stability theory developed by Fredsøe (1978) identifies if the river meanders, braids or remains straight depending on the channel width-to-depth ratio, without putting much emphasis on the resulting channel geometry. The study done by Parker (1976) stresses the existence of sediment transport and friction for the occurrence of flow and bed instabilities.

The development of alternate bars in straight channels was investigated analytically by Colombini *et al.* (1987) based on a standard linear and weakly nonlinear stability analysis. Their model shows that nonlinear effects inhibit indefinite growth leading perturbations to reach an equilibrium amplitude, and also that the development of higher harmonics tends to cause diagonal fronts with high downstream steepness. A critical channel width is identified below which no bars form, and quantitatively satisfactory predictions of the maximum bar

height for a wide range of channel width values were presented. The analysis carried out by Schielen *et al.* (1993) follows closely the work of Colombini *et al.* and extends the weakly nonlinear part. Schielen *et al.* derived a Ginzburg-Landau equation which describes the nonlinear evolution of the envelope amplitude of the group of unstable alternate bars by allowing for spatial modulations due to wave packet dispersion. They demonstrated that the periodic bar pattern can become unstable, exhibiting quasi-periodic behavior for realistic physical parameters and a dune covered channel bed.

A more recent numerical study on the formation of alternate bars by Takebayashi *et al.* (1999) focuses on the effect of sediment sorting on the resulting sand bars. They found that sediment sorting suppresses bar height formed on non-uniform sediment and also that wavelength and migration velocity can be significantly affected by uniform and non-uniform sediment.

Similar instabilities are also found in the coastal region. Field observations done by Sonu (1972) demonstrated that undulations of the surf-zone bed were an essential condition to the formation of circulation and meander. Sonu (1973) also presented a series of field observations in which he studied three dimensional beach changes. He concluded that rythmic topography exhibit periodic variations parallel to the coastline and that these undulations have characteristics analogous to those of sand waves found in alluvial channels. Sonu also stressed that an erodible bed coupled with a current can develop an instability in which any disturbance of the bed modifies the longitudinal distribution of sediment transport, causing the growth and propagation of the bed deformation. A two year dataset of daily sand bar morphology estimates from Duck, N.C., presented by Lippmann and Holman (1990) resulted in an eight-bar-type classification scheme representing the morphologic variability of nearshore sand bars observed at the site. The most common form was unstable longshore-periodic bars. The most stable form was shore attached cresentic bars, and non-rythmic three-dimensional bars were very transient.

Deigaard *et al.* (1994) presented a numerical simulation study of shear waves and the corresponding sediment transport, using the hydrodynamic model MIKE-21. Rather than the resulting bed formations, this study addressed the effectiveness of shear waves in the cross-shore momentum exchange, how they reduce the longshore sediment transport, and cause cross-shore transport. A similar study by Christensen *et al.* (1994) focused on the stability of large scale periodic bottom topographies on a straight and uniform beach. Emphasis was made on the description of sediment transport and the effect of the bed slope on bed load transport. A standard perturbation analysis was performed. Results show that the bed slope affects the kind of topography that emerges and the spacing of the rips that form. The inclusion of suspended load was found to decrease these spacings for large incident wave angles, and the phase lag of suspended load gives smaller growth rates. The stabilizing effects were found to be the bed slope, large grain size and the phase lag of suspended transport load; whereas the destabilizing effects were the longshore current and the modification of the wave field due to the perturbed bed. A more recent study by Deigaard *et al.* (1999) considered the morphological instability for a long straight barred beach. This analysis can be considered as an extension to the previous two studies. Deigaard *et al.* found that the instability is closely related to the cross-shore flow at the bar crest where a tendency of deposition occurs. The instabilites concentrated around the bar form rip channels, and

the alongshore spacing of the rip channels is affected by the flow resistance and horizontal momentum exchange.

Similar to the study by Schielen *et al.*, a more standard linear stability analysis for the coastal region was presented by Falqués *et al.* (1996a). An initially uniform longshore current on a plane erodible beach was considered. The growth rates and dominant unstable mode of the bed perturbations mainly depend on the parameter R which is the ratio of bottom friction to beach slope. Instability increases for higher values of R forming a simple transverse bar pattern; higher values produce a more complicated pattern consisting of bumps and holes, and downcurrent oriented oblique bars. The growth rates depend on R, the beach slope and the maximum Froude number. Results show that the most complex behavior occurs for mildly sloped beaches. In this analysis Falqués *et al.* considered bed-flow instability only, in which the perturbations were not affecting the wave field, or more specifically the forcing terms in the momentum equations. In another study, Falqués *et al.* (1996b) considered also bed-surf instability in which the wave field is perturbed as well. Depending on the incoming wave angle and wave height the results with bed-flow instability are generally more complex and show a more complicated pattern, whereas for bed-surf instability a smoother and simpler pattern evolves. Although causing a smoother bar pattern, they conclude that bed-surf instability has the most de-stabilizing effect. Clearly, more research is needed to clarify all these mechanisms in a more conclusive way. A recent and similar study on the mechanism for the generation of wave-driven rhythmic surf zone patterns can be found in Falqués *et al.* (2000). Using the same instability analysis Falqués *et al.* (1998) also performed a study on the morphodynamic evolution of shoreface-connected ridges by considering large scale behaviour of the proces.

Most of the analytical studies trying to describe features of these formations are generally addressing one particular configuration within the finite amplitude limit and do not really describe the change from one configuration to another, as observed by Lippmann and Holman (1990) for example. Even weakly nonlinear stability analyses are valid for basic flow conditions and bathymetry. This is due to the complexity of the whole process, and a description of such a configuration change would require a numerical treatment of the whole problem.

Similar to the analysis by Kennedy (1963), but without the potential flow assumption, there are also other recent studies considering a two-dimensional-vertical system for large-scale bed forms in tidal seas. These are also based on a standard stability analysis. The model by Hulscher (1996) shows how tidal currents form wave-like bottom patterns. According to Hulscher the inclusion of vertical flow structure is the most crucial part for the formation of all known large-scale bed features. A nonlinear analysis of the same problem is presented by Komarova and Hulscher (2000), where linear instability and nonlinear coupling between long sand banks and sand waves are shown to be the two mechanisms responsible for the growth of these bed forms.

A recent extensive review on the mechanics of offshore and nearshore rhythmic bed-forms based on a standard stability theory can be found in the study by Blondeaux (2001). This review includes some of the above cited studies as well as other closely related work.

1.3 Present Study

The main goal is to develop a morphology model which can be used to study bedform changes on time scales up to several days. Focus is on the interaction between the flow and the bed instabilities and the resulting topography. A basic movable bed model is coupled with the hydrodynamic code of Özkan-Haller and Kirby (1997). The approach is to carry out numerical simulations using the coupled model, using also information obtained from a stability analysis related to the specific cases. This approach is similar to the one by Özkan-Haller and Kirby, the only difference is that the problem is now extended with sediment transport and a changing bottom.

A discussion of the related linear stability analysis follows in the next chapter. The analyses by Schielen *et al.* (1993) and Falqués *et al.* (1996a) are briefly discussed. Results of some cases are also presented.

A detailed derivation of the linear dispersion relation for an one-dimensional and two-dimensional channel is presented in Chapter 3, as part of the stability analysis of the present work. Results are presented in the form of dispersion curves for different parameters involved in the derivation.

In Chapter 4 a review of the hydrodynamic code used in this study is presented. The governing equations, the inclusion of sediment transport and the numerical method used in the model are discussed with emphasis on the capabilities of the coupled model.

Numerical results and comparisons for a rectangular channel case and plane beach are discussed in Chapter 5 and 6, respectively. The inclusion of an extended sediment transport model and preliminary results are presneted in Chapter 7. Conclusions of this study with suggestions for improvements of the model for future work are summarized in Chapter 8.

Chapter 2

INSTABILITY OF FLOW COMBINED WITH AN ERODIBLE BOTTOM

A two-dimensional flow is considered stable if it does not change drastically with small disturbances that are always present in the natural environment. If the flow field undergoes a transition from laminar to turbulent flow this is associated with an instability mechanism. In this case, the mean flow changes and shows variations in time as the small disturbances grow. Considering the strong relation between the flow and the bottom, it is obvious that any instability of the flow can also affect the bottom change in a similar way, and vice versa.

In order to study this instability, the equations describing the flow and the sediment transport process are combined. The equations for the flow are the standard depth- and wave-averaged momentum equations, and the mass conservation equation. These are combined with a sediment transport equation, usually relating sediment transport flux to the flow velocity; and a sediment conservation equation with which the actual bottom change can be computed. If the basic flow state consisting of a stable longshore or along channel flow becomes unstable to wave like perturbations in the flow itself or in the bottom topography, the perturbations grow and can be observed as finite amplitude undulations of the flow and the topography. A linear stability analysis reveals this phenomena, but once the perturbations have reached finite amplitude a nonlinear stability analysis is required.

In this chapter we present an overview of a standard linear and weakly nonlinear stability analysis. The theory by Schielen *et al.* (1993) is presented. This is followed by the stability analysis Falqués *et al.* (1996a, 1996b) performed for a plane beach.

2.1 Instability Theory for a Straight Channel

Schielen *et al.* (1993) consider a simple morphological model describing the interaction between an unidirectional flow and an erodible bed in an infinitely long straight channel with a mild along channel slope. A standard coordinate system is chosen, where the x coordinate

points along channel, the y coordinate across channel and the z coordinate in the vertical direction. The channel width and undisturbed water depth are y_* and h_*, respectively. The situation is depicted in Figure 2.1.

The channel width is assumed to be much larger than the undisturbed water depth and bar amplitudes developing in the bottom are considered to be much smaller than the characteristic horizontal length scales. With these assumptions any boundary layer development along the sidewalls or at the bottom, as well as flow separation due to the resulting bed forms can be neglected. Therefore a depth-averaged model is considered.

The momentum and mass conservation equations then become

$$\frac{\partial \mathbf{u}}{\partial t} + (\mathbf{u} \cdot \nabla)\mathbf{u} + g\nabla\eta = F,$$

$$\frac{\partial d}{\partial t} + \nabla(\mathbf{u}d) = 0 \tag{2.1}$$

As shown in Figure 2.1, $\mathbf{u} = (u + U, v)$ is the depth-averaged velocity, with u and v being the perturbed velocities and U being the basic, steady along channel flow velocity; η is the perturbed free surface, z_b is the disturbed bed level, and $d = \eta + h_* - z_b$, is the total depth. F represents the forcing and friction terms, defined as

$$F = \left(-C\frac{(u+U)((u+U)^2 + v^2)^{1/2}}{d} + i_o g, \qquad -C\frac{v((u+U)^2 + v^2)^{1/2}}{d} \right) \tag{2.2}$$

where $C = g/C_f^2$ is the drag coefficient, g is the gravitational acceleration, and C_f is the Chezy coefficient. Note that the terms including the drag coefficient are frictional terms and the other term is the actual forcing. i_o is the along channel slope.

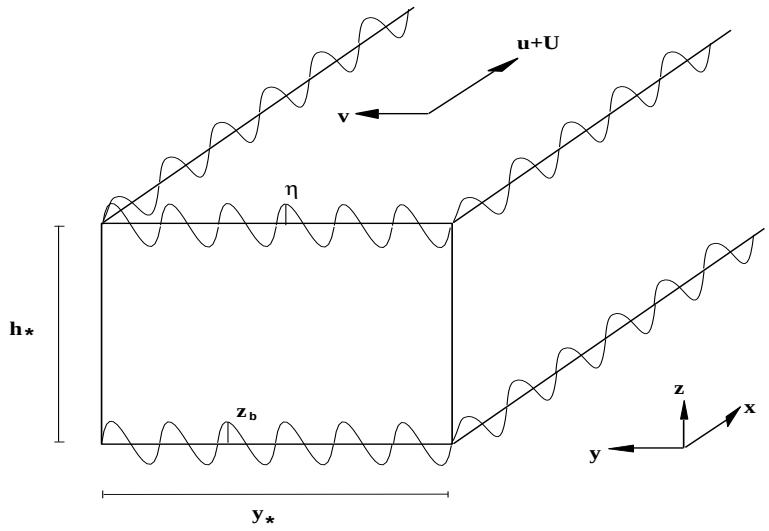

Figure 2.1: Sketch of the physical layout: rectangular channel.

Sediment transport is assumed to occur only as bed load transport which is a function of the local flow parameters. The volumetric transport rate $\mathbf{q}$ is modeled as

$$\mathbf{q} = \nu_o |\mathbf{u}|^b \left(\frac{\mathbf{u}}{|\mathbf{u}|} - \gamma' \nabla z_b \right) \tag{2.3}$$

Here $b > 0$, and $\gamma' \nabla z_b$ accounts for the tendency of downslope sand movement, where γ' is usually of order 1. Values of b range between 2 and 7. The coefficient ν_o depends on the sediment characteristics and can only be determined empirically. It is important to note that the porosity effect is included in this coefficient and therefore it is not necessary to include it in the conservation equation described next.

The model is closed with a sediment transport conservation equation (2.4) and appropriate boundary conditions (2.5)

$$(1 - n) \frac{\partial z_b}{\partial t} = \nabla \cdot \mathbf{q} \tag{2.4}$$

$$v = 0, \;\; q_y = 0 \;\; on \;\; y = 0, \; y_* \tag{2.5}$$

where the subscript y denotes the transport component in the that direction. The coefficient n is the bed porosity. When this equation is divided by $(1 - n)$ the bed porosity can be absorbed in the coefficient ν_o. From here on ν_o is replaced by ν which includes bed porosity. With these boundary conditions the sidebanks are assumed to be impermeable and non-erodible.

After scaling equations (2.1)-(2.5), this system can be simplified with a 'quasi-steady' flow and a 'rigid-lid' assumption. According to the quasi-steady flow assumption, the flow instantaneously adjusts itself with the evolving bed. This means that the hydrodynamic time scale y_*/U is much smaller than the morphological time scale $\frac{y_* h_*}{\nu U^b}$, so any flow instability with a smaller time scale which may evolve due to some other mechanism is not resolved in this system. The flow instabilities are majorly due to only the bed perturbation. The rigid-lid assumption neglects terms containing small Froude number values, $U/(gh_*)^{1/2}$. Low Froude numbers are generally associated with river flows. With these two assumptions all time derivatives except for the sediment transport continuity equation; and terms which contain the Froude number can be dropped. The details of this derivation are presented in the next chapter.

The basic state of the linearized system is given as follows

$$(u_o, v_o, \eta_o, z_{bo}) = (U, 0, 0, 0) \tag{2.6}$$

where the subscripts denote terms at the basic state. This situation is also shown in Figure 2.1 where only the perturbed terms and the steady flow U are included. The steady along channel flow depends on the along channel slope i_o, the unperturbed channel depth h_* and on the friction factor C. Schielen *et al.* consider a fixed U value of 1 m/s. The channel geometry allows for along channel travelling wave solutions with some lateral structure, as given in the following form

$$\phi = f(y) e^{ikx + \omega t} + c.c. \tag{2.7}$$

where $f(y)$ stands for the perturbation amplitudes of the unknown terms; $u(y)$, $v(y)$, $\eta(y)$, $z_b(y)$. Here, k is a real valued wavenumber, ω is a complex frequency and $c.c$ denotes the complex conjugate.

After using (2.7) in the linearized equations, it is possible to reduce the system of equations to a fourth-order differential equation for the bottom perturbation z_b by a standard Gauss elimination procedure. This leads to equation (2.8), which has solutions of the form given in (2.9).

$$b_3 \frac{d^4 z_b}{dy^4} + (\omega a_2 + b_2) \frac{d^2 z_b}{dy^2} + (\omega a_1 + b_1) z_b = 0, \tag{2.8}$$

$$z_b(y) = A \cos p\pi y \tag{2.9}$$

The terms a_1, a_2, b_1, b_2 are combinations of k, γ', b, R (width-to-depth ratio of the channel), and C. These are shown in Chapter 3. A is an arbitrary amplitude, and p specifies the different modes of the solution. $p = 1$ is the first mode to become unstable (the situation of alternate bars).

This solution provides a dispersion relation for k and ω, where the real part ω_r determines the stability of this basic state. If ω_r is greater than zero for a certain range of k values, an unstable state occurs; for values smaller than zero the system is stable. This also leads to a critical value of the channel width-to-depth ratio R_c beyond which all perturbations are unstable. The imaginary part of ω describes the phase speed of the resulting bars. The derivation of this relation and examples of dispersion curves are presented in the next chapter.

Schielen *et al.* performed a perturbation analysis to obtain asymptotic expressions for R_c; the critical wavenumber k_c and corresponding frequency ω_c

$$\begin{aligned} R_c &= (\pi\gamma'/\beta)\delta^{-0.5}[1 + 2\delta^{0.5} + 4\delta + O(\delta^{1.5})], \\ k_c &= \sqrt{2}\pi\delta^{0.25}[1 + \frac{19}{4}\delta + O(\delta^{1.5})], \\ \omega_c &= -ik_c[1 + \beta\delta^{0.5} - 5\beta\delta + O(\delta^{1.5})] \end{aligned} \tag{2.10}$$

where $\delta = \frac{\gamma' C}{\beta}$, $\beta = b - 1$.

According to Schielen *et al.*, for realistic values of morphological parameters the R_c values range between 20 and 30, the k_c values between 5 and 15 channel widths, and wave periods range between 5 and 15 morphological time scales. An extensive study by Anderson *et al.* (1975) reports that for channels where braiding and meandering occurs R values can range from 3333 to 2.5, and the meander length which can be associated with k ranges from $1m$ to $30m$. The morphological time scale is a function of the flow, channel geometry and sediment parameters. Although the basic flow velocity and channel geometry can be measured, predicting the fricition factor, the coefficient ν and b is very difficult. For a $5m$ deep, $220m$ wide channel with a basic flow of $1m/s$, a friction factor of $c_f = 0.003$, and with fixed values of $\nu = 3.7 \times 10^{-4}$ and $b = 6$ the morphological time scale is slightly longer than a month, $T = 35$ days. In a laboratory experiment done by Schumm and Khan (1972), depending on the channel slope and flow characteristics this time scale can range from one hour to 24 hours.

The linear analysis describes features in the initial growth stages, where the wave amplitudes are small. The description of nonlinear dynamic behavior requires the consideration of interactions between various wave components. This analysis investigates behavior for wavenumbers (or width-to-depth ratios) which are slightly larger than the critical value. Therefore, this analysis is referred to as 'weakly' nonlinear and it only slightly extends the finite amplitude range.

Following a multiple scales analysis, a slow temporal and slow spatial scale is introduced allowing the amplitude A to vary slowly in time and space. This leads to an evolution equation for the amplitude, at third order. Since the whole procedure is mathematically very tedious, only the resulting evolution equation will be shown here

$$\frac{\partial A}{\partial \tau} = r(\tau_r + i\nu_r)A - \frac{1}{2}(\tau_{k^2} + i\nu_{k^2})\frac{\partial^2 A}{\partial \xi^2} + (c_r + ic_i)|A|^2 A \tag{2.11}$$

This equation is referred to as the Ginzburg-Landau equation. Here, A is the amplitude, τ is the slow temporal scale, ξ is the slow spatial scale. r is a value of order R_c and ensures that the analysis is within the weakly nonlinear limit (for values only slightly larger than R_c). The terms τ_r and ν_r measure the growth rate and the frequency shift of the perturbations, respectively. τ_{k^2}, ν_{k^2}, c_i, and c_r are lengthy terms depending on b, β, δ, and π.

Further analysis of the Ginzburg-Landau equation indicates that a fully periodic or quasi-periodic bed profile can evolve from an initially perturbed flat bed.

The same analysis can also be done by taking the amplitude as a constant, or only allowing for a slow temporal scale (Colombini *et al.*, 1987) and extending the linear theory to higher orders. An example of the resulting topography for the former case is shown in Figure 2.2. Note the steeper wave fronts caused by the superposition of the linear and the $O(\epsilon^2)$ approximations.

2.2 Instability Theory for a Planar Beach

Using the same procedure, a similar analysis can be carried out for the coastal region by changing certain features, like the bottom geometry or velocity profile. Falqués *et al.* (1996a) applied a linear stability analysis to a planar beach.

The governing equations are the same, except for the forcing terms in the momentum equations and an improvement made in the sediment transport equation

$$F_x = g\frac{d\zeta}{dx} \quad , \qquad F_y = c_d\frac{V^2}{d}, \tag{2.12}$$

$$\mathbf{q} = \nu(|\mathbf{u}| - v_c)^b \left(\frac{\mathbf{u}}{|\mathbf{u}|} - \gamma'\nabla z_b\right), \qquad if \quad |\mathbf{u}| > v_c \tag{2.13}$$

Accordingly, sediment transport is initiated only when the critical velocity, v_c is exceeded. c_d in equation (2.13) is the drag coefficient, and d is the undisturbed total depth. Note that the bottom shear stress is in the basic flow direction and the forcing in the x-direction

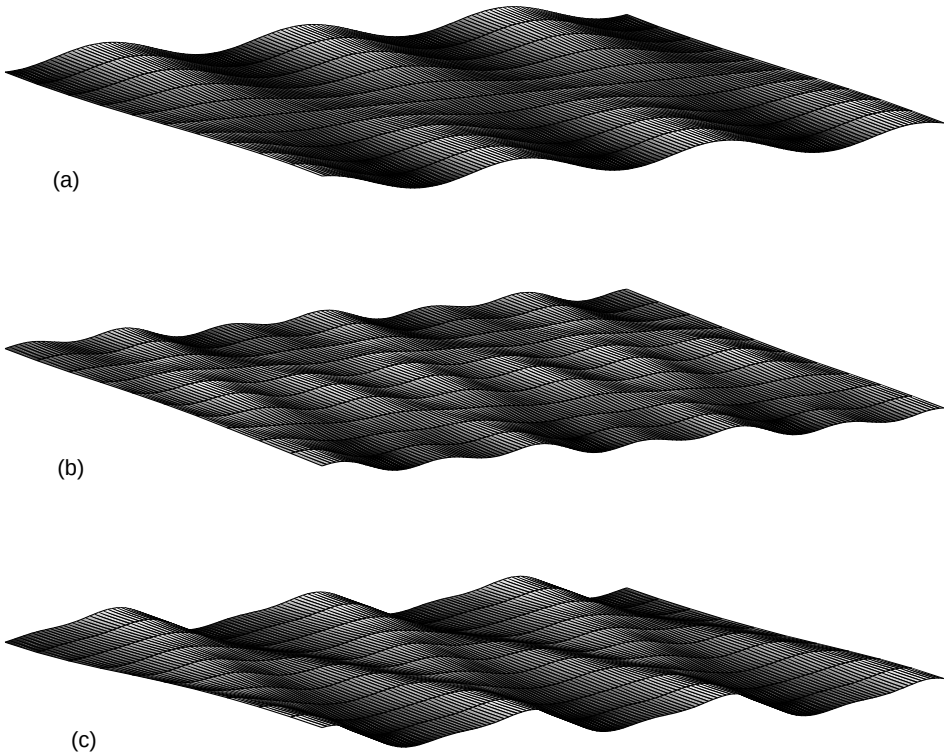

Figure 2.2: Bed profiles for $b = 6$, $C = 0.003$, $\gamma' = 1$, $A = 1$, $\epsilon = 0.35$. (a) $O(\epsilon)$ approximation, (b) $O(\epsilon^2)$ approximation, (c) superposition of $O(\epsilon)$ and $O(\epsilon^2)$ approximations. Profiles based on equations by Schielen *et al.* (1993).

(cross-shore direction) is directly balanced by the set-up/set-down, $\zeta = (d - h)$. Due to this balance ignoring set-up/set-down, the forcing in the x-direction can be directly set to zero, $F_x = 0$.

The longshore velocity profile is given by the following

$$V(x) = axe^{-nx} \tag{2.14}$$

This corresponds to a velocity profile which has a maximum of $U = a/(ne^1)$ at an offshore distance of $L = 1/n$. For this case an approximate surfzone width would be $x_b = 2L$. Falqués *et al.* assumed $a = e^1$, $n = 1$ for the dimensionless flow field, and a plane beach topography of the form $h(x) = mx$, where m is the bottom slope. The schematic for this case is shown in Figure 2.3.

Another important point to note is that no perturbations are allowed in the forcing terms. The forcing terms are steady and any instability in the flow field or bottom does not affect the forcing terms. Falqués *et al.* referres to this as 'bed-flow instability'. The opposite case where instabilities affect the forcing terms is referred to as 'bed-surf instability'.

In summary, the only differences from the channel case are: the domain geometry which is now a plane sloping beach with an open boundary at the offshore end, a basic flow profile with a transverse gradient, and a threshold velocity for the initiation of sediment

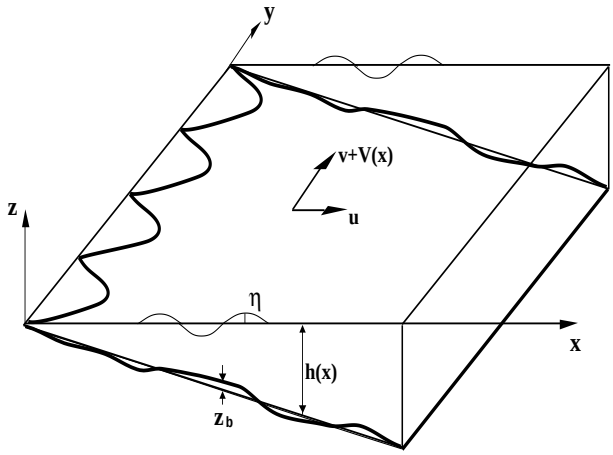

Figure 2.3: Sketch of the physical layout: plane beach

transport.

Scaling and perturbing the governing equations just as in the previous case, the resulting system again allows for alongshore travelling wave solutions

$$(u, v, \eta, z_b) = [\hat{u}(x), \hat{v}(x), \hat{\eta}(x), \hat{z_b}(x)]e^{i(ky-\omega t)} \tag{2.15}$$

Note that with this form, the imaginary part of the frequency governs growth or decay of the instabilities.

The morphodynamic time scale $mL^2/(\nu U^b)$ is again larger than the hydrodynamic time scale L/U and in this case the rigid-lid assumption is not made; therefore, the time derivatives can be dropped whereas terms that include the Froude number can be kept this time. For $L = 100m$, $U = 0.8m/s$, $m = 0.01$, $\nu = 0.1$ and $b = 2$, the hydrodynamic scale is $100s$ while the morphodynamic time scale is $1562.5s$. Shear waves or edge waves are filtered out of the system since motions with time scales smaller than the morphodynamic time scale are not included.

From the momentum equations it is possible to obtain equations for u, the longshore current velocity and v, the cross-shore current velocity as

$$\begin{aligned} u &= -\frac{1}{(ikV + RV/d)}\frac{\partial \eta}{\partial x}, \\ v &= \frac{1}{(ikV + 2RV/d)}\left[-u\frac{dV}{dx} + \left(Rf^2V^2/d^2 - ik\right)\eta - RV^2/d^2 z_b\right] \end{aligned} \tag{2.16}$$

The hats in the terms are dropped for convenience. Here, $f = U/\sqrt{gmL}$ is the Froude number, and $R = c_d/m$ is the controlling parameter of the instabilities. Using equations (2.17) with appropriate boundary conditions in the conservation equations an eigenvalue problem can be obtained

$$A(\eta, z_b) = i\omega B(\eta, z_b) \tag{2.17}$$

where ω is the eigenvalue and (η, z_b) is the eigenfunction. Here, A and B are linear operators including $\partial/\partial x$. Due to the solution form (2.15) for this case, growth of instabilities corresponds to $\omega_i > 0$. The appropriate boundary conditions are given by

$$\begin{aligned} \eta(\infty) &= 0, \qquad & z_b(\infty) &= 0, \\ \partial\eta(0)/\partial x &= 0, \qquad & z_b(0) &= 0 \end{aligned} \tag{2.18}$$

Here, ∞ corresponds to the offshore end of the domain where the perturbations vanish. The second boundary condition corresponds to the shoreline and can be shown by fluid and sediment conservation.

The system is solved numerically, therefore no explicit equation for the dispersion relationship is available. The numerical method is based on Chebyshev expansions and a collocation procedure. Details about this method can be found in Falquès *et al.* (1996a, 1996b).

Dispersion curves representing propagation and growth of the instabilities can be obtained for different modes, and different combinations of parameters. The general approach is to fix the maximum Froude number $F = \sqrt{e^1/2}f$, b, ν and v_c in the equations and obtain results for a range of realistic $R = c_d/m$ values. Typical values of R range between 0.1 and 1, and for F between 0.0 and 0.5. The power b of the velocity in the sediment transport equation is usually taken as 2, and the threshold velocity for transport v_c is set to $0.05U$. Different combinations of these values cause changes in the resulting dispersion relations (Figure 2.4). The resulting bed forms show increasing spatial complexity in the cross-shore with increasing mode number. This can be observed in Figure 2.5 where contour lines of the bed perturbations are shown. In this figure the most unstable wavenumbers k_M and corresponding imaginary frequencies σ_M are also shown. Examples of the resulting bed forms which consist of the basic slope plus the topographic instability, are shown in Figure 2.6. Note the alongshore periodic sand waves and the oblique orientation of the crests towards the offshore.

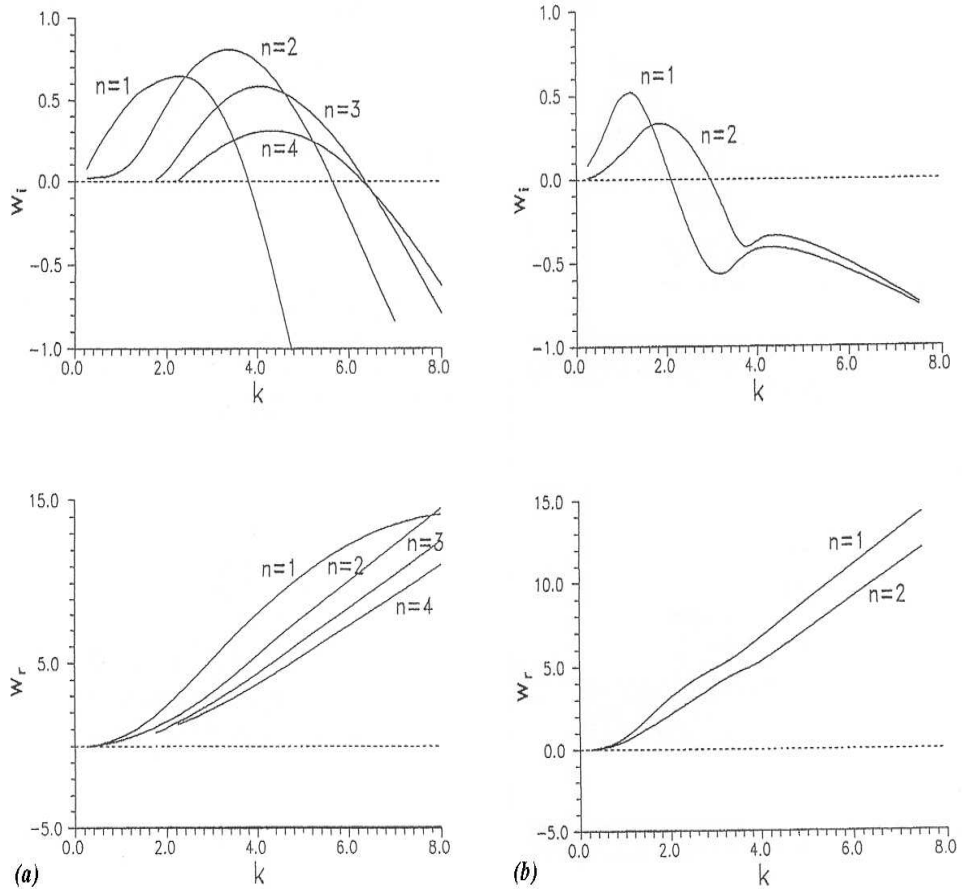

Figure 2.4: Dispersion curves, for different modes. $F = 0.3$, $m = 0.01$, (a) $R = 1$, (b) $R = 0.35$ (from Falquès *et al.*, 1996a).

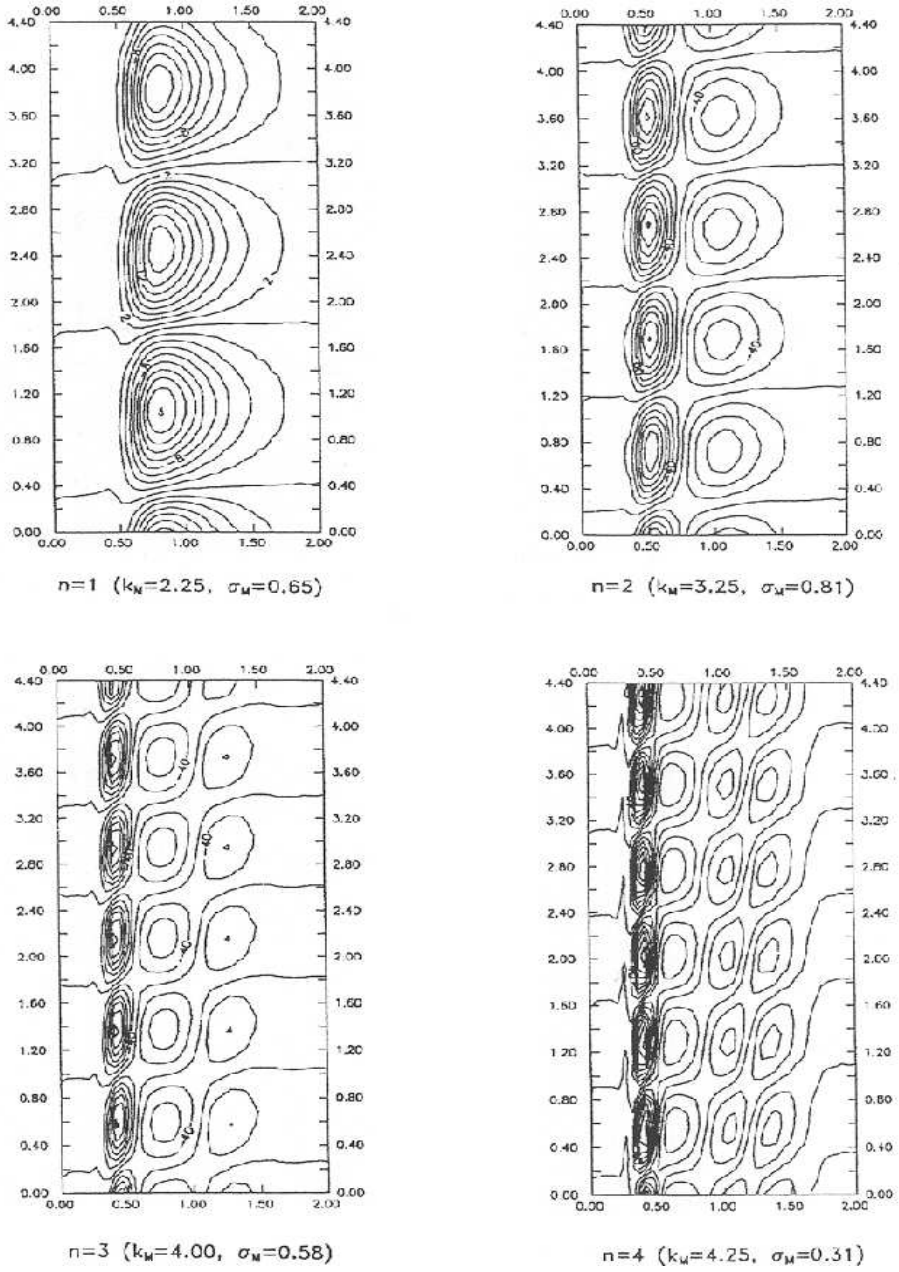

Figure 2.5: Contour lines of bed perturbation for modes 1,2,3 and 4. $R = 1$, $m = 0.01$, $F = 0.3$ (from Falquès *et al.*, 1996a).

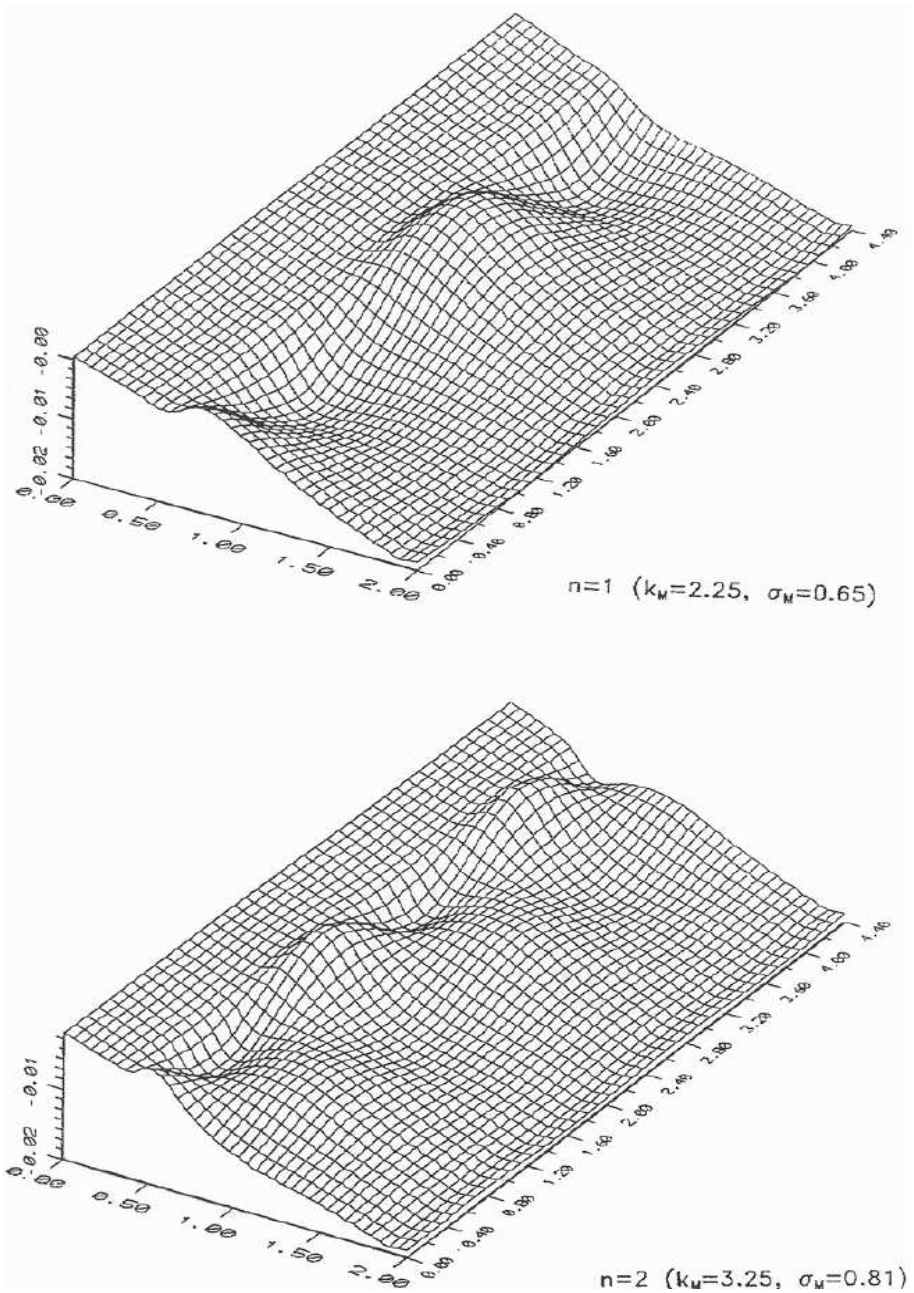

Figure 2.6: Bottom topography for modes 1 and 2. $R = 1$, $m = 0.01$, $F = 0.3$ (from Falquès *et al.*, 1996a).

Falqués *et al.* (1996b) also performed the same analysis considering bed-surf instabilities. For this case the forcing terms in the momentum equations are replaced with more realistic radiation stress terms following the solution by Longuet-Higgins and Stewart (1964). Lateral mixing terms are also included.

The momentum equation then becomes

$$\frac{\partial \mathbf{u}}{\partial t} + \mathbf{u} \cdot \nabla \mathbf{u} + g \nabla \eta - \frac{\tau_\mathbf{b}}{\rho d} - \tau_\ell = \frac{1}{\rho d} \nabla S \tag{2.19}$$

where, S is the radiation stress tensor and,

$$\tau_{\ell i} = \frac{1}{d} \sum_{j=1}^{2} \frac{\partial}{\partial x_j} \left[\nu_t d \left(\frac{\partial u_i}{\partial x_j} + \frac{\partial u_j}{\partial x_i} \right) \right], \qquad i = 1, 2$$

$$\tau_{bx} = -\frac{4}{\pi} \rho c_f u_o u, \qquad \tau_{by} = -\frac{2}{\pi} \rho c_f u_o v \tag{2.20}$$

Here, $x_1 = x$ and $x_2 = y$; also $\nu_t = N x \sqrt{gd}$ is the eddy viscosity, where N is a coefficient. The bottom friction terms are based on the weak current and small wave angle assumptions. In these terms, u_o is the maximum orbital velocity associated with the waves, which can be specified according to the wave theory used. For wave breaking a simple criteria relating wave height to total depth is assumed, $H = \gamma_b d$.

The continuity and the sediment transport equations are the same as before. The same perturbation analysis is performed on these equations.

For this case Falquès *et al.* refer to the perturbations in the radiation stress terms as bed-surf terms. Perturbations in the wave refraction have not been included in this study. Bed-flow terms are the rest of the terms when the bed-surf terms are neglected. In these studies the general definition of bed-surf instability and its difference from bed-flow instability is somewhat ambigious. Details on how the wave field and the corresponding radiation stress terms are computed, and how the instabilities enter these terms are not given.

Results point to an enhanced instability when bed-surf terms are considered. The dispersion curves do not show much change in the overall shape, but the growth rates increase significantly with bed-surf instabilities. The real part of ω is negative and of order one. This means that the bedforms are travelling against the current, showing an anti-dune regime. In the previous analysis where only bed-flow instabilites are considered (Falqués *et al.*, 1996a), all ω_r values are positive (Figure 2.4). In both these studies this difference is not addressed.

Two different types of bedforms can be identified from the results. These are referred to as current and wave dominated bedforms. In the first case the bars are upcurrent rotated and very oblique. They occur for relatively high Froude numbers, corresponding to a small R and a large incident wave angle at breaking, α_b. Including also bed-surf instabilites does not seem to cause significant changes in the resulting bottom perturbations. Figure 2.7 shows the evolved bottom topography for this case.

For wave dominated bedforms the effect of including bed-surf instabilities is more evident. With only bed-flow, the bedforms look very similar to transverse bars slightly upcurrent rotated (Figure 2.8), just like in the previous results shown in Figure 2.5 and 2.6.

The effect of bed-flow instabilities can be seen in Figure 2.9, where bottom perturbation contours are shown. Comparing Figures 2.5 and 2.9, bed-surf instability seems to cause a jump to a higher mode. Wave dominated bedforms occur for lower Froude numbers when R is larger and α_b is smaller.

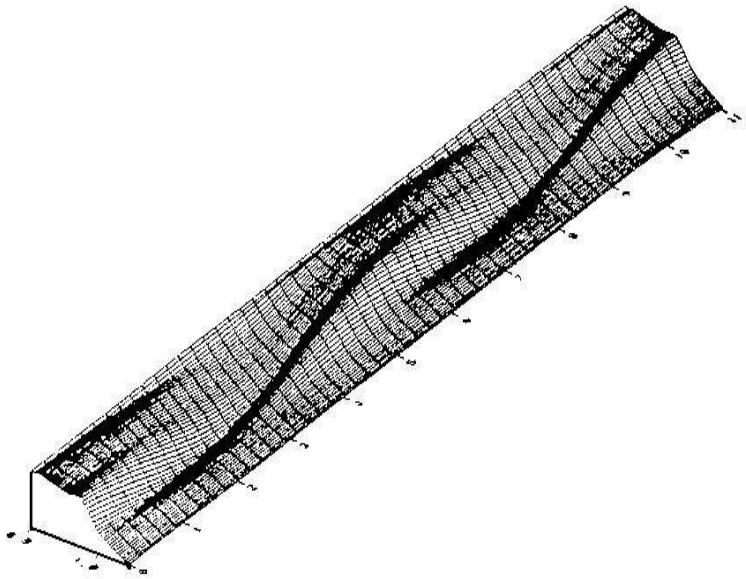

Figure 2.7: Current dominated bottom topography for $R = 0.1$, $\alpha_b = 12.3^o$, $N = 0.005$, $\gamma_b = 0.4$, $F = 0.8$, $k = 1.14$ (from Falqués *et al.*, 1996b).

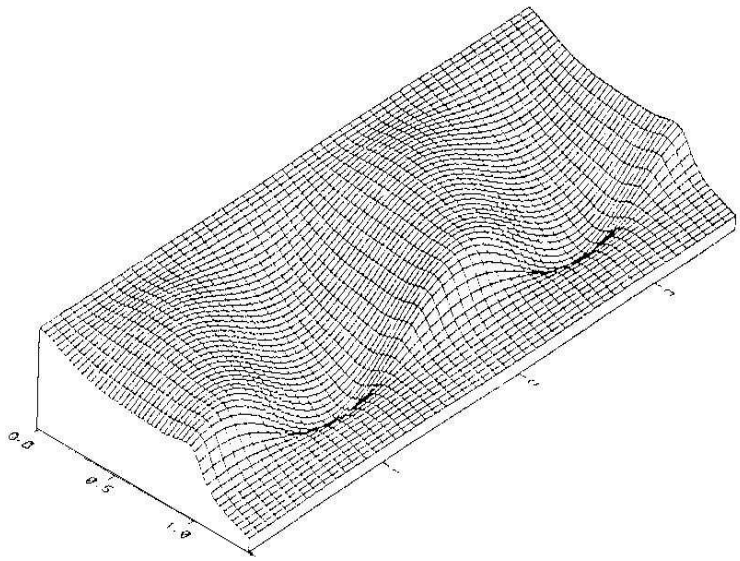

Figure 2.8: Wave dominated bottom topography for $R = 0.5$, $\alpha_b = 12.3^o$, $N = 0.005$, $\gamma_b = 0.4$, $F = 0.16$, $k = 3.5$ (from Falqués *et al.*, 1996b).

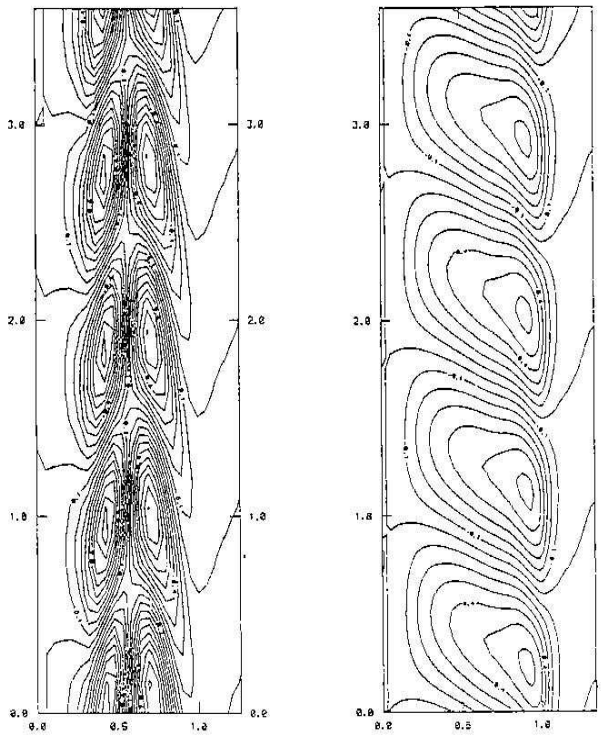

Figure 2.9: Contour lines of bed perturbation for $R = 0.5$, $\alpha_b = 12.3^o$, $N = 0.005$, $\gamma_b = 0.4$, $F = 0.16$, $k = 3.5$. Right: only bed-flow, left: bed-flow and bed-surf (from Falqués *et al.*, 1996b).

Falquès *et al.* have shown in these studies that a plane beach topography can be unstable due to interactions between the longshore current, incoming waves and the bed. The alongshore spacing of the resulting sand waves changes according to R, α_b, and N. The direct effect of N, namely the lateral friction mechanism has not been addressed in detail in these studies. The effect of the growing bedforms on the flow field is in the form of a meandering longshore current with an offshore deflection over the shoals. Considering rip currents, this may be in contrast with many observations. Since these results are for initial growth stages, after the perturbations have reached finite amplitude other nonlinear interactions may cause a different current behaviour.

Chapter 3

LINEAR DISPERSION RELATIONSHIPS FOR RECTANGULAR CHANNELS

This chapter contains a detailed derivation of the dispersion relationships discribing the growth and propagation of bottom instabilities in rectangular channels. Results which consist of dispersion and growth lines are also presented, and the effects of different parameters involved in the analysis are discussed. The theory outlined in the previous chapter is closely followed. The same equations for an arbitrary basic flow are used with a slightly improved transport equation.

First, the derivation for a one-dimensional channel is presented. This is followed by the derivation for a two-dimensional rectangular channel.

3.1 One-dimensional Channel

Ignoring any cross channel variation in a 2D (two-dimensional) channel, a 1D (one-dimensional) channel can be considered (Figure 3.1). For this case the momentum equation only for the x-direction is necessary, and the conservation equations reduce to 1D. Here, the transport equation is improved by including a threshold velocity, v_c for the initiation of transport; and the whole derivation is done for an arbitrary basic flow velocity, U. The equations are shown in the following

$$u_t + uu_x + g\eta_x = -c_f \frac{v^2}{d} + i_o g, \qquad d_t + (ud)_x = 0,$$

$$(z_b)_t + (q)_x = 0, \qquad q = \nu(u - v_c)^b (1 - \gamma'(z_b)_x); \qquad u > v_c \tag{3.1}$$

where $d = \eta - z_b + h_*$. Subscripts x and y denote derivatives in the corresponding directions. Note that the porosity effect is included in the coefficient ν as discussed in Chapter 2. The transport rate is zero for $u < v_c$.

The next step is to nondimensionalize the equations with appropriate physical scales: $u = U\hat{u}$, $z_b = h_*\hat{z_b}$, $x = x_*\hat{x}$, $\eta = \frac{U^2}{g}\hat{\eta}$, $t = \frac{x_* h_*}{\nu U^b}\hat{t} = T\hat{t}$.

Here the dimensionless parameters are presented with a hat sign $\hat{.}$; and x_* and T represent a characteristic channel length which is associated with the wavelength of the bedforms, and the morphological time scale, respectively. From the basic unperturbed case, $U^2 = i_o g h_*/c_f$.

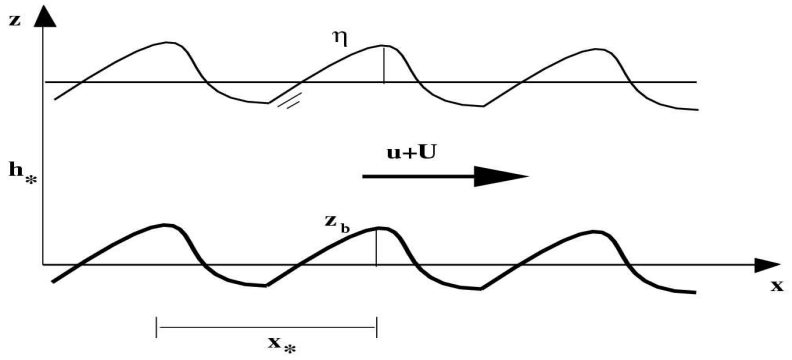

Figure 3.1: Sketch of the physical layout: 1D channel

The scaled equations are shown in the following with the hats dropped for convenience

$$\kappa u_t + u u_x = -\eta_x - c_f \frac{x_*}{h_*(F^2\eta - z_b + 1)} u^2 + \frac{c_f}{h_*} U^2,$$

$$\kappa \eta_t + u_x \eta - F^{-2} u_x (z_b - 1) + u\eta_x - F^{-2} u (z_b)_x - \left(\frac{F^{-2} x_*}{UT}\right)(z_b)_t = 0,$$

$$(z_b)_t + \left[(u - v_c)^b \left(1 - \frac{\gamma' h_*}{x_*}(z_b)_x\right)\right]_x = 0 \tag{3.2}$$

where $\kappa = \frac{x_*}{UT}$ is the ratio of the hydrodynamic time scale to the morphological time scale. This ratio is assumed to be much smaller than one, since the morphological changes take place slower than the hydrodynamic changes (the quasi-steady assumption). $F = U/\sqrt{g h_*}$ is the Froude number, which is also assumed to be much smaller than one (the rigid-lid assumption).

The basic flow consisting of a steady along channel flow U is perturbed such that

$$\begin{aligned} u(x,t) &= U + \tilde{u}(x,t), \\ \eta(x,t) &= 0 + \tilde{\eta}(x,t), \\ z_b(x,t) &= 0 + \tilde{z_b}(x,t) \end{aligned} \tag{3.3}$$

With the above assumptions, terms including κ and F can be neglected. Assuming small perturbations ($\tilde{u}/U < 1$) and further linearizing the equations we obtain

$$U u_x = -\eta_x - \frac{x_* c_f}{h_*}\left[2uU + z_b U^2\right],$$

$$U(z_b)_x - u_x = 0,$$

$$-(U - v_c)^b \frac{\gamma' h_*}{x_*}(z_b)_{xx} - b(U - v_c)^{b-1} u_x + (z_b)_t = 0 \tag{3.4}$$

Here the tildes are all dropped. This system allows for travelling wave solutions with constant amplitudes, wavenumber k and frequency ω

$$[u, \eta, z_b] = [u_o, \eta_o, z_o] e^{i(kx - \omega t)} \tag{3.5}$$

Plugging this form into the equations we can rewrite them in matrix form

$$\mathbf{Q}\mathbf{f_o} = \mathbf{0} \tag{3.6}$$

where

$$\mathbf{Q} = \begin{bmatrix} ikU + \left(\frac{x_* c_f}{h_*}\right) 2U & ik & \left(\frac{x_* c_f}{h_*}\right) U^2 \\ -1 & 0 & U \\ ikb(U - v_c)^{b-1} & 0 & -i\omega + (U - v_c)^b \left(\frac{\gamma' h_*}{x_*}\right) k^2 \end{bmatrix}, \quad \mathbf{f_o} = \begin{bmatrix} u_o \\ \eta_o \\ z_o \end{bmatrix} \tag{3.7}$$

For this form to hold the determinant of the matrix, $\mathbf{Q}$ should be equal to zero, $det(\mathbf{Q}) = 0$. Carrying out this calculation leads to a dispersion relationship for ω and k

$$\omega = \omega_r + i\omega_i = [Ub(U - v_c)^{b-1}]k + i[-(U - v_c)^b \gamma' h_* / x_*]k^2 \tag{3.8}$$

where $\omega_i > 0$ corresponds to growth of the instabilities. Since it is not possible for ω_i to become a positive term (the term in front of k^2 is always greater than zero for transport to happen), a 1D channel is stable under these circumstances. One way for bed instabilities to grow ($\omega_i > 0$) is when a phase difference between η (or u) and z_b is introduced (Kennedy, 1963). For a 1D channel ω is independent of the bottom friction factor. It is necessary to consider a 2D channel for bottom friction to enter the dispersion relation, as will be shown in the next section.

An example dispersion curve is shown in the Figure 3.2 for arbitrarily chosen parameters. Note that the dispersion curve (Figure 3.2(a))representing propagation of the bed perturbations is always linear and positive which means that the bed features propagate along with the stream at constant speed. The main controlling parameter of the decay rate magnitude is h_*/x_*; the general shape of the curve remains the same (Figure 3.2 (b)).

Following the same procedure it is possible to obtain a more complicated dispersion relation without considering the previous assumptions, which means that more terms are retained in the equations.

The above matrix, $\mathbf{Q}$ then becomes

$$\mathbf{Q} = \begin{bmatrix} -i\omega\kappa + ikU + \frac{x_* c_f}{h_*} 2U & ik - \frac{x_* c_f}{g h_*^2} U^4 & \frac{x_* c_f}{h_*} U^2 \\ -ik\frac{g h_*}{U^2} & -i\omega\kappa + ikU & -ik\frac{g h_*}{U} + i\omega \frac{h_* x_* g}{U^3 T} \\ ikb(U - v_c)^{b-1} & 0 & -i\omega + (U - v_c)^b \frac{\gamma' h_*}{x_*} k^2 \end{bmatrix} \tag{3.9}$$

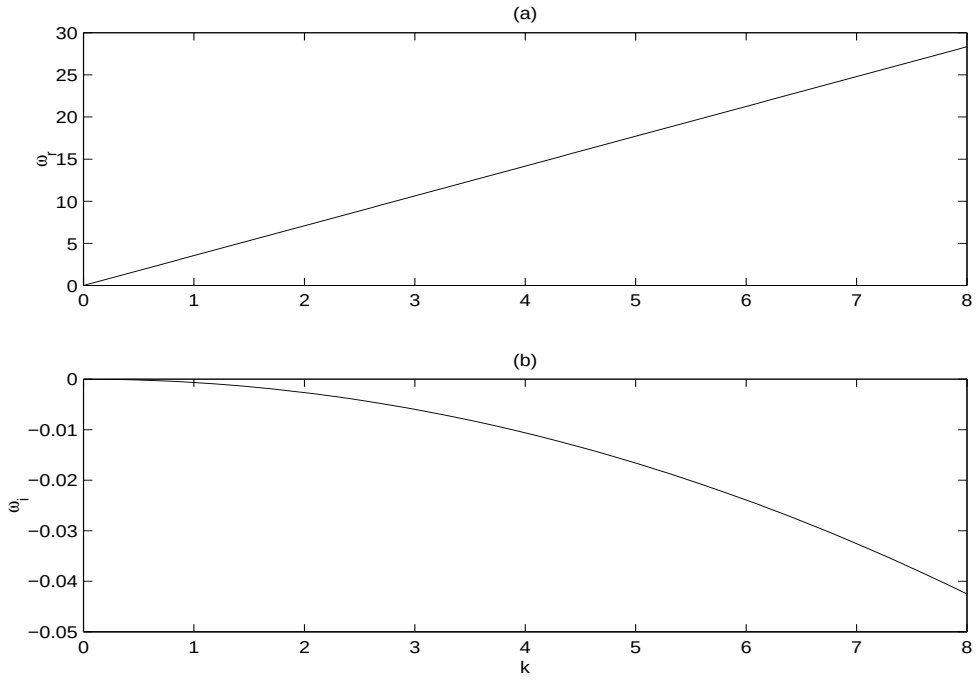

Figure 3.2: Dispersion curves for a 1D channel, with parameters: $U = 1m/s$, $b = 6$, $v_c = 0.1m/s$, $\gamma' = 1$, $h_* = 5m$, $x_* = 4000m$.

Again, setting $det(\mathbf{Q}) = 0$ a cubic equation relating ω with k can be found

$$A\omega^3 + B\omega^2 + C\omega + D = 0 \tag{3.10}$$

where,

$$\begin{aligned}
A &= i\kappa^2, \\
B &= -(U - v_c)^b \gamma' h_* / x_* \kappa^2 k^2 - i2k\kappa U - c_f x_* 2U / h_* \kappa, \\
C &= 2k^3 \kappa U (U - v_c)^b \gamma' h_* / x_* + ik^2 U^2 - ic_f 2U\kappa (U - v_c)^b \gamma' k^2 - ik^2 g h_* / U^2 \\
&\quad + g h_* c_f x_* U^4 / (U^2 g h_*^2) + c_f x_* 2U^2 k / h_* - ib(U - v_c)^{b-1} h_* x_* g / (TU^3),
\end{aligned}$$

$$\begin{aligned}
D = -(U - x_*)^b \gamma' h_* / x_* [U^2 k^4 + ic_f x_* 2U / h_* U k^3 + igh_* / Uk^3 + gh_* / U^2 k^4 \\
+ igh_* / U^2 c_f x_* U^4 / (gh^2) k^3]
\end{aligned}$$

Two of the roots of this equation are spurious results which do not represent correct dispersion relations for this case. The third root should be the correct one representing the solution, for this case without the rigid-lid and quasi-steady assumptions.

A comparison is shown in Figure 3.3. The parameters are the same as in the previous figure, with an addition of $c_f = 0.001$. The first four lines are from the spurious roots and the last two are from the third correct root.

The real ω values show a reasonable match for smaller wavenumbers, whereas for larger values of k the difference is evident. The shape of the curve for the imaginary ω values is more

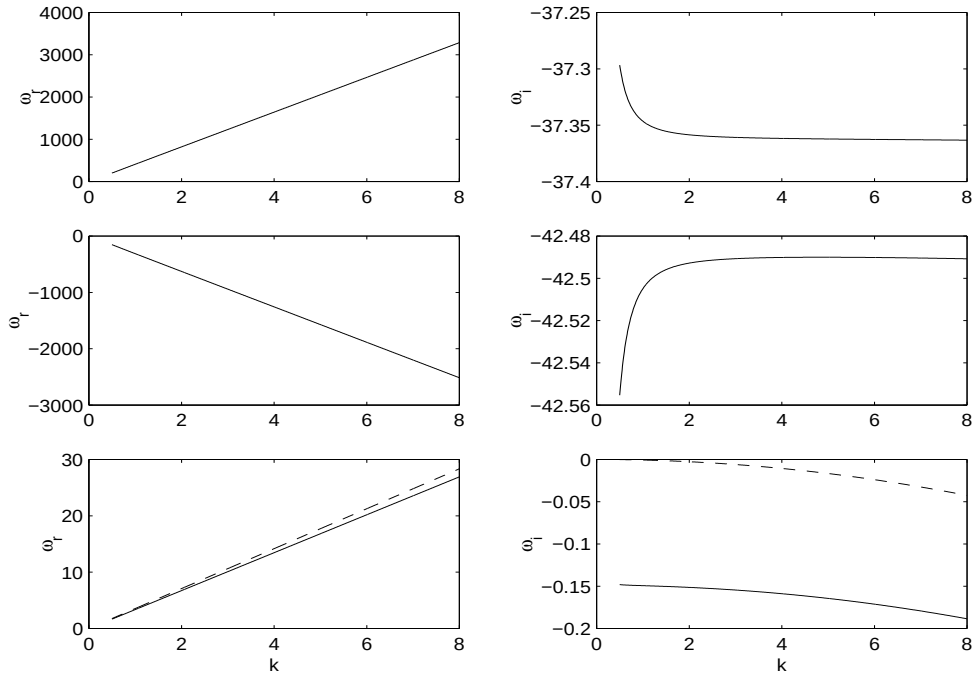

Figure 3.3: A comparison between dispersion curves for a 1D channel with parameters: $U = 1m/s$, $b = 6$, $v_c = 0.1m/s$, $\gamma' = 1$, $h_* = 5m$, $x_* = 4000m$, $c_f = 0.001$. (—) results without assumptions,(- -) results with assumptions.

or less the same with a difference in magnitudes, which decreases with a decreasing friction factor c_f as shown in Figure 3.4. As a conclusion, the difference between the dispersion relationships obtained from the analysis with and without the assumptions show no great difference. The overall shape of the curves is not affected, but the magnitudes of the ω values change as the wavenumbers increase.

For a 1D channel this analysis does not reveal more detailed results, since the bed instabilities show no growth.

3.2 Two-dimensional Channel

For a 2D channel, equations (2.1)-(2.4) are considered. The only differences are that the sediment transport equation includes a threshold velocity v_c, and that the analysis is done for an arbitrary basic flow U. Rewriting them

$$u_t + uu_x + vu_y = -g\eta_x - c_f(u^2 + v^2)^{1/2}u/d - c_f U^2/h_*,$$

$$v_t + uv_x + vv_y = -g\eta_y - c_f(u^2 + v^2)^{1/2}v/d,$$

$$d_t + (ud)_x + (vd)_y = 0, \qquad (z_b)_t + (q_x x)_x + (q_y y)_y = 0 \tag{3.11}$$

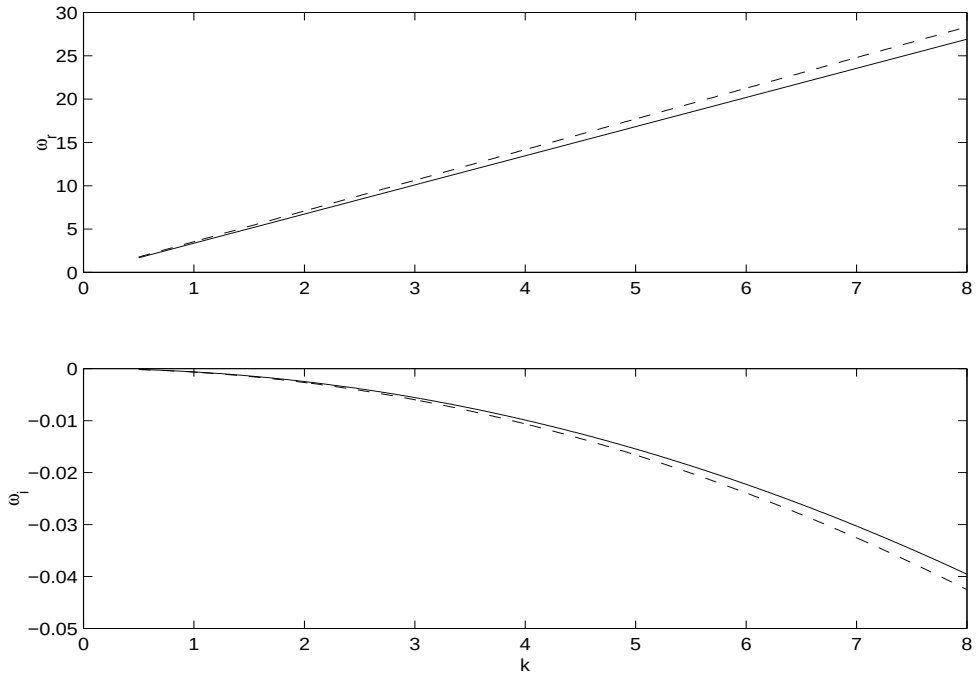

Figure 3.4: A comparison between dispersion curves for a 1D channel with parameters: $U = 1m/s$, $b = 6$, $v_c = 0.1m/s$, $\gamma' = 1$, $h_* = 5m$, $x_* = 4000m$, $c_f \approx 0.0$. (—) results without assumptions,(- -) results with assumptions.

Here d is the total depth and q_x and q_y are the volumetric sediment transport rates along channel and across channel, respectively. Once again, the porosity effect is included in the transport equation through ν.

The nondimensional terms are the same as before, except for the horizontal scales: $(x, y) = y_*(\hat{x}, \hat{y})$, where y_* is the channel width.

Perturbing the scaled equations with the same form as in equation (3.3), but also allowing for a cross channel variation and carrying out the same linearization as before, the matrices $\mathbf{Q}$ and $\mathbf{f_o}$ become

$$\mathbf{Q} = \begin{bmatrix} ikU + c_f R2U & 0 & ik & c_f RU^2 \\ 0 & ikU + Rc_f U & (\,)_y & 0 \\ ik & (\,)_y & 0 & -ikU \\ ikb(U - v_c)^{b-1} & \frac{(U-v_c)^b}{U}(\,)_y & 0 & -i\omega + (U - v_c)^{b-1} R\gamma'[k^2 - (\,)_{yy}] \end{bmatrix},$$

$$\mathbf{f_o} = \begin{bmatrix} u_o \\ v_o \\ \eta_o \\ z_o \end{bmatrix} \tag{3.12}$$

where, $R = y_*/h_*$.

As discussed in Chapter 2, this matrix can be reduced by a standard Gauss elimination

procedure to lead to a fourth-order equation for z_b (see equation (2.8)). Substituting the solution form given in (2.9) gives the following dispersion relationship,

$$\omega = \frac{b_2(p\pi)^2 - b_3(p\pi)^4 - b_1}{a_1 - a_2(p\pi)^2} \tag{3.13}$$

where

$$\begin{aligned}
a_1 &= (-ik^3 - k^2 R c_f)U^2(U - v_c)^b, \\
a_2 &= (2Rc_f + ik)U^2(U - v_c)^b, \\
b_1 &= k^5(\gamma'/R)\frac{U^2}{U - v_c} + k^4\left(-i\gamma' c_f \frac{U^2}{U - v_c} + ib\frac{U^3}{U - v_c}\right) + k^3 bRc_f \frac{U^3}{U - v_c}, \\
b_2 &= -2k^3(\gamma'/R)\frac{U^2}{U - v_c} + k^2\left(-iU^2 + i3\gamma' c_f \frac{U^2}{U - v_c}\right) \\
&\qquad + kRc_f\left(-3U^2 + b\frac{U^3}{U - v_c}\right), \\
b_3 &= -(\gamma'/R)\left(i2c_f \frac{R}{U - v_c} - k\frac{U^2}{U - v_c}\right)
\end{aligned} \tag{3.14}$$

The first mode of the bed forms representing alternate bars is for $p = 1$.

For this dispersion relation, it is possible to obtain certain ranges of k where ω is greater than zero (Figure 3.5). Different dispersion curves result for different ranges of parameters R, c_f, b. These effects can be seen in the following figures. The most unstable wavenumbers are shown with a small black dot on every growth curve.

In Figure 3.6, the effect of increasing R is shown. While for the curves representing propagation speed the effect is not very significant, for the growth curves the unstable wavenumber range and the maximum unstable wavenumber are increasing with increasing R. The dash-dotted curve for R_c is obtained from equation(2.10). For fixed values of b and c_f, R seems to be an important parameter controlling bed instabilities. Fixing R and c_f and changing b has a very similar effect on the dispersion curves. For the range of b values given in Figure 3.7, the effect on both set of curves is in the form of an increase; the propagation speed is increasing as well as the unstable wavenumber range and the most unstable wavenumber. This is also the case for R values below R_c, the critical width-to-depth ratio. The most significant changes occur for higher values of the friction factor c_f, which is shown in Figure 3.8. For $b = 6$ and $R = 44$, even a slghtly larger c_f value causes significantly higher values of k. A rudimentary explanation for this can be the increase of flow resistance that has to be overcome by an instability with a higher wavenumber. The propagation curves are very little affected by increasing c_f values.

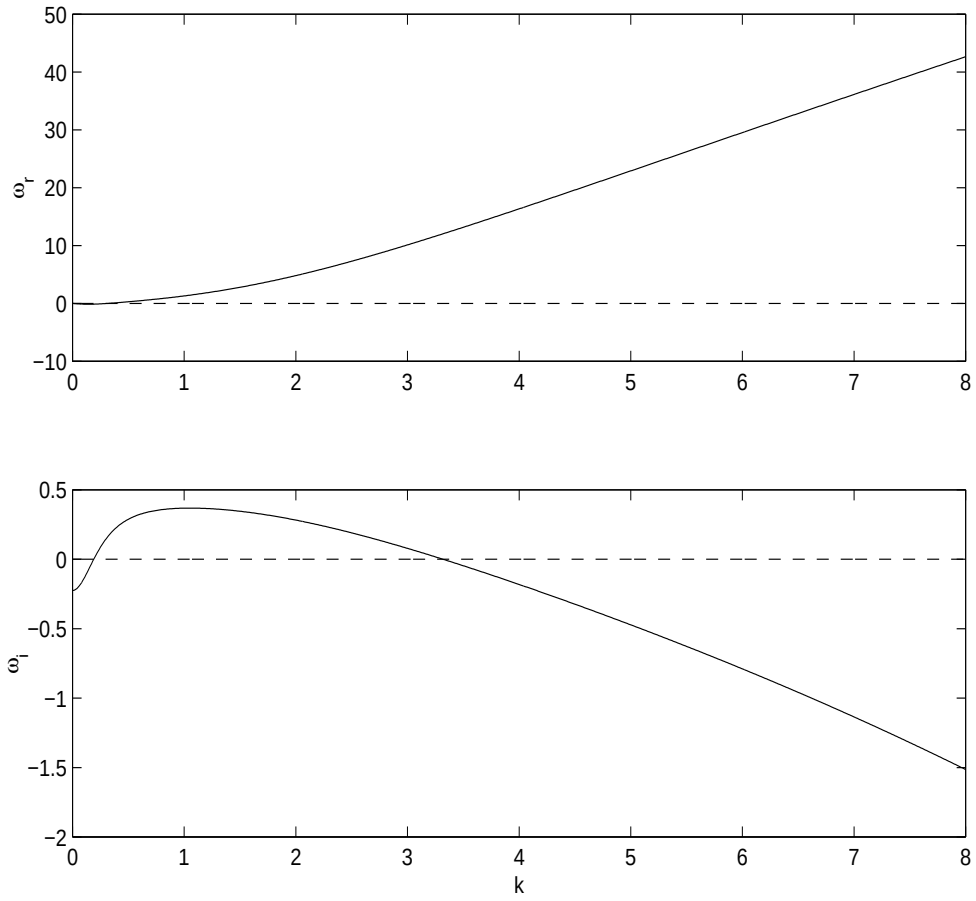

Figure 3.5: An example of dispersion curves for a 2D channel where growth of bed instabilities happens for a certain range of wavenumbers. Parameters: $U = 1m/s$, $b = 6$, $v_c = 0$, $\gamma' = 1$, $R = 44$, $c_f = 0.003$.

Different values for U and v_c do not have a surprisingly different effect on the dispersion curves which is also evident from the dispersion relationship (3.13). This is shown in Figure 3.9. Changing these values changes only the magnitudes of ω, and the imaginary part ω_i is inversely proportional to the values of U and v_c for a fixed wavenumber k. The unstable wavenumber intervals and the most unstable wavenumbers are not affected.

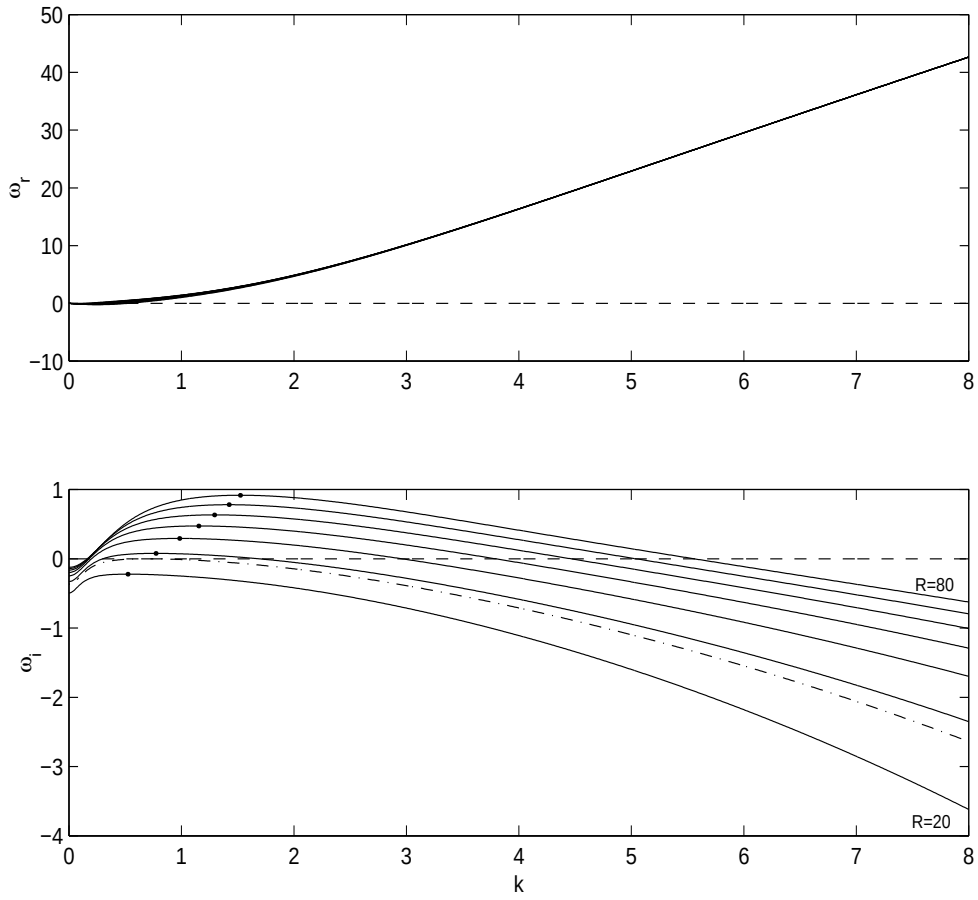

Figure 3.6: 2D channel dispersion curves for $R = 20 - 80$ with parameters: $U = 1m/s$, $b = 6$, $v_c = 0$, $\gamma' = 1$, $c_f = 0.003$. (-.-)$R_c = 26.9692$.

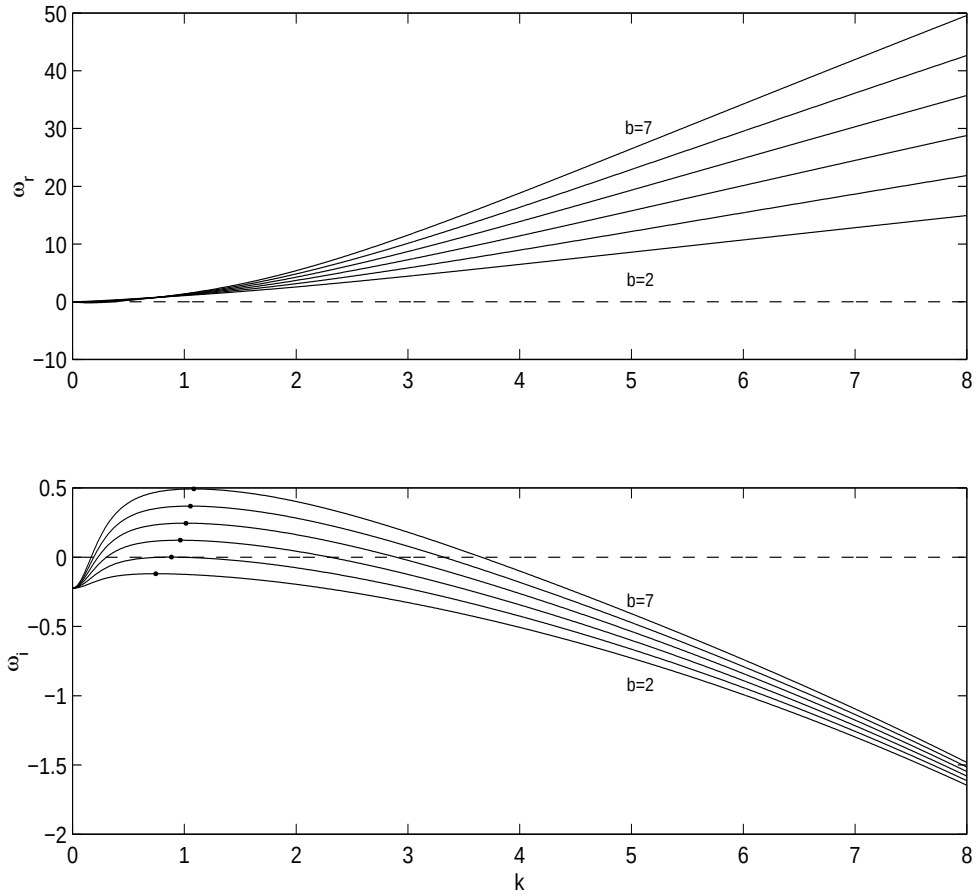

Figure 3.7: 2D channel dispersion curves for $b = 2 - 7$ with parameters: $U = 1m/s$, $R = 44$, $v_c = 0$, $\gamma' = 1$, $c_f = 0.003$.

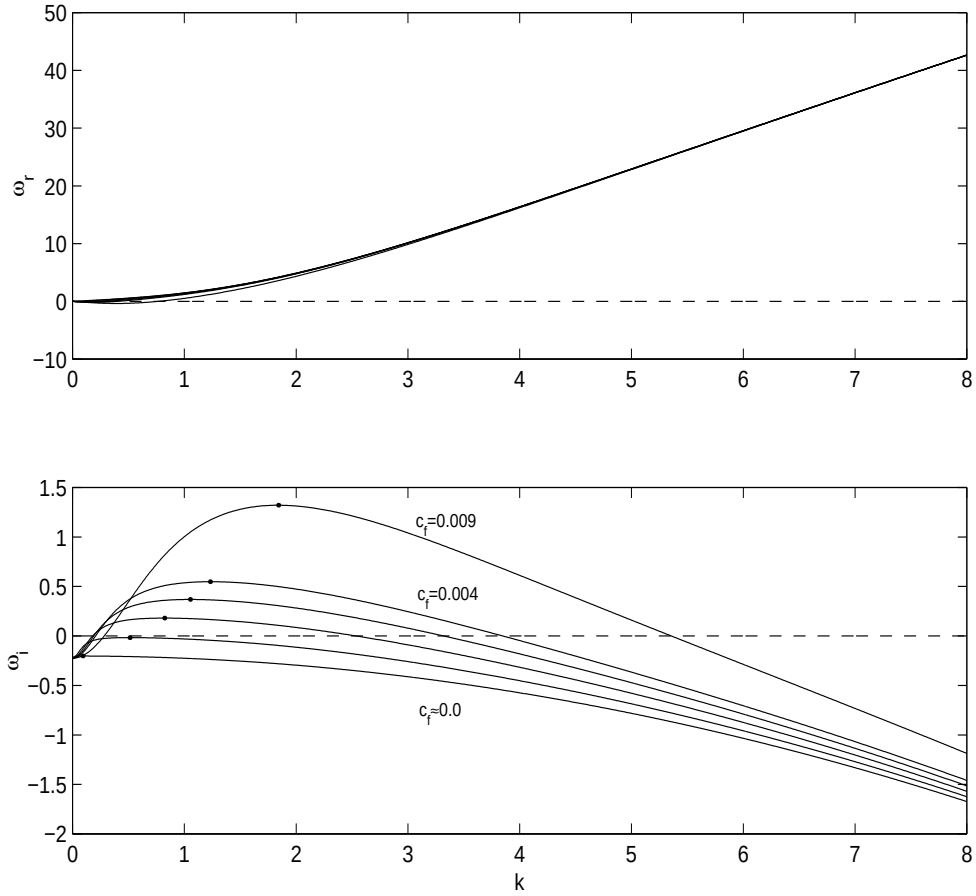

Figure 3.8: 2D channel dispersion curves for $c_f = 0.0 - 0.009$ with parameters: $U = 1m/s$, $R = 44$, $b = 6$, $v_c = 0$, $\gamma' = 1$.

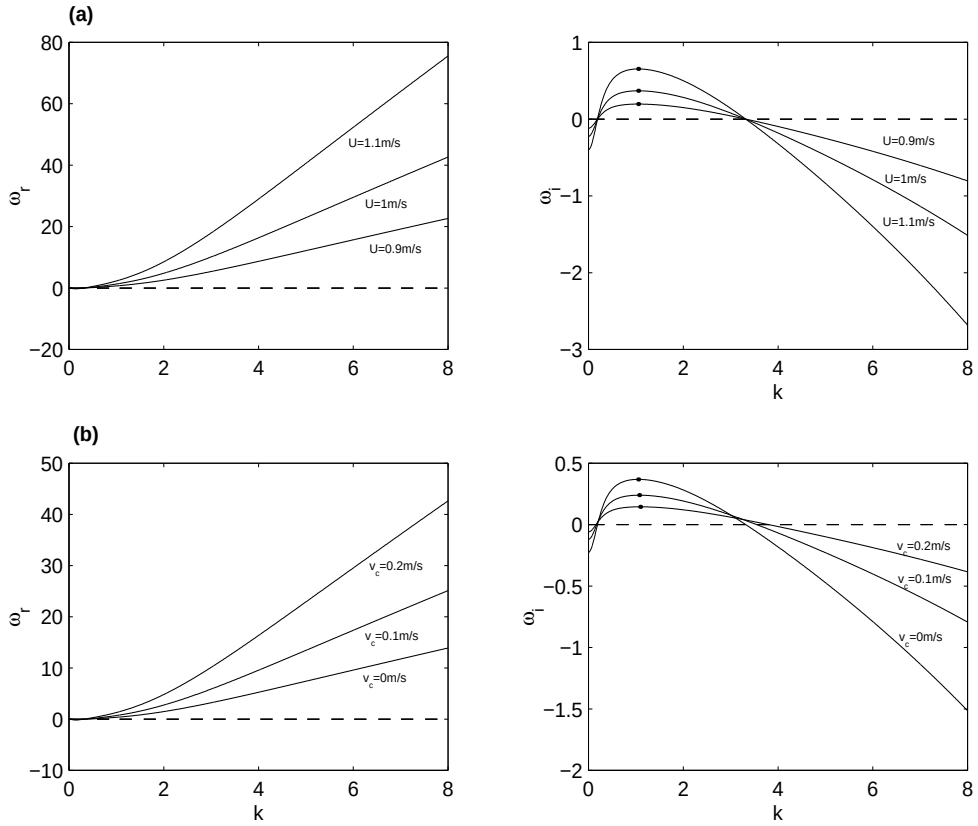

Figure 3.9: 2D channel dispersion curves for different ranges of U and v_c values, with parameters: $R = 44$, $b = 6$, $\gamma' = 1$, $c_f = 0.003$, (a) $v_c = 0$, (b) $U = 1m/s$.

As stated before, these dispersion curves provide information only on the propagation and growth of the bed instabilites for the linear problem. This information can be used to study instabilities in more detail including nonlinear effects and the actual geometry of the resulting bed forms. Detailed results using this information will be shown in Chapter 5.

Chapter 4

THE HYDRODYNAMIC MODEL EXTENDED WITH SEDIMENT TRANSPORT CAPABILITY

In order to account for the coupling between the evolving bed and flow field, equations governing sediment transport and sediment continuity are necessary in addition to the equations governing the hydrodynamic processes. The standard equations of fluid motion consist of the momentum and the mass conservation equations. The momentum equations used are in the form of the horizontal shallow water equations including terms for short wave and turbulent motions of shorter time scales, and terms for dissipation due to bottom friction. The sediment transport equation relates the current velocity to the volumetric sediment transport rates. This equation can be of different forms depending on the theory it is based on. Generally based on energetics concepts it is assumed that the current velocity raised to some power is related to the transport flux by some coefficient. Considering transport due to waves and currents separately, this equation can become more complicated. Other factors like the bed slope, threshold velocity, or type of sediment transport (suspension, bedload) can be considered, too. The sediment continuity equation is very similar to the mass conservation equation for fluid motion; it is based on the same physical reasoning. This equation relates the change of the bed in time to the spatial gradient of the sediment transport rates, thereby allowing for the computation of the bed evolution.

In this chapter, a review of the governing equations of the hydrodynamic model developed by Özkan-Haller and Kirby (1997, 1999), as well as the numerical method used to solve these equations are presented. A short description of the sediment transport and conservation equations, and their incorporation into the hydrodynamic model are also included.

4.1 Generation of the Flow Field

The governing equations are the depth- and wave-averaged shallow water equations with additional short wave forcing and frictional damping terms, and the mass conservation equa-

tion.

$$\begin{aligned}\frac{\partial u}{\partial t}+u\frac{\partial u}{\partial x}+v\frac{\partial u}{\partial y} &= -g\frac{\partial \eta}{\partial x}+F_x+\tau_{\ell x}-\tau_{bx},\\ \frac{\partial v}{\partial t}+u\frac{\partial v}{\partial x}+v\frac{\partial v}{\partial y} &= -g\frac{\partial \eta}{\partial y}+F_y+\tau_{\ell y}-\tau_{by}\end{aligned} \tag{4.1}$$

$$\frac{\partial \eta}{\partial t}+\frac{\partial [ud]}{\partial x}+\frac{\partial [vd]}{\partial y}=0 \tag{4.2}$$

Here, η is the short-wave averaged water surface elevation above still water level, h is the still water depth, $d=(h+\eta)$ is the total water depth which also may include different bedforms in the form of instabilities, u and v are the depth-averaged current velocities in the x and y directions, respectively, where x points offshore and y points alongshore. F_x and F_y are the short wave forcing terms, $\tau_{\ell x}$ and $\tau_{\ell y}$ represent the turbulent lateral mixing effects. The bottom friction terms are τ_{bx} and τ_{by}.

The short wave forcing terms are based on the radiation stress concept by Longuet-Higgins and Stewart (1964). A release of momentum occurs in the surf zone when waves break as they apporoach the shore. This excess momentum is referred to as radiation stress which actually forces current motions. These forcing terms can be modeled as

$$F_\alpha=-\frac{1}{\rho d}\frac{\partial S_{\alpha\beta}}{\partial x_\beta} \tag{4.3}$$

where α,β represent x,y directions. The radiation stress components $S_{\alpha\beta}$ are defined in terms of orbital wave velocities using linear water wave theory.

$$\begin{aligned}S_{xx} &= E\left[\frac{c_g}{c}(\cos^2\theta+1)-\frac{1}{2}\right],\\ S_{xy} &= E\frac{c_g}{c}\sin\theta\cos\theta,\\ S_{yy} &= E\left[\frac{c_g}{c}(\sin^2\theta+1)-\frac{1}{2}\right]\end{aligned} \tag{4.4}$$

where E is the wave energy given by

$$E=\frac{1}{8}\rho g H^2 \tag{4.5}$$

In these equations, H is the wave height, θ is the angle of wave incidence, and $c=(2\pi\tilde{f})/\tilde{k}$ is the short wave celerity, where $\tilde{f}$ is the frequency and $\tilde{k}$ is the wavenumber given by the linear dispersion relationship

$$(2\pi\tilde{f})^2=g\tilde{k}\tanh(\tilde{k}h) \tag{4.6}$$

The group velocity is defined as $c_g=nc$ where

$$n=\frac{1}{2}\left(1+\frac{2\tilde{k}h}{\sinh 2\tilde{k}h}\right) \tag{4.7}$$

Considering random waves, the above equations for the radiation stress terms can be defined by the directional spectrum made up of discrete wave height H_i, frequency $\tilde{f}_i$ and angle of incidence θ_i components. The total energy spectrum is the sum of each component E_i, and can be computed from (4.5) by replacing H with H_{rms}, the root-mean-square wave height. Further details about the case of random waves can be found in Özkan-Haller (1997). In this study random waves are not considered.

Provided that the wave height H, the wavenumber $\tilde{k}$ and the angle of incidence θ are known as a function of space, the radiation stress terms can be computed externally and hence the forcing terms F_x and F_y. If not known for the whole domain, given the offshore values of the above parameters and using short wave transformation due to shoaling, refraction, diffraction and breaking, the radiation stress terms can be obtained.

The parameters representing the effect due to lateral momentum mixing are, $\tau_{\ell x}$ and $\tau_{\ell y}$. This mixing effect in the surf zone majorly arises due to the gradients of turbulence-induced momentum fluxes, which can be represented by the depth-integrated Reynolds' stresses $S'_{\alpha\beta}$. The Reynolds' stresses are a function of the turbulent velocity components and since these are generally not known, the Reynolds' stresses can be directly associated with the mean current.

$$S'_{\alpha\beta} = -\rho\nu_t d\left(\frac{\partial u_\alpha}{\partial x_\beta} + \frac{\partial u_\beta}{\partial x_\alpha}\right) \tag{4.8}$$

The parameter ν_t is the turbulent eddy viscosity.

Another source reinforcing lateral mixing is a dispersion process due to additional terms arising in the depth-averaged momentum equations when depth nonuniformity of the velocity profiles is considered (Svendsen and Putrevu, 1994; Putrevu and Svendsen, 1999). Rederiving the equations, Putrevu and Svendsen (1999) represented the most dominant additional terms as the ones premultiplied by the coefficient $D_{\alpha\beta}$. This coefficient is a function of the depth variation of the current velocities and is assumed to be proportional to the wave-induced volume fluxes in the horizontal directions. For small incident wave angles the volume flux in the x direction will be the most pronounced one, therefore terms with D_{xx} can be retained as a first approximation. Svendsen and Putrevu (1994) also showed that D_{xx} can be orders of magnitude larger than ν_t. Following this theory the lateral mixing terms can be expressed as

$$\tau_{\ell x} = \frac{2}{d}\frac{\partial}{\partial x}\left(\nu' d\frac{\partial u}{\partial x}\right) + \frac{1}{d}\frac{\partial}{\partial y}\left(\nu' d\frac{\partial v}{\partial x}\right), \qquad \tau_{\ell y} = \frac{1}{d}\frac{\partial}{\partial x}\left(\nu' d\frac{\partial v}{\partial x}\right) \tag{4.9}$$

where $\nu' = \nu_t + D_{xx}$ is the effective eddy viscosity.

Following Battjes (1975), the cross-shore variation of ν can be formulated as

$$\nu' = Md\left(\frac{\epsilon_b}{\rho}\right)^{1/3} \tag{4.10}$$

where M is a mixing coefficient and ϵ_b is the ensemble-averaged wave energy dissipation due to breaking.

A more detailed discussion about these equations can be found in the study by Özkan-Haller (1997), or in the above mentioned references.

The bottom friction terms can be written in the general form as

$$\begin{aligned} \tau_{bx} &= \frac{1}{d} c_f \overline{|\mathbf{u}|(u+\tilde{u})}, \\ \tau_{by} &= \frac{1}{d} c_f \overline{|\mathbf{u}|(v+\tilde{v})} \end{aligned} \tag{4.11}$$

where c_f is a friction coefficient and $|\mathbf{u}| = [(u+\tilde{u})^2 + (v+\tilde{v})^2]^{1/2}$. $\tilde{u}$ and $\tilde{v}$ are the short wave orbital velocity components, and u and v are the current velocity components. The overbar denotes time averaging over the short wave time scale. Assuming small incident wave angles and that the maximum orbital wave velocity u_o is much larger than the mean current a simple formulation for the bottom stress terms can be obtained after linearizing with respect to u_o

$$\tau_{bx} = \frac{\mu}{d} u, \qquad \tau_{by} = \frac{\mu}{d} v \tag{4.12}$$

where $\mu = 2/\pi c_f u_o$.

Using linear wave theory the maximum orbital velocity is given by $u_o = \frac{cH}{2h}$. Equation (4.12) is the mathematically most simplest formulation of the bottom stress. Improvements can be made by incorporating a higher order wave theory or lifting the weak current assumption.

Substituting the expressions for the forcing and damping terms into (4.1) the final form of the momentum equations can be obtained.

$$\begin{aligned} \frac{\partial u}{\partial t} + u\frac{\partial u}{\partial x} + v\frac{\partial u}{\partial y} &= -g\frac{\partial \eta}{\partial x} - \frac{1}{\rho d}\left(\frac{\partial S_{xx}}{\partial x} + \frac{\partial S_{xy}}{\partial y}\right) - \frac{\mu}{d}u \\ &\quad + \frac{2}{d}\frac{\partial}{\partial x}\left(\nu d \frac{\partial u}{\partial x}\right) + \frac{1}{d}\frac{\partial}{\partial y}\left(\nu d \frac{\partial v}{\partial x}\right), \\ \frac{\partial v}{\partial t} + u\frac{\partial v}{\partial x} + v\frac{\partial v}{\partial y} &= -g\frac{\partial \eta}{\partial y} - \frac{1}{\rho d}\left(\frac{\partial S_{xy}}{\partial x} + \frac{\partial S_{yy}}{\partial y}\right) - \frac{\mu}{d}v \\ &\quad + \frac{1}{d}\frac{\partial}{\partial x}\left(\nu d \frac{\partial v}{\partial x}\right) \end{aligned} \tag{4.13}$$

4.2 Sediment Transport and Evolving Bottom

The sediment transport equation used in this study is a simple relationship between the current velocities and the transport rates. It assumes that only bedload transport occurs; suspendend sediment load is neglected. This assumption rules out sediment transport due to waves, which may become important in the surfzone where cross-shore proccesses are dominant as well. There are more complete equations in the literature which consider bedload and suspended transport (Bagnold, 1966; Bailard, 1981; Bailard and Inman, 1981).

The sediment transport rate in one direction is related to the current velocity in the same direction raised to some power and multiplied by a coefficient which is a function of sediment parameters.

$$\mathbf{q} = \nu(|\mathbf{u}| - v_c)^b \left(\frac{\mathbf{u}}{|\mathbf{u}|} + \gamma' \nabla h\right), \qquad if \quad |\mathbf{u}| > v_c \tag{4.14}$$

where $\mathbf{q}$ is the volumetric sediment transport rate vector, ν is the coefficient representing sediment and bed characteristics, v_c is a critical velocity for initiation of transport, $\mathbf{u}$ is the current velocity vector, and $\gamma' \nabla h$ takes care of the tendency of sediments moving downslope. Note the plus sign in front of this term, this is because this equation has been modified to fit the coordinate system of the model (see also equation (4.15)). The coefficient γ' represents the inverse of the dynamic coefficient of Coulomb friction (Schielen *et al.*, 1993). This coefficient has been taken as a constant value of 1, except where stated different. Note also that this equation is different than (2.13) and (2.3) in that it includes the actual bed gradient rather than the gradient of the bed perturbation. It is more accurate to include the actual bed slope although Falqués *et al.* (1996a) consider the bed gradient as its equilibrium state. Here we prefer to let the bed profile including the perturbations reach its equlibrium state in time. Accurate values for b are in fact not well established, typical values range between 2 and 7. Many transport equations are in a similar form. A review of several transport equations can be found in van Rijn (1989).

The sediment conservation equation

$$\frac{\partial h}{\partial t} - \nabla \cdot \mathbf{q} = 0 \tag{4.15}$$

is very similar to the fluid mass conservation equation. This equation closes the system, and enables one to compute the bed evolution in time.

4.3 Solution Method

The model domain starts from the shoreline and extends to some offshore distance L_x and it has a longshore width of L_y, where x points to the offshore and y to the longshore direction. It is possible to specify a moving shoreline boundary at the shore, where ζ is the shoreline position as a function of longshore location and time (Figure 4.1). Alternatively, a wall boundary can be specified at each end of the domain, too. It also is able to handle an open offshore boundary by an absorbing-generating boundary condition. This model is set-up to specifically deal with motions that are periodic in the longshore direction, therefore a periodic lateral boundary condition is used. Although never tested in detail, one can also specify lateral wall boundaries in the model.

4.3.1 Governing Equations

The numerical method is based on spectral collacation schemes which handle the spatial derivatives, and an explicit time integration of high order. The most suitable approach for spectral collacation methods is to work with the characteristic forms of the governing equations in order to properly specify boundary conditions.

The equations governing the hydrodynamics can be rewritten in matrix form as

$$\mathbf{q}_t + \mathbf{A}\mathbf{q}_x + \mathbf{B}\mathbf{q}_y = \mathbf{C} \tag{4.16}$$

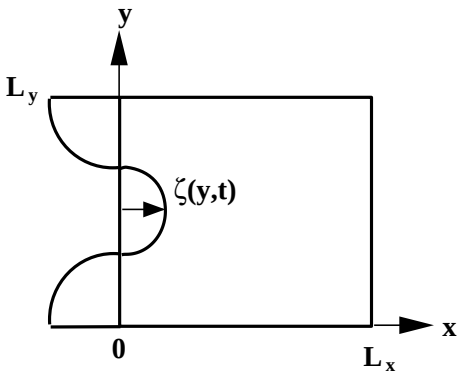

Figure 4.1: Sketch of the model domain.

where

$$\mathbf{q} = \begin{bmatrix} d \\ u \\ v \end{bmatrix}, \quad \mathbf{A} = \begin{bmatrix} u & d & 0 \\ g & u & 0 \\ 0 & 0 & u \end{bmatrix}, \quad \mathbf{B} = \begin{bmatrix} v & 0 & d \\ 0 & v & 0 \\ g & 0 & v \end{bmatrix}, \quad \mathbf{C} = \begin{bmatrix} 0 \\ gh_x + F \\ gh_y + G \end{bmatrix} \tag{4.17}$$

Here, G and F are functions representing the forcing and dissipation terms.

Multiplying (4.16) with the inverse of the eigenvector matrix of $\mathbf{A}$, the following expression can be obtained after some manipulations

$$\mathbf{w}_t + \mathbf{A}'\mathbf{w}_x + \mathbf{B}'\mathbf{w}_y = \mathbf{C}' \tag{4.18}$$

where

$$\mathbf{A}' = \begin{bmatrix} u - \sqrt{gd} & 0 & 0 \\ 0 & u + \sqrt{gd} & 0 \\ 0 & 0 & u \end{bmatrix}, \qquad \mathbf{B}' = \begin{bmatrix} v & 0 & -\sqrt{gd} \\ 0 & v & \sqrt{gd} \\ -\frac{1}{2}\sqrt{gd} & \frac{1}{2}\sqrt{gd} & v \end{bmatrix},$$

$$\mathbf{C}' = \begin{bmatrix} gh_x + F \\ gh_x + F \\ gh_y + G \end{bmatrix} \tag{4.19}$$

The vector $\mathbf{w}$ includes the unknowns for which the model solves for

$$\mathbf{w} = \begin{bmatrix} u - 2\sqrt{gd} \\ u + 2\sqrt{gd} \\ v \end{bmatrix} \equiv \begin{bmatrix} \beta^- \\ \beta^+ \\ \gamma \end{bmatrix} \tag{4.20}$$

The governing equations can now be rewritten as

$$\beta_t^- + (u - c)\beta_x^- + v\beta_y^- - c\gamma_y = 2c_o c_{ox} + F \tag{4.21}$$

$$\beta_t^+ + (u + c)\beta_x^+ + v\beta_y^+ - c\gamma_y = 2c_o c_{ox} + F \tag{4.22}$$

$$\gamma_t + u\gamma_x + v\gamma_y = -g\eta_y + G \tag{4.23}$$

In these equations, $c = \sqrt{gd}$ is the nonlinear shallow water wave speed, and $c_o = \sqrt{gh}$ is the linear one. Equation (4.22) carries information in the $+x$ direction (specified with the '+'

superscript), therefore it is valid within the domain and only on the right boundary points. For (4.21) the opposite is true, it carries information in the $-x$ direction and is valid inside the domain and only on the left boundary. Equation (4.23), on the other hand is valid everywhere in the domain including the boundaries.

The sediment transport and bed evolution equations are kept in their original forms. At every time step the sediment transport rates are computed using the corresponding current velocities obtained from the hydrodynamic part. The time integration applied to the sediment conservation equation (4.15) leads the new bed configuration with which the new flow field is calculated at the next time step.

4.3.2 Numerical Scheme

Recently, spectral and pseudospectral methods have become popular in numerical modeling due to enhanced accuracy of spatial derivatives when compared to finite difference approximations. Depending on the motion of interest, it is possible to chose basis functions of the spectral derivatives that naturally satisfy the boundary conditions, with variable grid spacings in order to achieve higher accuracy where needed. Schielen *et al.* (1993) used a spectral method in their stability analysis when solving the Ginzburg-Landau equation in order to obtain the bedform amplitudes. Falqués and Iranzo (1994) used a Chebyshev collacation method in the treatment of an eigenvalue problem resulting from their study on nearshore vorticity waves as a stability problem. In addition, Falqués *et al.* (1996a, 1996b) used the same procedure in their study about morphodynamic and longshore current instabilities. A more detailed review on spectral methods can be found in Canuto *et al.* (1987).

Considering the enhanced accuracy along with less computational time involved, a pseudospectral collocation method has been used in this model.

Given the initial conditions for the water surface η, the velocity components u and v, and the bottom topography represented by the water depth h, the equations are integrated in time using an explicit third-order Adams-Bashforth scheme. This integration method proves to be an accurate scheme often used with collocation methods (Canuto *et al.*, 1987).

Equations (4.21)-(4.23) and (4.15) can be rewritten as

$$\begin{aligned} \beta_t^- &= F_1(\eta, u, v), \\ \beta_t^+ &= F_2(\eta, u, v), \\ \gamma_t &= F_3(\eta, u, v), \\ h_t &= F_4(h, u, v) \end{aligned} \tag{4.24}$$

The functions F_1, F_2, F_3 and F_4 contain spatial derivatives of their arguments. F_4 is related to its arguments through the sediment transport equation (4.14). The functions can be obtained by comparing these equations with (4.21)-(4.23) and (4.14)-(4.15).

Let Q represent one of the variables β^-, β^+, γ, or h and F one of the above functions given in (4.24), then the Adams-Bashforth scheme is written as

$$Q^{n+1} = Q^n + \frac{\Delta t}{12}\left[23F^n - 16F^{n-1} + 5F^{n-2}\right] \tag{4.25}$$

The superscripts denote the time level at which the terms are evaluated with n being the present time level.

In order to account for the moving shoreline at the onshore boundary of the domain and also due to the collocation method used, two coordinate transformations are incorporated (Figure 4.2). The first one is a transformation of the physical coordinate system (x, y) to an intermediate stationary system (ϕ, ψ) given as

$$x = \phi + \zeta(y,t)e^{-\alpha\phi^2}, \quad y = \psi \tag{4.26}$$

The movement of the grid is damped out in the offshore direction, so that the grid becomes stationary at a certain distance which is dictated by the parameter α. As a result of this transformation the derivatives in the equations now become

$$\begin{aligned} (\ )_t|_x &= (\ )_t|_\phi + (\ )_\phi \phi_t \\ (\ )_x &= (\ )_\phi \phi_x \\ (\ )_y &= (\ )_\psi + (\ )_\phi \phi_y \end{aligned} \tag{4.27}$$

where $(\ )_t|_x$ and $(\ )_t|_\phi$ denote time derivatives at a fixed x and ϕ, respectively.

The next transformation is from the stationary (ϕ, ψ) coordinate system to a stationary computational grid (s, r) (Figure 4.2). The domain is discretized into an $(NX+1)\times(NY+1)$ point mesh. The collocation points in the offshore direction s are chosen as the reversed Gauss-Lobatto points given by $s_i = -\cos(\pi i/NX), (i = 0, ..., NX)$. The grid points are concentrated close to the shoreline with this choice. The collocation points in the longshore direction r are chosen to be equally spaced so that $r_j = j\Delta y, (j = 0, ..., NY)$.

The derivatives of the equations are further modified due to the this transformation,

$$\begin{aligned} (\ )_t|_x &= (\ )_t|_s + (\ )_s s_\phi \phi_t \\ (\ )_x &= (\ )_s s_\phi \phi_x \\ (\ )_y &= (\ )_r + (\ )_s s_\phi \phi_y \end{aligned} \tag{4.28}$$

where $(\ )_t|_s$ denotes time derivatives at fixed s values.

Depending on the grid distribution desired within the (ϕ, ψ) domain, different coordinate transformations are available. Three essential transformations will be mentioned here. The first one is a linear transformation which preserves the grid distribution of the physical domain.

$$\phi = \frac{L}{2}(1+s), \quad \psi = r \tag{4.29}$$

The coordinate transformation

$$\phi = L\frac{1+s}{s_o - s}, \quad \psi = r \tag{4.30}$$

has the effect of concentrating the grid points towards the shoreline in the physical domain. This is suitable for modeling shoreline runup. The parameter s_o controls the offshore extend

of the domain, a value of 1 corresponds to an offshore boundary located at infinity. For a finite offshore length, $s_o > 1$. In this study $s_o = 2$ has been used.

A grid of nearly uniformly spaced collocation points in the cross-shore direction s is obtained by the transformation

$$\phi = L\frac{\arccos(-ps) - \arccos(p)}{\arccos(-p) - \arccos(p)}, \quad \psi = r \tag{4.31}$$

with $p = 0.999$.

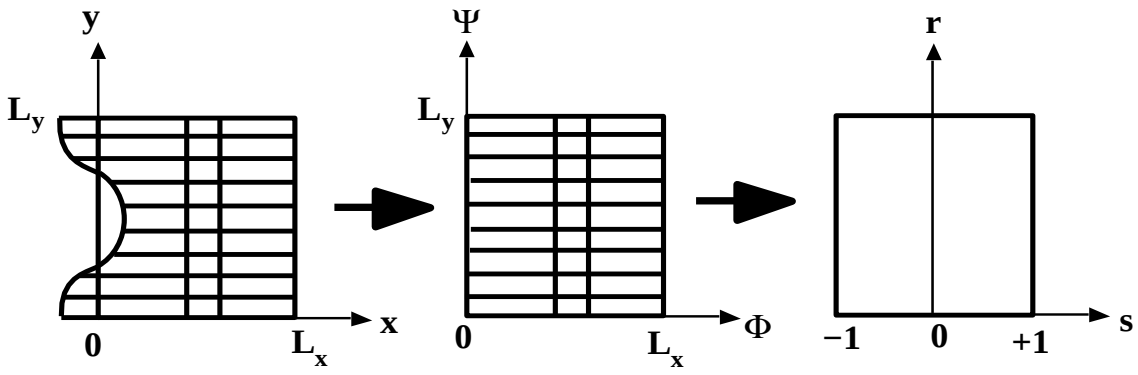

Figure 4.2: Transformation from the physical to the intermediate domain, and from the intermediate to the computational domain.

At this point it is important to test the actual accuracy of these transformations. Depending on the motions modeled, the accuracy of the results plays an important factor especially when analysing physical and numercial features of the results. Two sets of results will be presented here, in order to serve as a simple test (Figure 4.3 and Figure 4.4).

The test procedure is directly testing the accuracy of the three transformations for some specified function. First, a function $f(x)$ is chosen. Using (4.26) and the reversed Gauss-Lobatto points, this function is transformed from the physical domain to the computational domain ($f(x) \rightarrow f(s)$). This is used as input for the numerical differentiation. Then, since the actual function $f(x)$ is known, its derivative is obtained in the physical domain, and using (4.27) and (4.28) it is transformed to the computational domain ($f_x \rightarrow f_s s_\phi \phi_x$). Finally, the results obtained from the last step are compared to the numerical results.

In the two test cases the domain length $L = 5$, the grid point number $NX = 32$, and as test functions $f(x) = \sin(x)$ and $f(x) = e^x$ have been used. It is evident from the results that the last transformation does not perform well enough at the domain ends (Figure 4.3(c) and Figure 4.4(c)). The others show a much better performance throughout the whole length L (Figure 4.3(a)-(b) and Figure 4.4(a)-(b)). The performance of the three transformations does not change for different L and NX values. For the last transformation the results do not improve for a different p value, $p = 0.999$ is essentially the best value that can be used for this transformation. In the light of these tests, the last transformation will not be used in this study.

As a result of the two transformations, the governing equations now read

$$\begin{aligned}
\beta_t^- + [s_t + s_x(u-c) + s_y v]\beta_s^- + v\beta_r^- - c\gamma_r - s_y c\gamma_s &= 2s_x c_o c_{o_s} + F, \\
\beta_t^+ + [s_t + s_x(u+c) + s_y v]\beta_s^+ + v\beta_r^+ - c\gamma_r - s_y c\gamma_s &= 2s_x c_o c_{o_s} + F, \\
\gamma_t + [s_t + s_x u + s_y v]\gamma_s + v\gamma_r &= -g\eta_r - g s_y \eta_s + G, \\
h_t + h_s s_t = \left[\nu(|\mathbf{u}| - v_c)^b \left(\frac{u}{|\mathbf{u}|} + \gamma' h_s s_x + \frac{v}{|\mathbf{u}|} + \gamma'(h_r + h_s s_y)\right)\right]_s & s_x \\
+ \left[\nu(|\mathbf{u}| - v_c)^b \left(\frac{v}{|\mathbf{u}|} + \gamma'(h_r + h_s s_y)\right)\right]_r &
\end{aligned} \tag{4.32}$$

where $|\mathbf{u}| = (u^2+v^2)^{1/2}$ and v_c is the critical velocity. Note that at the shoreline $c = \sqrt{gd} = 0$.

For the s direction the derivatives are computed using Chebyshev collocation, as stated earlier. These calculations can be carried out using a Fast Fourier Transform routine. Due to the form of this method no special boundary treatment is necessary in this direction. A Fourier collocation is used in the r direction. Since Fourier basis functions used in this method naturally satisfy periodicity, no additional condition is needed for the longshore r direction.

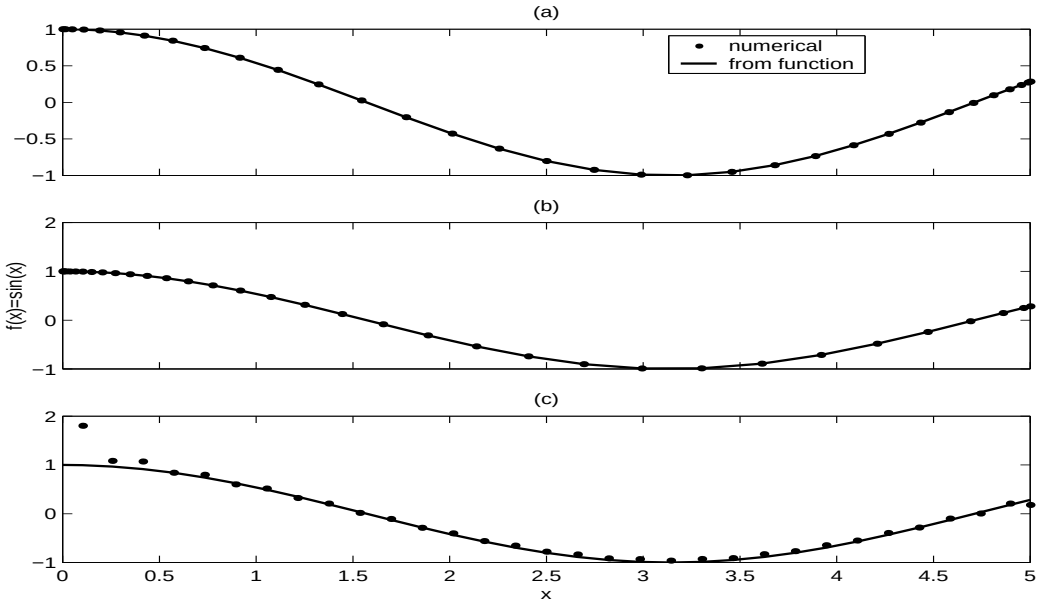

Figure 4.3: Comparison of three transformations used in the model for $f(x) = \sin(x)$. (a) Transformation (4.29), (b) Transformation (4.30), (c) Transformation (4.31).

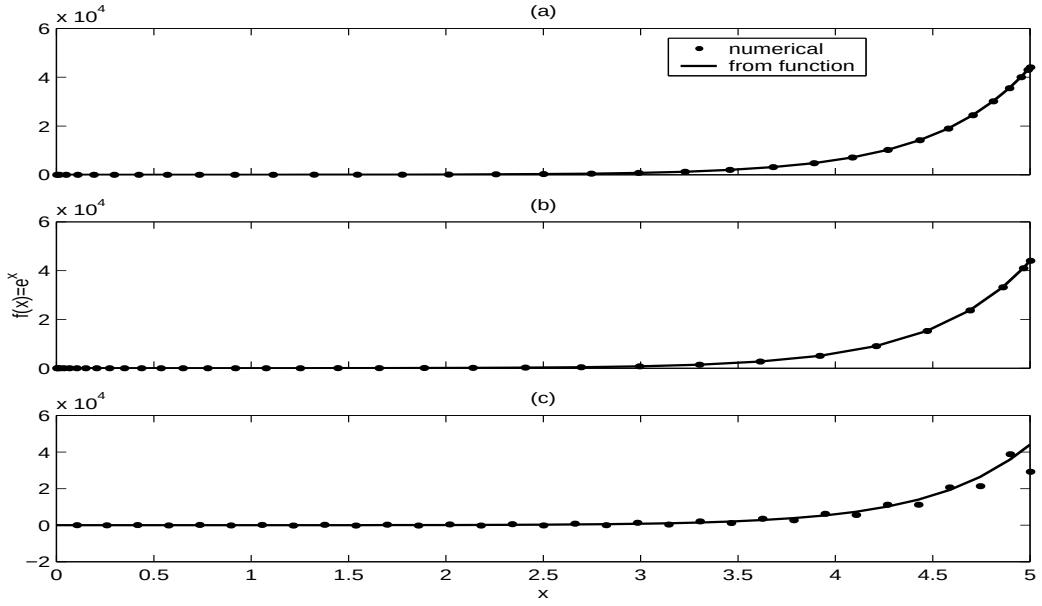

Figure 4.4: Comparison of three transformations used in the model for $f(x) = e^x$. (a) Transformation (4.29), (b) Transformation (4.30), (c) Transformation (4.31).

4.3.3 Boundary Treatments

The treatment of the moving shoreline is based on an Eulerian approach with deforming grid. Such models usually involve moving grids where one boundary of the grid tracks the shoreline position. Since at the shoreline $x = \zeta(y,t)$, a kinematic condition at that boundary can be written

$$\zeta_t = u^s - v^s \zeta_y \tag{4.33}$$

where $d = h + \eta = 0$ on this boundary.

Returning to the momentum equations, the velocity of the shoreline can be determined using the x-momentum equation

$$u^s_t + [s_t + s_x u^s + s_y v^s] u^s_s + v u^s_r = -g s_x \eta^s_s + F^s \tag{4.34}$$

where the superscript s denotes variables at the shoreline. After using the grid transformations, the kinetic condition becomes

$$\zeta_t = u^s - v^s \zeta_r \tag{4.35}$$

where $d = h + \eta = 0$ on $s = -1$. The position of the shoreline is tracked by including equations (4.34) and (4.35) in the time stepping scheme. Results of this model using a moving shoreline can be found in Özkan-Haller and Kirby (1997) and Özkan-Haller (1997).

As mentioned before, it is also possible to replace the moving shoreline with a fixed wall of some specified depth. In that case the essential condition of 'no flow' through the boundary is imposed. The same condition can be applied to the offshore boundary. Considering the no flow condition, the sediment transport rates perpendicular to the walls are also set to zero automatically. For the moving shoreline case it is difficult to specify a condition for the transport rates. Since the water depths closer to the shoreline are significantly small any change of batymetry at those points would most probably cause problems at the shoreline, like drastic changes of the shoreline or bed features sticking out of the water. This model is currently not able to handle any island type of formations which could arise due to changing bottom. One preliminary solution could be treating the shoreline as a wall and specifying a zero sediment transport rate. Although not necessarily preventing islands to form, this would prevent at least excessive cross-shore transport at those points thus taking care of some of the problems that might arise at the shoreline, while still including the effects of a moving shoreline.

At the offshore boundary an absorbing-generating boundary condition allowing waves to enter and exit the domain can be specified. This method is based on the study by Van Dongeren and Svendsen (1997), and details of the formulation can be found in Özkan-Haller (1997).

Chapter 5

EVOLUTION OF BED INSTABILITIES IN A FLOWING STREAM

This chapter discusses numerical results for bed evolution and flow field simulations in a rectangular channel. The dispersion relationship obtained in Chapter 3 is used in the model runs in order to compare results based on a stability analysis theory. The analysis outlined in Chapter 2 along with field and laboratory observations serve as guidelines in interpreting the numerical results. The rectangular channel consists of two impermeable, rigid walls located at both ends of the domain; at the shoreline and at the offshore boundary in this model. The basic flow consists of a constant velocity profile streaming along-channel. There are no waves within the domain and no lateral mixing processes. This basic case has been chosen in order to evaluate the performance of the coupled model in reproducing the bed and flow field instabilities, and to identify the results in the simplest possible mathematical setting.

First, a brief outline of the model implementation for this case is presented. This is followed by a test case consisting of an unperturbed regular channel with a cross-channel bed slope. The next section presents results for the most unstable wave number of the bed perturbation based on the linear dispersion relationship. Parameters for this case have been chosen based on Chapter 2. Results for different channel lengths are also included in this section. Next, the cases for wave numbers slightly larger and smaller than the most unstable one follow. In these simulations, the effect of different channel lengths has been addressed as well. Different model parameters that may have a significant impact on the bottom evolution are discussed in the next section, which is followed by results obtained for different initial bottom perturbations and the resulting bed evolution. After this section comparisons to laboratory measurements and observations are presented, followed by a summary of the results.

5.1 Model Implementation

Based on the equations outlined in Chapter 2 and 3, forcing and friction terms which describe flow in a rectangular channel are used in the momentum equations outlined in Chapter 4. In order to obtain an along-channel flow a mild slope of i_o is introduced. The forcing and friction terms are the same as in equation (2.2). The sediment transport equation was described in Chapter 4.

A rectangular channel is defined by introducing walls at the shoreline and at the offshore boundary. Periodicity in the along-channel direction is imposed. With this format the y-direction points along-channel and the x-direction points across-channel in the model. Due to the two walls there is no moving shoreline. The coordinate transformation which concentrates grid points towards the walls is chosen.

Values of the parameters like the channel width and depth, or the friction factor involved in this problem are specified in each section. A channel width-to-depth ratio R of 44, and a basic flow velocity of $1m/s$ has been used in most of the runs. The parameter ν in the transport equation is usually taken as 0.1 which corresponds to a morphological time scale of approximately 3 hours for $U = 1m/s$, $R = 44$, and $b = 6$.

In some of the following cases the model starts with initial conditions of zero flow $u, v = 0$, and no water surface elevation $\eta = 0$. In most of the cases the sediment transport process is activated after the flow field has developed. The flow field can develop in a very short period. In order to minimize the simulation time, in some cases the basic along-channel flow velocity has been defined as the initial condition. No critical velocity v_c has been used in these runs.

5.2 Test Case: Straight Channel with Cross-channel Bed Slope

In this simulation a rectangular channel, uniform in the along-channel direction, with a cross-channel bed slope of 1/1000 is used. The channel width is $220m$ and it has a depth of $5m$ on one end reaching to $5.22m$ on the other. The channel length L_y has been arbitrarily chosen to be $1402.5m$. In order to achieve a uniform flow of $1m/s$, $i_o = 6.11 \times 10^{-5}$ has been used. The parameters ν, b and γ' are 0.1, 6 and 1, respectively. The friction factor is $c_f = 0.003$. The domain consists of $(NX = 32, NY = 4)$ grid points. Due to the uniform channel the whole process taking place within the channel can be considered as one-dimensional, so only the cross-channel profiles are considered. That is also the main reason for the choice of a lower number of grid points in the along-channel direction.

The channel profile adjusts itself towards equilibrium. This can be seen in Figure 5.1. The initial channel profile is shown as the dash-dotted line and the evolving profiles are shown as solid lines. The eroded sediment from the upper portion of the profile is deposited to the lower portion. This is mainly due to the slope effect since no significant cross-channel velocities develop and everything is periodic along-channel. Higher along-channel transport rates correspond to deeper water depths, and the maximum cross-channel transport rate is in the mid-section of the channel. All this can be seen in Figure 5.2, where the cross-channel and along-channel sediment transport rates, and the corresponding depth change at four

different time levels are shown. As equilibrium is achieved the magnitude of the transport rates and the amount of depth change decreases significantly. Note also the symmetric shape of these curves which proves that the same amount of sediment transported from the upper portion of the channel is deposited to the lower portion. The volume of sediment transported matches the sediment transport rates.

In 40 hours the profile has almost reached equilibrium, the amount of depth change decreases in time and changes are not visually detectable from the profiles. This is more evident in the time series plot in Figure 5.3. In this figure time series of u, v and h at the deeper wall section of the channel are shown. Note that u values are negligibly small and that the along-channel velocity v reaches its value of $1m/s$ corresponding to the specified i_o and c_f. Note also how the channel depth at that point slowly moves towards equilibrium. For this plot the channel depth values are shown as positive values, so decrease in h corresponds to deposition.

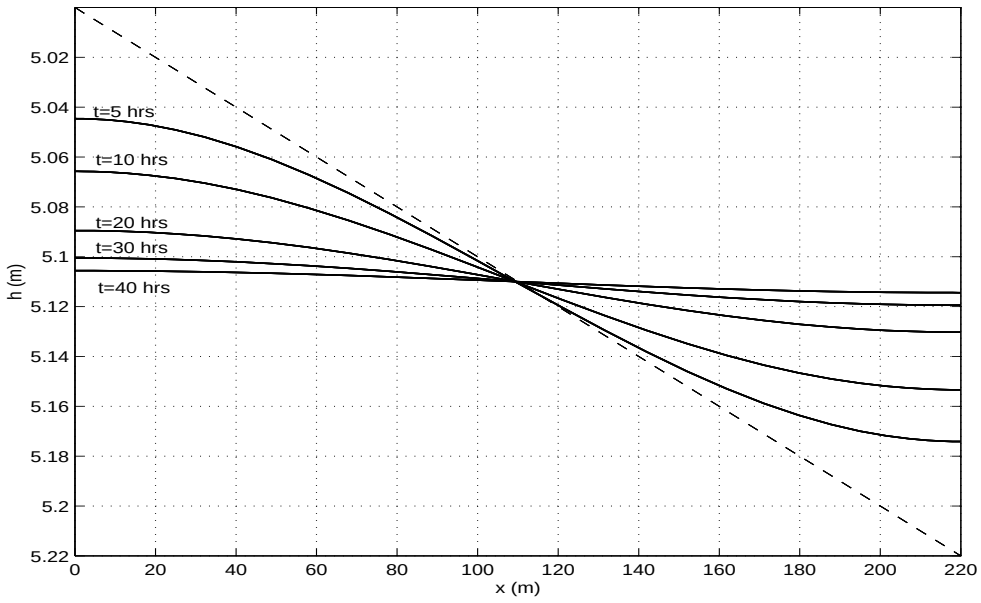

Figure 5.1: Test case: Cross-channel profile reaching equilibrium in time. (——) evolving profiles, (– - –) initial profile.

This test simulation proves that the sediment transport part is implemented correctly into the hydrodynamic model. The basic features of profile evolution corresponding to the given geometry and flow conditions have been simulated.

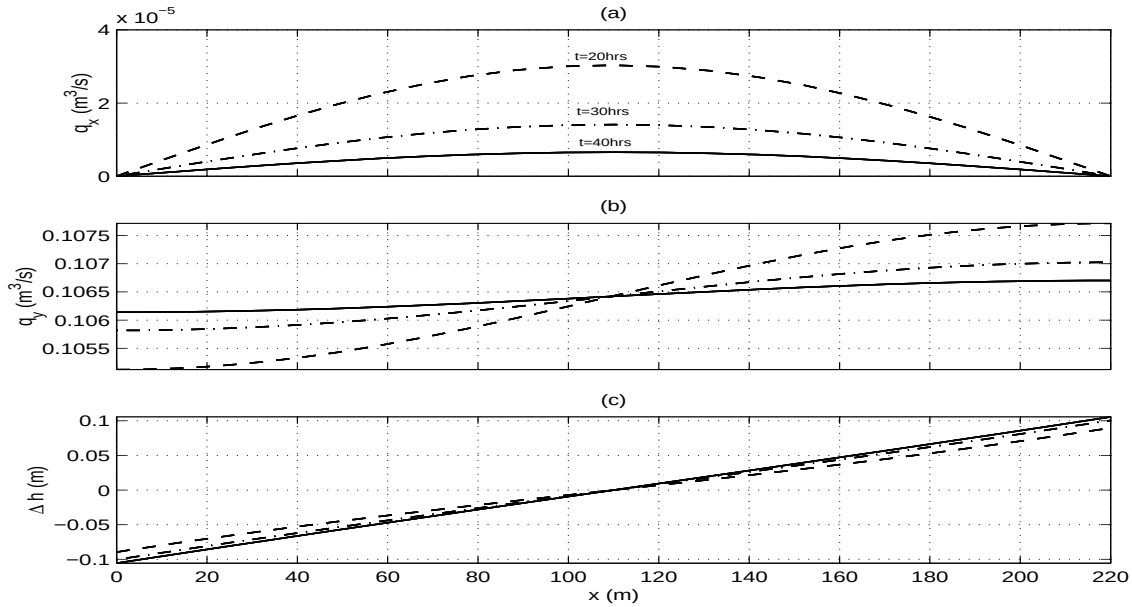

Figure 5.2: Cross-channel profiles of (a) cross-channel sediment transport rate, (b) along-channel sediment transport rate and (c) depth change at different time levels.

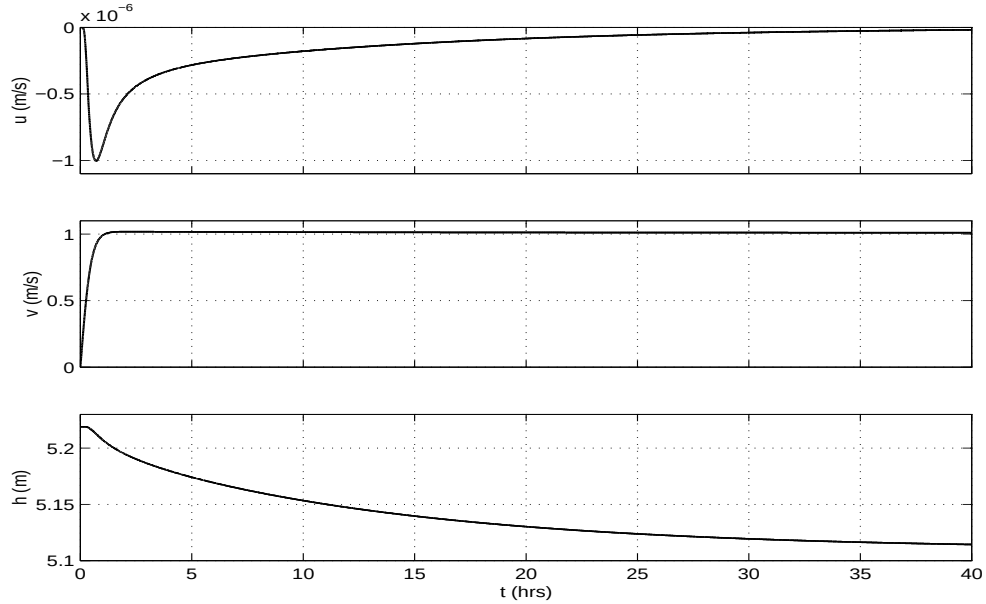

Figure 5.3: Time series of u, v and h at $(x, y) = (219m, 0.5L_y)$ for test case.

5.3 Simulations for the most Unstable Wavenumber, k_{max}

Using the dispersion relationship for a 2D channel derived in Chapter 3, it is possible to obtain the most unstable wavenumber and corresponding frequency of bed perturbations for a specified channel and flow. In this section we are interested in the long time evolution of the bedforms coupled to the flow field, when initially wave like disturbances of the bottom are included. For this purpose the dispersion curves for a case where growth of instabilities occurs are used. In Figure 5.4, the dispersion curves for a channel with the same parameters as in the previous simulation are shown, except in this case there is no cross-channel slope. Note that the values are nondimensional. These values are used to determine the initial bed perturbation.

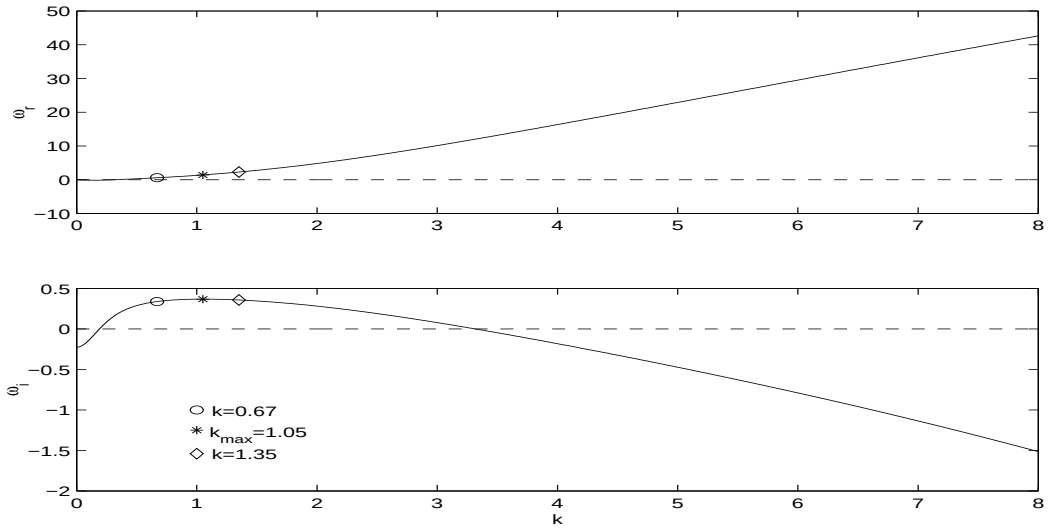

Figure 5.4: Dispersion curves for a 2D channel. Parameters: $U = 1m/s$, $b = 6$, $v_c = 0$, $\gamma' = 1$, $R = 44$, $c_f = 0.003$. Note the most unstable, the slightly larger and slightly smaller wavenumbers shown with different symbols on the curves.

Based on the stability analysis reviewed in Chapter 2, the first mode of the bed perturbations is in the form of a sinusoidal function in the y-direction (see equation (2.9)), as well as in the x-direction. Using this form and imposing a first mode sinusoidal form in the x-direction, the following initial bed perturbation can be used

$$z_b(x, y, t = 0) = z_c cos(d_{c1}x)cos(d_{c2}y) \tag{5.1}$$

where z_c is the amplitude, d_{c1} and d_{c2} are factors controlling the wavenumbers of the bed perturbations in both directions. Depending on these values, the perturbation wavelengths are λ_x and λ_y in the cross-channel and along-channel directions, respectively.

5.3.1 Results for $L_y = \lambda_y$

For this case an amplitude of $z_c = 1$ has been used. The channel bottom can be considered as covered with small sand waves. The values for $d_{c1} = \pi/L_x$ and $d_{c2} = k$, where k is the

wavenumber of the sand waves have been chosen such that one perturbation wavelength λ_y fits into the domain in the along-channel direction and one half fits in the cross-channel direction. This corresponds to a wavelength of $\lambda_y \approx 1316.5m$ in the y-direction. A three-dimensional figure of the perturbed bed is shown in Figure 5.5. In order to maintain spatial accuracy collocation points of $(NX = 32, NY = 64)$ have been used. This grid uses 64 points per wavelength which, based on the study by Özkan-Haller (1997), should maintain a high accuracy.

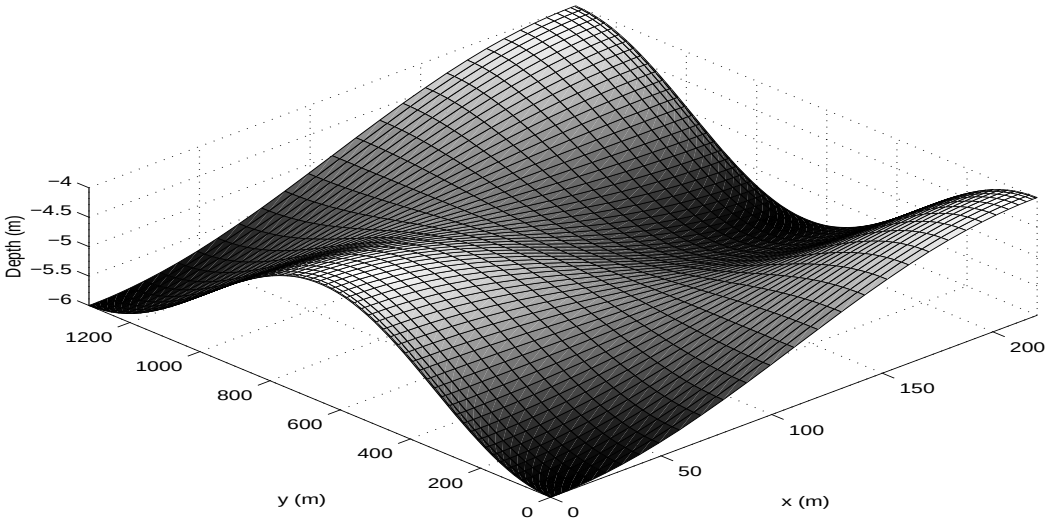

Figure 5.5: Initially perturbed bed configuration for $L_y = \lambda_y$, $k_{max} = 1.05$.

The simulation is carried out for 40 hours. Results of the bed evolution are shown in Figure 5.6. Significant changes occur after the first three hours, which roughly corresponds to the previously calculated morphological time scale. The bedforms start to change orientation and attain an oblique structure. This structure becomes more evident in the following three hours. The increasing amount of erosion and deposition happening after approximately six hours which can be seen in the depth contour changes, results in the growth of the sand waves. Also note how the $6.5m$ and $7m$ contours representing eroded points and the $3.5m$ contours representing points of deposition become even more evident after 7 hours.

Fluctuations around the steep wave front form after 14 hours. At this point a shock wave type of structure has already developed. The steep slope of the sand wave fronts may be causing the fluctuations. This can be seen in Figure 5.7 where the three-dimensional view of the evolving bed is shown. The correct aspect ratio of the channel in this figure has been altered in order to obtain a clear plot of the bedforms. The fluctuations are in the form of depth contour separations. Although hard to notice, the $3m$ contours first separate at 17 hours and more significantly after 31 hours. We are not exactly sure if this is caused numerically or if it has some physical significance. It is noted that the steep slope may be physically unrealistic. This slope reaches approximate values of $0.0667 - 0.0875$. Such steep sand waves can be expected to collapse. Since the model is not able to handle such motions the depth contours may have started to fluctuate. The parameter γ' in the transport equation governs the degree of the slope effect on sediment transport. This parameter is chosen as a

constant value and depends on the angle of repose of the bed material. Considering that in the process of transport the sand grain distribution of the bedforms may change, it can be expected that the angle of repose will also change accordingly. Depending on the changing angle of repose, a varying γ' could produce a more realistic wave front. This would require a more sophisticated transport equation which includes the effect of changing sediment grain distribution and its relation to the angle of repose and γ'. The effect of changing γ' has not been investigated in this study.

The sediment transported from the lower points towards the higher points of the bedforms increases in time, so deposition spreads over a larger area in the domain (note the red areas in the pseudocolor contour plots). After 20 hours the initial sand waves have developed into a considerable shock wave form with a significant bar front. The highest point of sand waves reaches a value of about 45.6% of the unperturbed channel depth (a depth contour of $2.7176m$) in 40 hours. The deepest point is about 8% larger than the unperturbed channel depth (a depth contour of $10.3963m$).

This type of pattern forming in alluvial channels is referred to as alternate bars. The results are comparable to the first stages of the development of free meandering from a straight channel or to similar bedforms frequently observed in laboratory flume experiments (Chang *et al.*, 1971; Schumm and Khan, 1972; Parker, 1976; and Uchijima, 1990). The channel topography and two channel cross-sections along with an idealized schematic of this motion taken from the study by Chang *et al.* (1971) are shown in Figure 5.8. Note how the shape of the bar front and the cross-sections are similar.

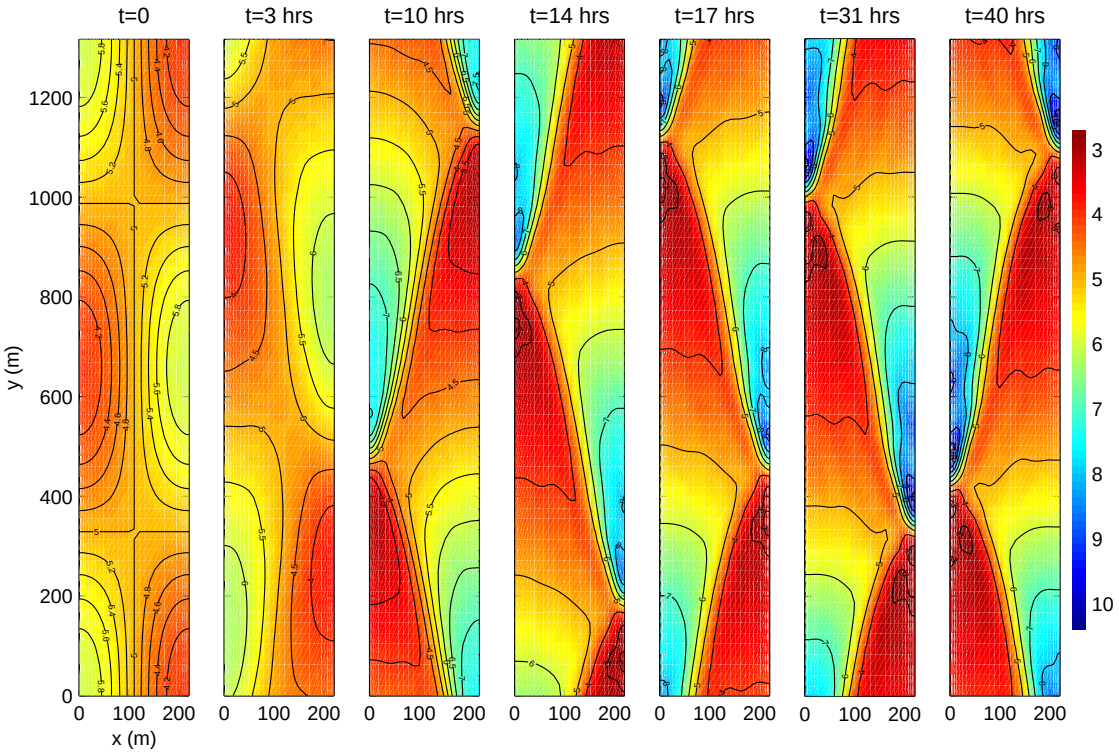

Figure 5.6: Simulated bed evolution for $L_y = \lambda_y$, $k = 1.05$.

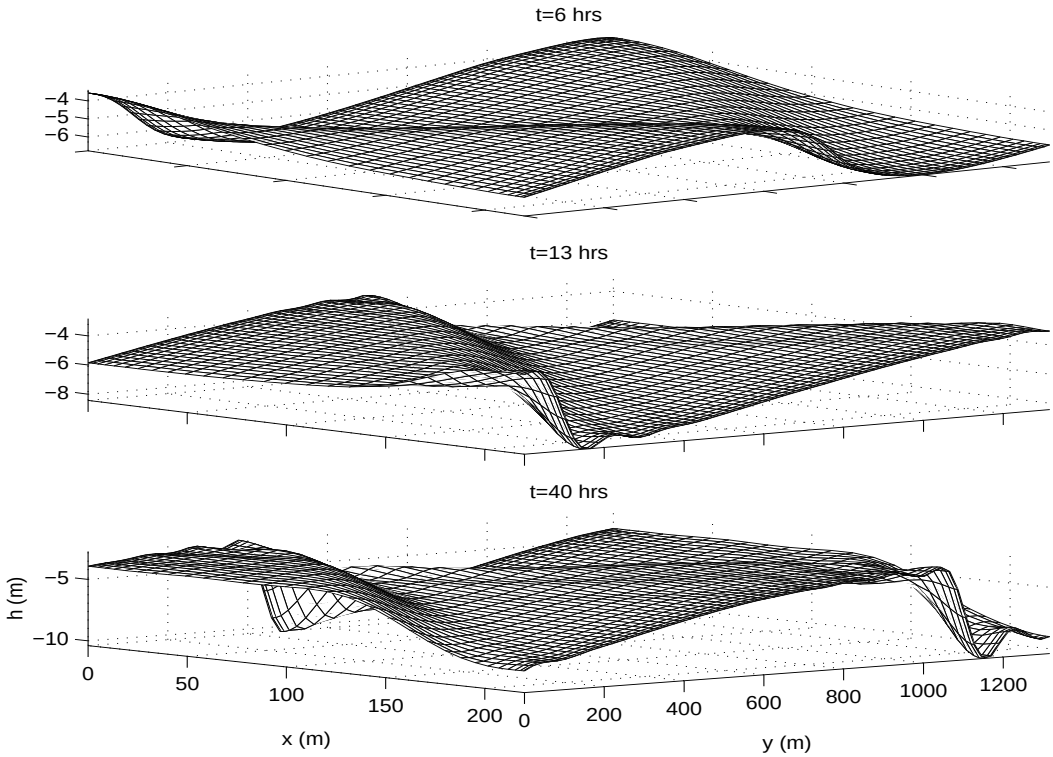

Figure 5.7: Snapshots of simulated bed evolution in 3D for $L_y = \lambda_y$, $k_{max} = 1.05$.

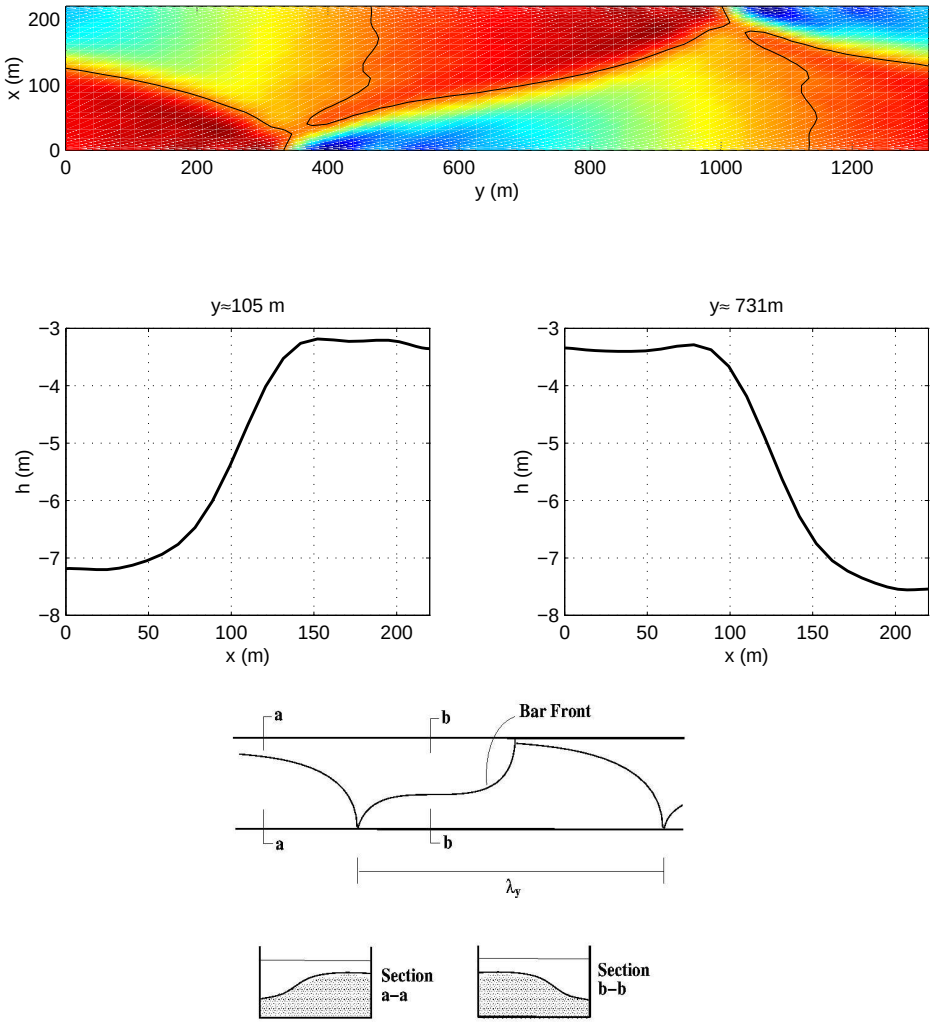

Figure 5.8: Top panel: Simulated topography at $t = 40hrs$. Mid panel: Channel cross-sections taken at two along-channel locations. Bottom panel: Idealized alternate bar pattern in alluvial channels (after Chang *et al.*, 1971).

Time series of u, v and h taken at the mid-section of the channel also show that the initial perturbations periodically grow in time (Figure 5.9). The flow instantenously responds to the bed evolution. It is noted that the cross-channel velocity u continues to grow along with the channel depth h. Upon reaching its basic value of $1m/s$ the along-channel velocity v starts to fluctuate around this value. The fluctuations seem to have reached finite amplitude as growth cannot be detected within visual resolution. From the time series of h, an average estimate of the characteristic period of the bed motion can be computed. This is a very rough estimate and is obtained by determining the time lag between each peak of the h fluctuations. It is important to note that these time series are taken at the mid-section of the channel and therefore the period obtained will be twice the period corresponding to the time series at a point closer to the walls. Due to the bedform propagation pattern at the middle of the channel, as two peaks pass through one point only one passes through at a point closer to the sides of the channel where in fact propagation of the alternate bars can be better observed. This is also the reason for the difference in the periods of the u, v and h fluctuations in the time series plot.

The average period value is given as $T_{av} \approx 15hrs$. This corresponds to a frequency of $\omega_{av} = 1.17 \times 10^{-4} rad/s$. The nondimensional frequencies obtained from the linear dispersion relationship are $\omega_r = 1.4299$ and $\omega_i = 0.3687$. Nondimensionalizing the frequency from the simulation with the morphological time scale gives a value of $\omega'_{av} = 1.287$. This value is close to ω_r and it represents the propagation of the bedforms considering that the time series of h represents the topographic waves passing through one point.

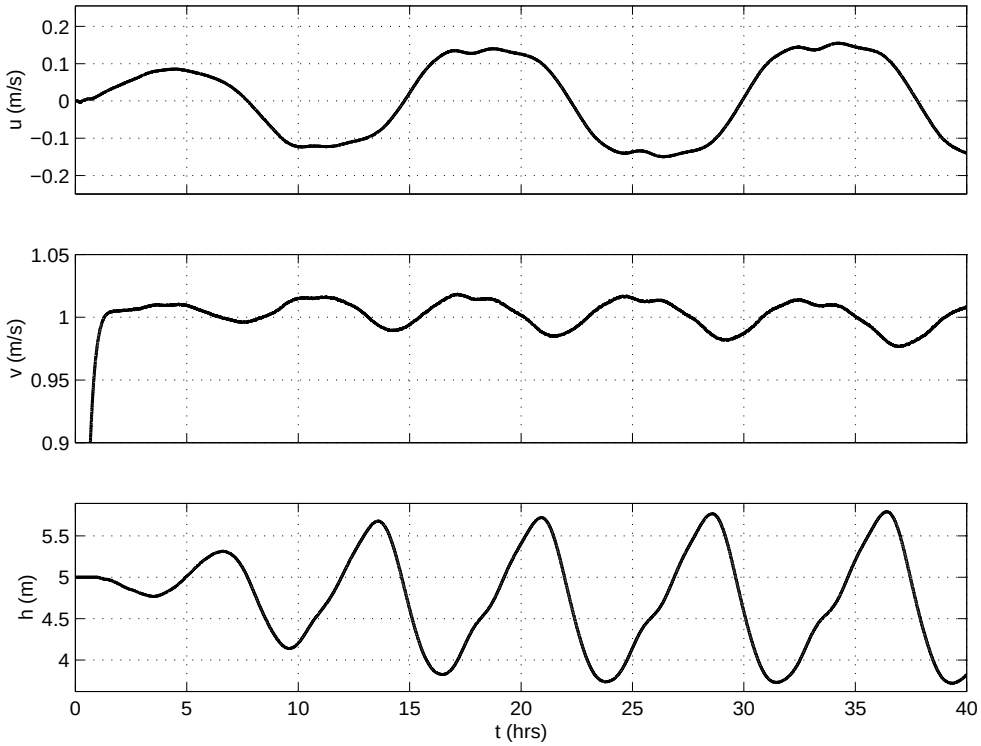

Figure 5.9: Time series of u, v and h at $(x, y) = (110m, 0.5L_y)$ for $L_y = \lambda_y$.

The propagation speed of the bed forms changes from $0.0116m/s$ to $0.0232m/s$ in the evolution process. These speed values have been estimated using a two-dimensional lag-correlation applied over the entire channel topography for every hour. Again, using the information from the dispersion relationship the propagation speed can be computed as $C'_{bed} = 0.02072m/s$. A speed estimate can also be obtained by using the wavenumber of the bedforms and the frequency computed above, which gives $C_{bed} = 0.0245m/s$. The last two values are surprisingly close. The results obtained from the lag-correlation show changing values rather than a constant value as predicted by the linear stability analysis. This is due to nonlinear interactions in the evolution process, which are not predicted by the linear dispersion relationship.

The flow field adjusts itself according to the evolving bottom. The meandering of the along-channel flow gains more strength in time, as bed features grow and the bar front forms. Plots of the velocity field on top of the corresponding vorticity and bottom contours are shown in Figure 5.10 . The velocities are plotted every fourth collocation point in each direction in order to maintain a better visual resolution. Negative vorticity shown in blue color represents clock-wise rotation of the flow. Positive vorticity shown in red is the opposite. As the bed evolves the vorticity increases together with the velocities, especially along the bar front. Due to the relation between the flow velocities and sediment transport rates, the general flow structure matches the propagation and growth of the bedforms.

5.3.2 Results for $L_y = 2\lambda_y$

In order to investigate the effect of channel length on the bed evolution, another simulation has been run where all parameters are kept the same as before and the channel length L_y is doubled so that two wavelengths of the bed perturbation fit into the domain, so now $L_y = 2633m$. Another difference is the initial condition on the flow field. In order to speed up the development of the flow field the basic along-channel flow velocity is defined as the initial condition. The same number of grid points is used in this simulation.

Comparison of the time series for this case and the previous case show no large difference magnitude-wise (Figure 5.11). The same structure is attained, the only difference being the lag between the fluctuations. As will be shown in the next case the reason for this lag is neither the number of collocation points which for this case is 32 per wavelength in the along-channel direction, nor the initial condition imposed on the along-channel velocity. The same difference in the period happens for the next case where a longer channel and higher number of grid points are used. The general trend of these fluctuations is that their frequency decreases as the channel gets longer.

The frequency information from the dispersion relationship is essentially the same for this case, since the bed perturbation has the same wavenumber. The nondimensional average frequency of the bedforms obtained from the time series is $\omega_{av} = 1.216$. Compared to the previous frequency obtained, they are close values and they both mainly represent propagation of the bedforms. The propagation speed range obtained by lag-correlation is $C_{bed} = 0.0116 - 0.0232m/s$. The speed obtained using the wavenumber and frequency is $0.02317m/s$.

The bedform evolution is shown in Figure 5.12. The bedforms in this simulation evolve

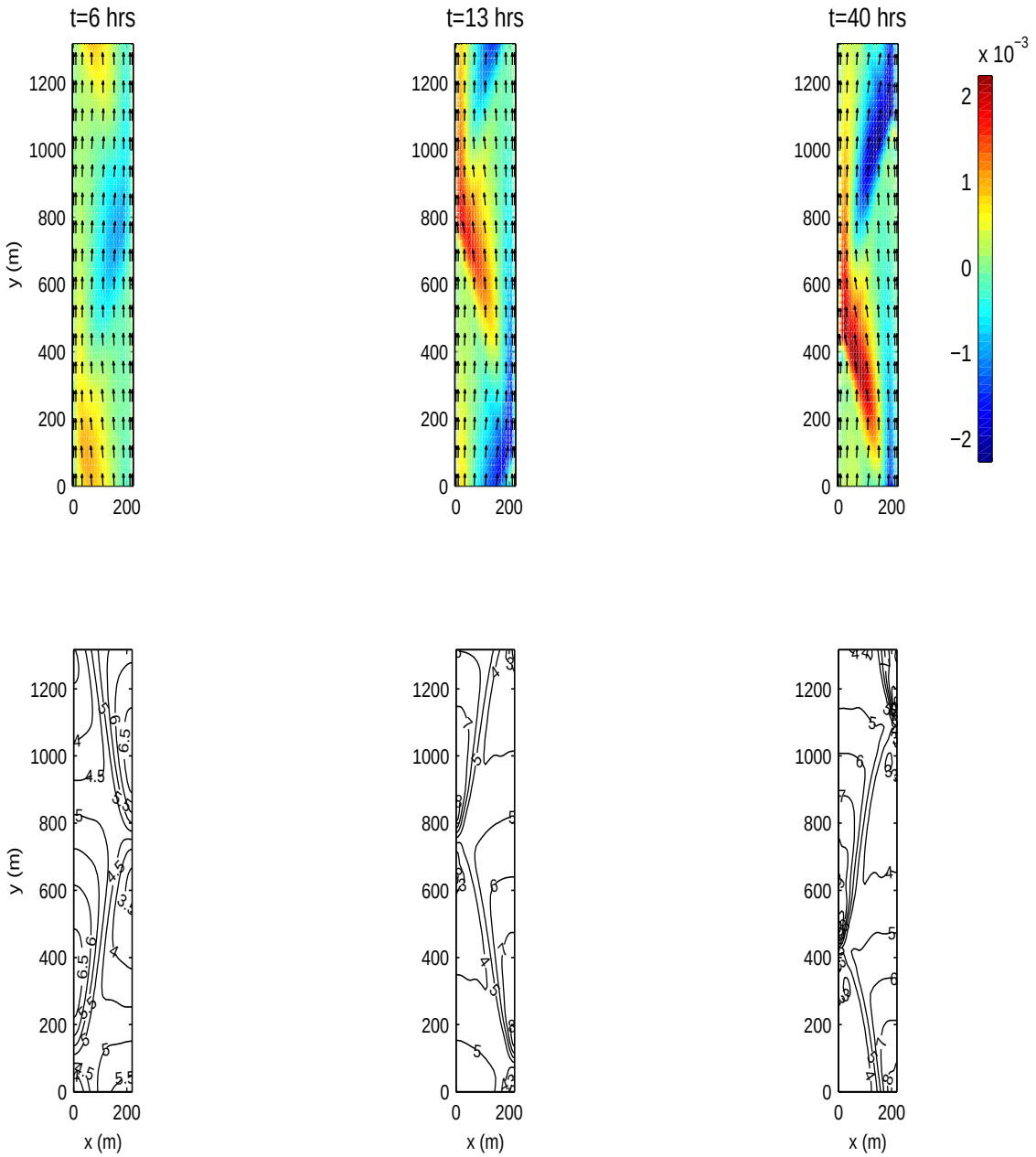

Figure 5.10: Snapshots of the velocity field, corresponding vorticity (top panel) and depth contours (bottom panel) for $L_y = \lambda_y$, $k = 1.05$.

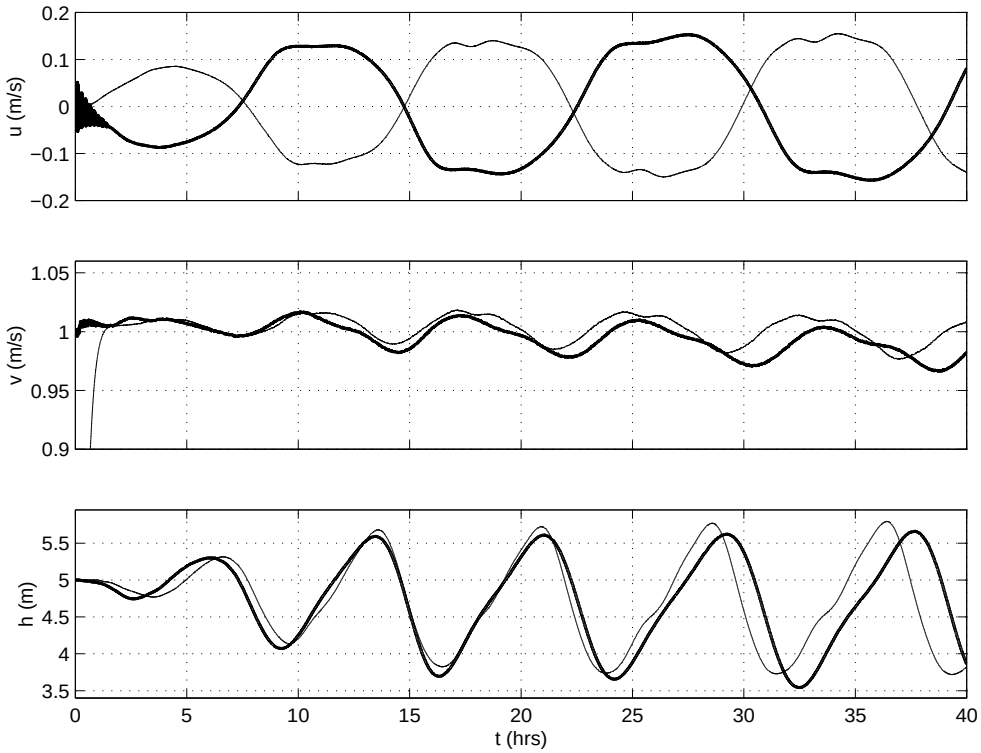

Figure 5.11: Time series of u, v and h at $(x, y) = (110m, 0.5L_y)$ for (——)$L_y = 2\lambda_y$ and (——)$L_y = \lambda_y$.

to an alternate bar pattern very similar to the previous case. Although very similar at a glance, there are some differences in the form of contour separations. Similar fluctuations form around the same time step as before. It is also possible to observe contour pairing in these simulations. Note at 16 hours the $3m$ contour forming at the lower right hand side of the domain starts moving towards the next $3m$ contour. As it reaches the next contour it also spreads over a larger area and it pairs with it at 25 hours. At 35 hours the contours separate again. Similar behaviour occurs for the rest of the $3m$ contours within the domain. Most probably, we would have been able to observe pairing of contours for the previous case as well, if the domain length was longer. From these two simulations it is obvious that separation and pairing of contours is more likely to happen at higher sand wave amplitudes, which would correspond to lower water depths. At these points the discharge increases due to lower flow depths and this pushes the higher points of the bedforms forcing the observed behaviour. The amount of erosion and deposition is slightly larger in this case. After 40 hours the deepest contour is $10.5154m$ and the lowest contour is $2.2896m$.

The flow field shows a similar behaviour to the previous simulation. In Figure 5.13 the velocity vectors are plotted on top of the vorticity at three different time levels. Here again, vectors every fourth grid point are shown for a better resolution. Since the channel length is doubled now, the number of meanders is also doubled. With the initial along-channel velocity the flow field develops faster than before causing more transport to happen in a shorter duration. Considering also that the bedforms have more freedom in developing

due to the longer channel, this result is not unexpected. The magnitude of the maximum vorticity shows almost no change. Neither the flow field, nor the bed evolution have been significantly affected by doubling the channel length.

5.3.3 Results for $L_y = 4\,\lambda_y$

As a last simulation using the most unstable wavenumber, a channel length of four times the most unstable wavelength has been used in this section. This gives a channel length of $L_y = 5266m$. All other parameters are still the same. For this case, the number of grid points in the along-channel direction is taken as 128 in order to keep 32 points per wavelength. Based on the previous results the bed evolution does not show any significant differences in terms of long time behaviour, therefore only 20 hours of simulation time has been considered.

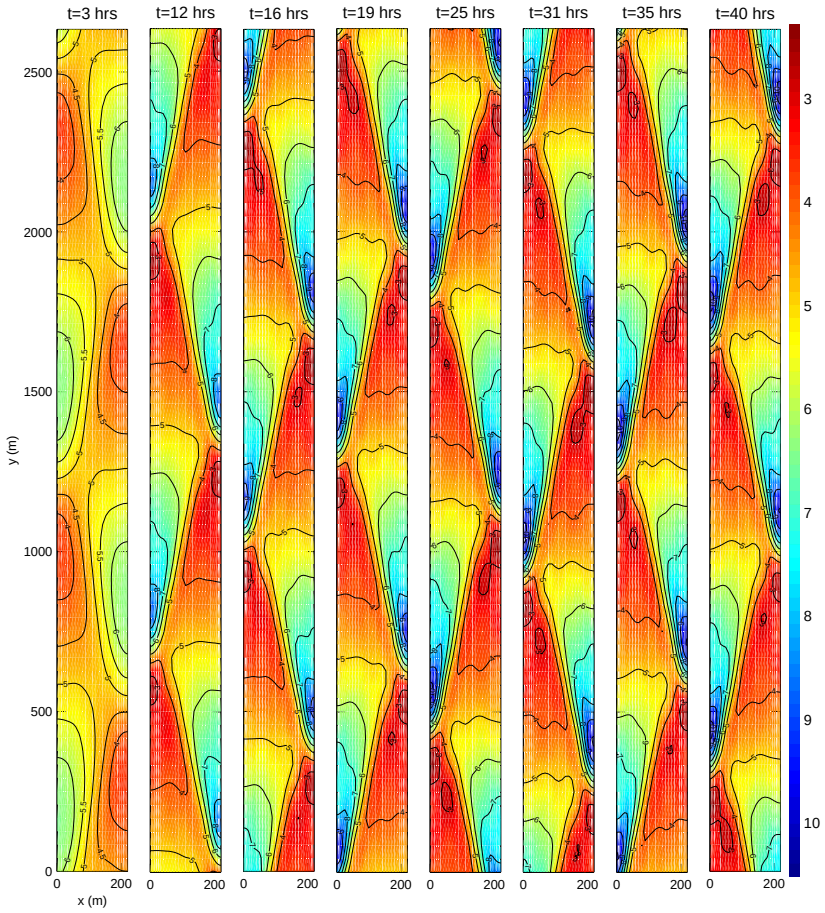

Figure 5.12: Simulated bed evolution for $L_y = 2\lambda_y$, $k = 1.05$.

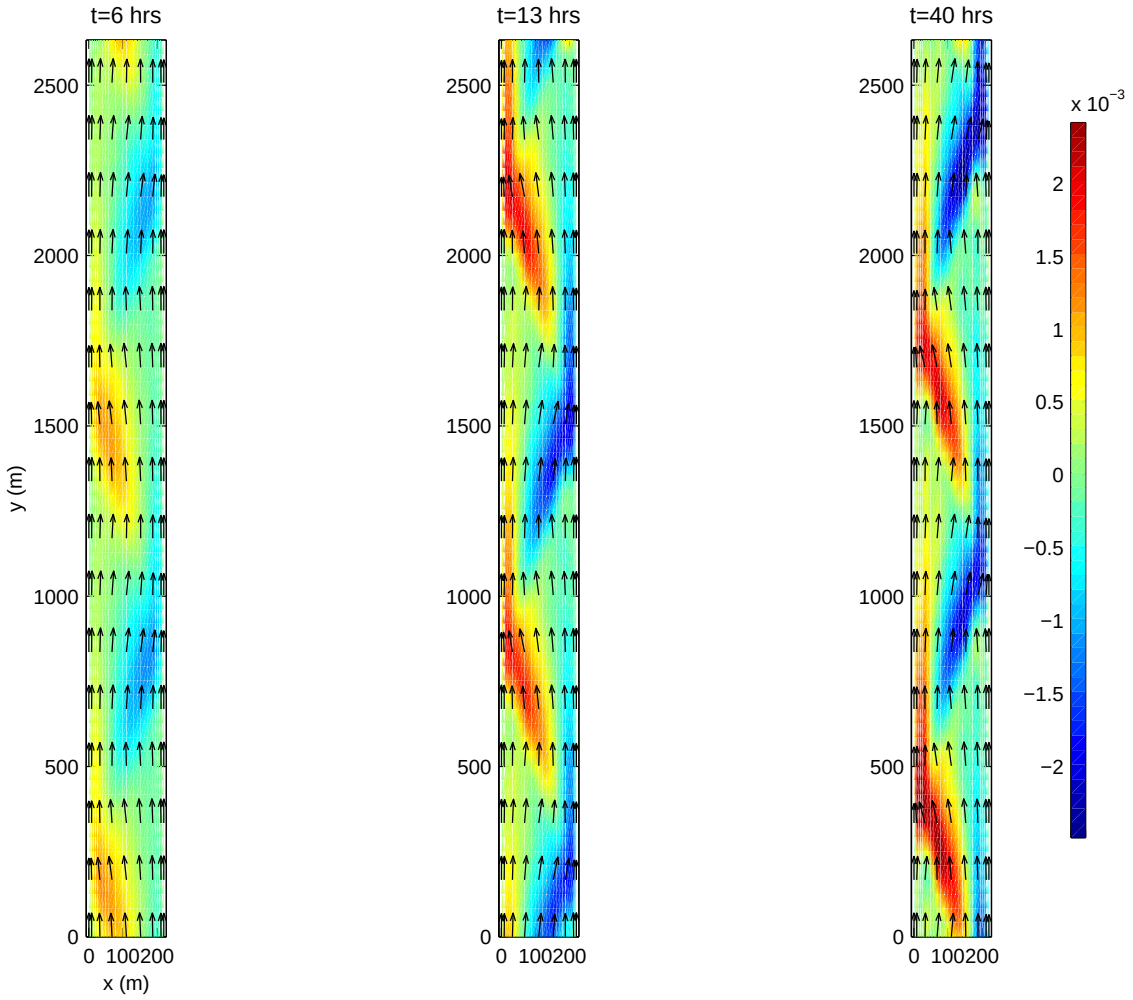

Figure 5.13: Snapshots of the velocity field on top of the vorticity for $L_y = 2\lambda_y$, $k = 1.05$.

The time series do not show any significant difference from the previous simulations, except for a small lag and a slightly faster growth of the bedforms (Figure 5.14). The nondimensional average frequency and the propagation speed obtained from the results are $\omega'_{av} = 1.48$ and $C_{bed} = 0.0282m/s$, respectively. As in the previous simulations their magnitude is close to the values obtained from the linear dispersion relationship. The range for the propagation speed obtained by lag-correlation is $0.0115m/s - 0.023m/s$.

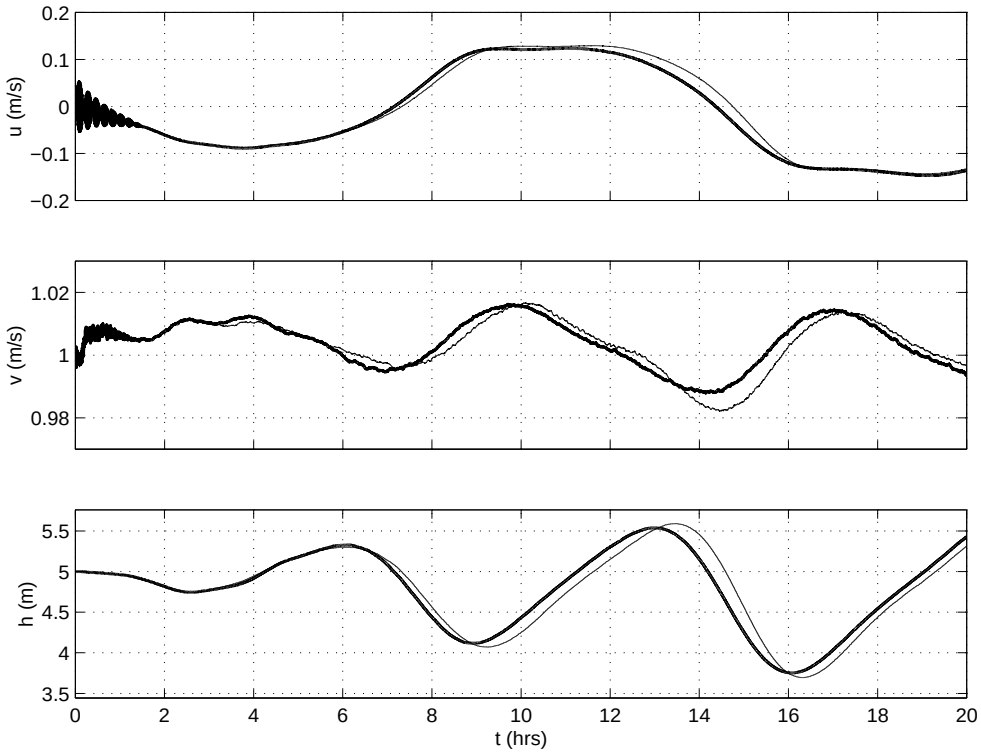

Figure 5.14: Time series of u, v and h at $(x, y) = (110m, 0.5L_y)$ for (——)$L_y = 4\lambda_y$ and (——)$L_y = 2\lambda_y$.

The bed evolution also shows no significant difference. Snapshots of the topography are shown in Figure 5.15. The same alternate bar pattern forms with a higher number of meanders since the channel is longer. One thing to note is the timing and form of the separation and pairing of the $3m$ depth contour. These emerge as fluctuations of the steep wave front. Since a longer channel contains more meanders it is possible that they affect each other such that they cause different pairing and separation events with different timings. This is also evident from the lag between the time series. Due to this lag crest and troughs of the bedforms at a point occur at different time levels.

A comparison of the vorticity and bathymetry of the previous two cases with the present case is shown in Figure 5.15. The first two plots are for the cases where $L_y = 4\lambda_y$ and $L_y = 2\lambda_y$, respectively. In order to be able to make a more accurate comparison only one wavelength is shown in these figures. The last one is from the first simulation where $L_y = \lambda_y$. Obviously the differences are insignificant. Looking at the intensities and general shapes of the vorticity and depth contours, the same type of motion has been formed. The

maximum vorticity magnitudes are the same in each case. Considering both magnitudes of the flow field, bedforms and the alternate bar pattern, longer channel lengths do not affect the results in a significant way. The initial condition on the flow field does not seem to cause any changes either.

5.4 Simulations for a Larger Wavenumber, $k > k_{max}$

In this section a wavenumber larger then the most unstable one is used. The main focus is on how the bed evolution is affected by a larger wavenumber. A nondimensional wavenumber of $k = 1.35$ is chosen from the linear dispersion relationship (Figure 5.4). The same parameters previously defined and the same simulation time of 40 hours are utilized. The collocation points are chosen such that the number of points per wavelength is not less than 32, which maintains spatial accuracy.

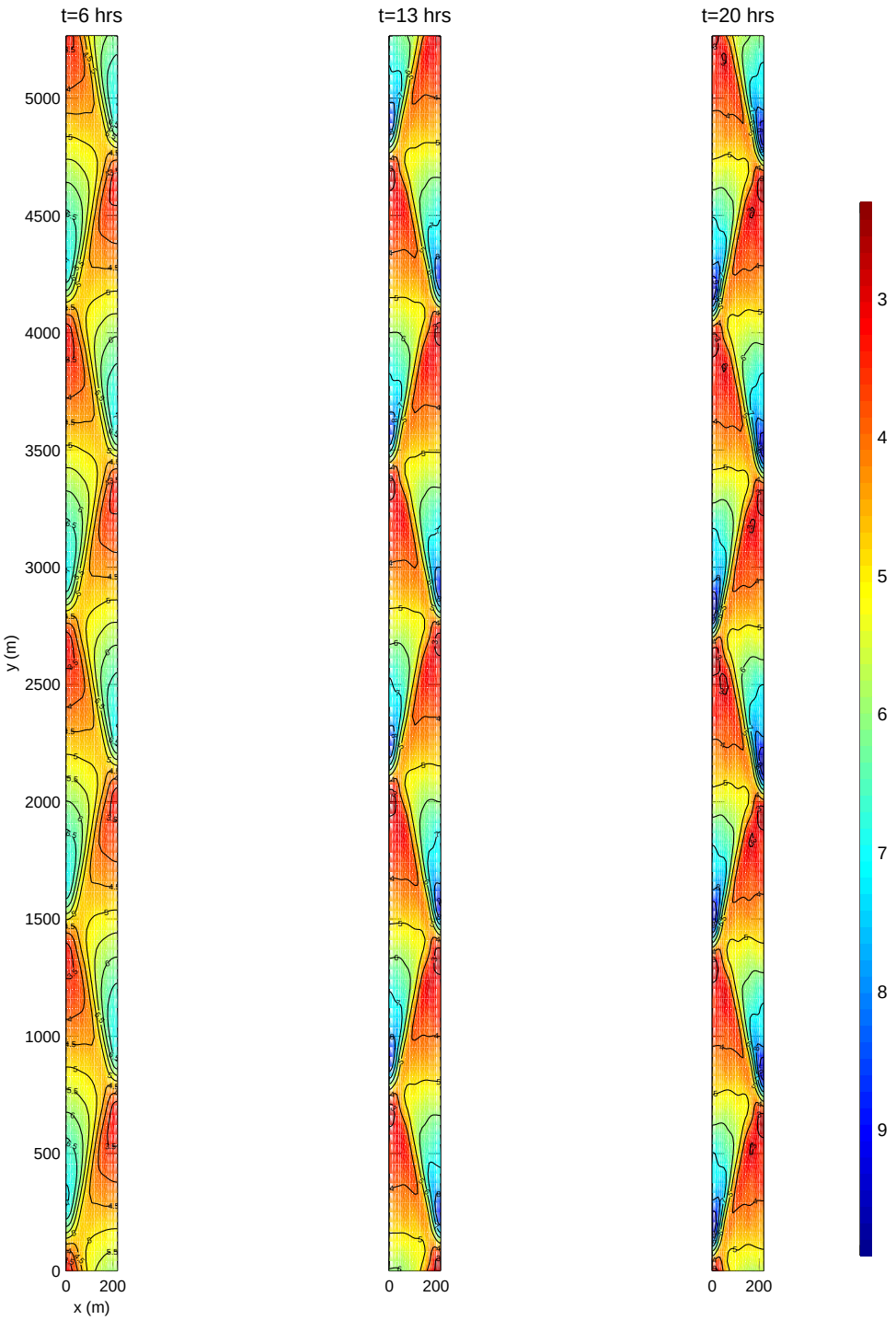

Figure 5.15: Simulated bed evolution for $L_y = 4\lambda_y$, $k = 1.05$.

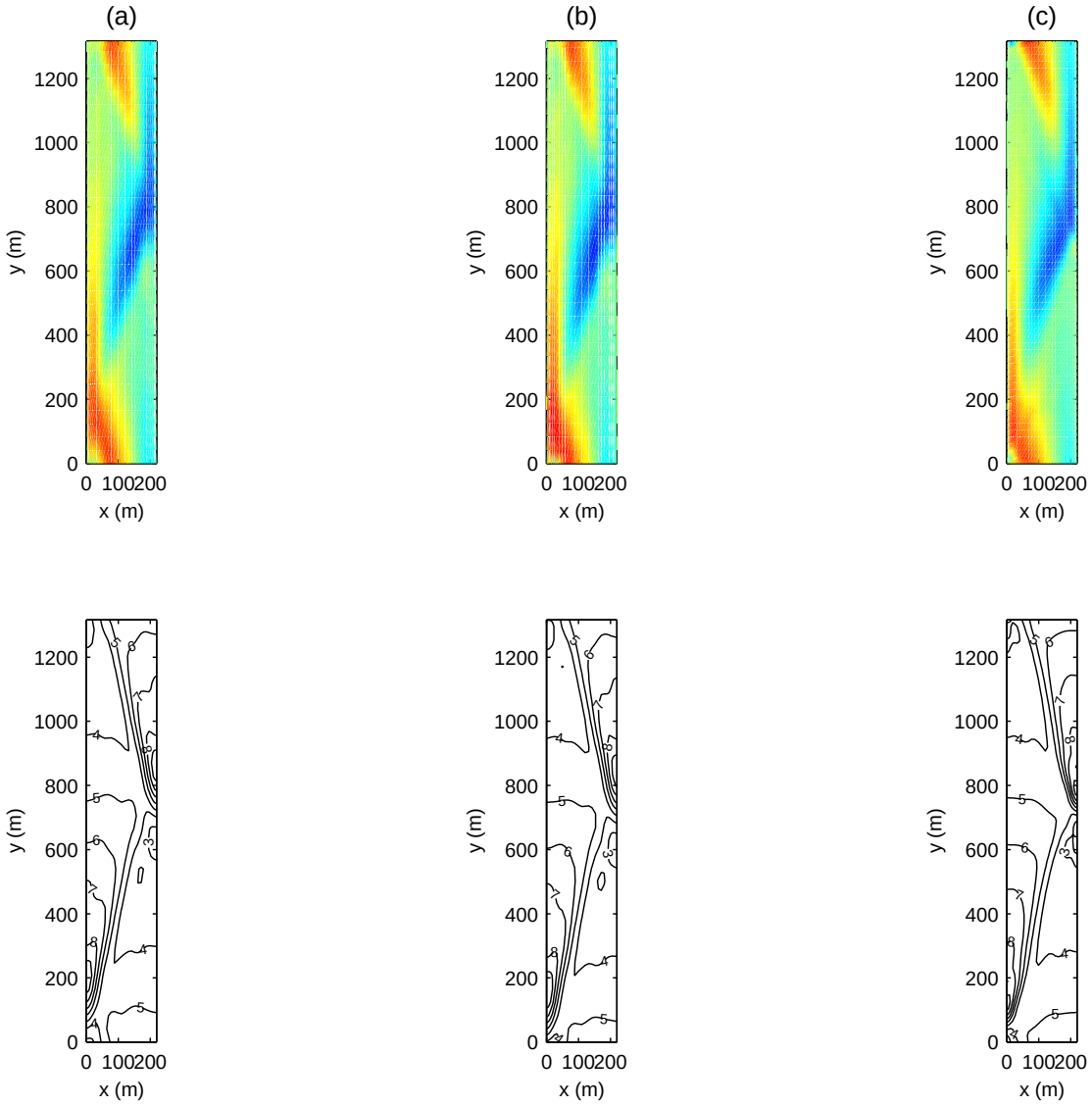

Figure 5.16: Snapshots of the vorticity and topography at $t = 20hrs$ for (a)$L_y = 4\lambda_y$, (b)$L_y = 2\lambda_y$, (c)$L_y = \lambda_y$. Top panel: vorticity, bottom panel: depth contours. Note that only one wavelength is shown for cases (a) and (b).

The same form of initial bottom perturbation is used, this time with $k = 1.35$. The initial flow field is set to zero. Two simulations have been carried out. In the first simulation one perturbation wavelength fits into the channel length, in the second the channel length is doubled so that two perturbation wavelengths fit into the domain.

5.4.1 Results for $L_y = \lambda_y$

For $k = 1.35$ the perturbation wavelength is $\lambda_y = 1000m$, and the length of the channel is also $L_y = 1000m$. According to the dispersion relationship, the bedforms travel faster in this case since a higher wavenumber corresponds to a higher real frequency, ω_r (see Figure 5.4). Their growth rate on the other hand corresponds to a slightly lower value. A comparison of time series is shown in Figure 5.17. Note that the number of fluctuations is almost doubled and that the growth is indeed lower compared to the previous time series.

The dispersion relationship gives nondimensional frequencies of $\omega_r = 2.2897$ and $\omega_i = 0.358$. Using the time series of h, an average nondimensional frequency of $\omega'_{av} = 2.29$ is obtained. The crude propagation speed obtained using this frequency and the perturbation wavenumber is around $C_{bed} = 0.0368m/s$. The propagation speed obtained from the dispersion relation is $C'_{bed} = 0.0339m/s$. The propagation speeds obtained by lag-correlation range from values as low as $0.009m/s$ to $0.0353m/s$. For this case speed values are more fluctuating than the previous results.

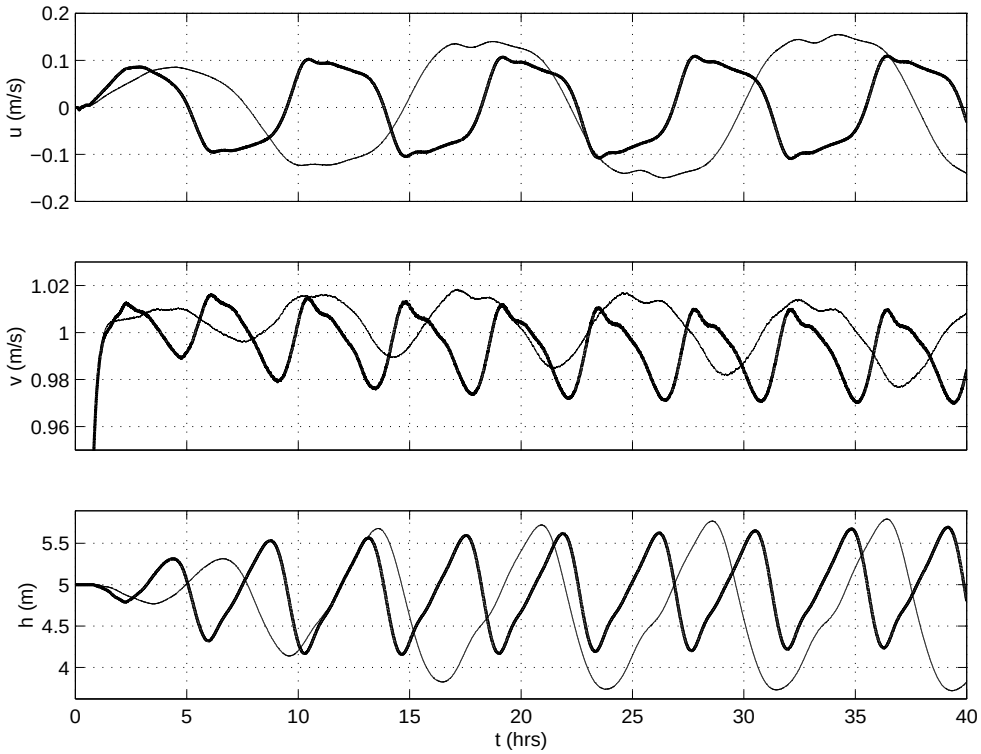

Figure 5.17: Time series of u, v and h at $(x, y) = (110m, 0.5L_y)$ for $L_y = \lambda_y$. (——)$k = 1.35$, (——)$k = 1.05$

The bed evolves into an alternate bar pattern once again. This time the bedforms are more organized and no pairing or separation of contours occurs. The previous fluctuations around the wave front do not form this time, probably due to a less steep wave front slope. The maximum depth contour is $7.28m$ (lowest point) and the minumum value is $3.77m$ (highest point). Snapshots of the simulated bed evolution are shown in Figure 5.18. It is evident that the bar front is shorter.

The flow structure is also less meandering in this case. This can be seen in the vorticity plots (Figure 5.19). The maximum magnitude of vorticity is approximately $8 \times 10^{-4}\ s^{-1}$ in this case, whereas it was around $2.5 \times 10^{-3}\ s^{-1}$ in the previous simulations. The flow field starts out with a more significant meandering pattern and looses some of its magnitude in the later stages. Note how the intensities of the red and blue colored areas at 6 hours are stronger compared to the ones at 13 and 40 hours. For the previous simulations the opposite occured, the flow field attained a more meandering nature (see Figures 5.10 and 5.13). Associated with a lower growth rate and a higher propagation speed, the evolution of the bed and the flow field reaches a smoother configuration in the present case.

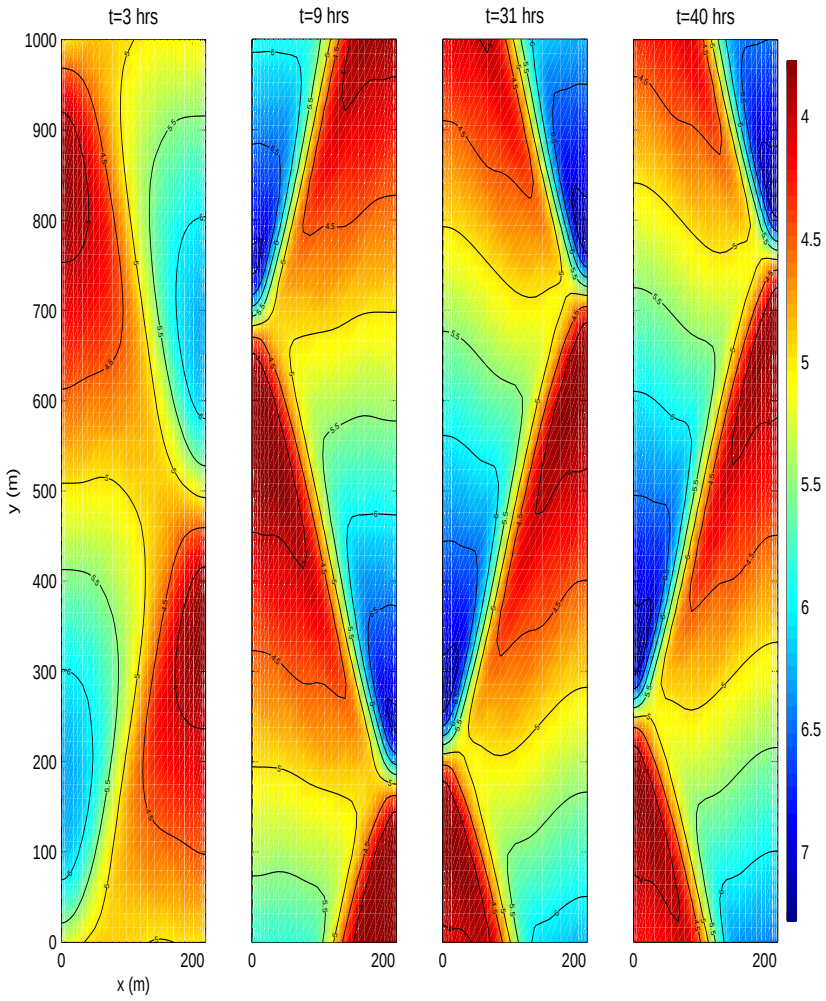

Figure 5.18: Simulated bed evolution for $L_y = \lambda_y$, $k = 1.35$.

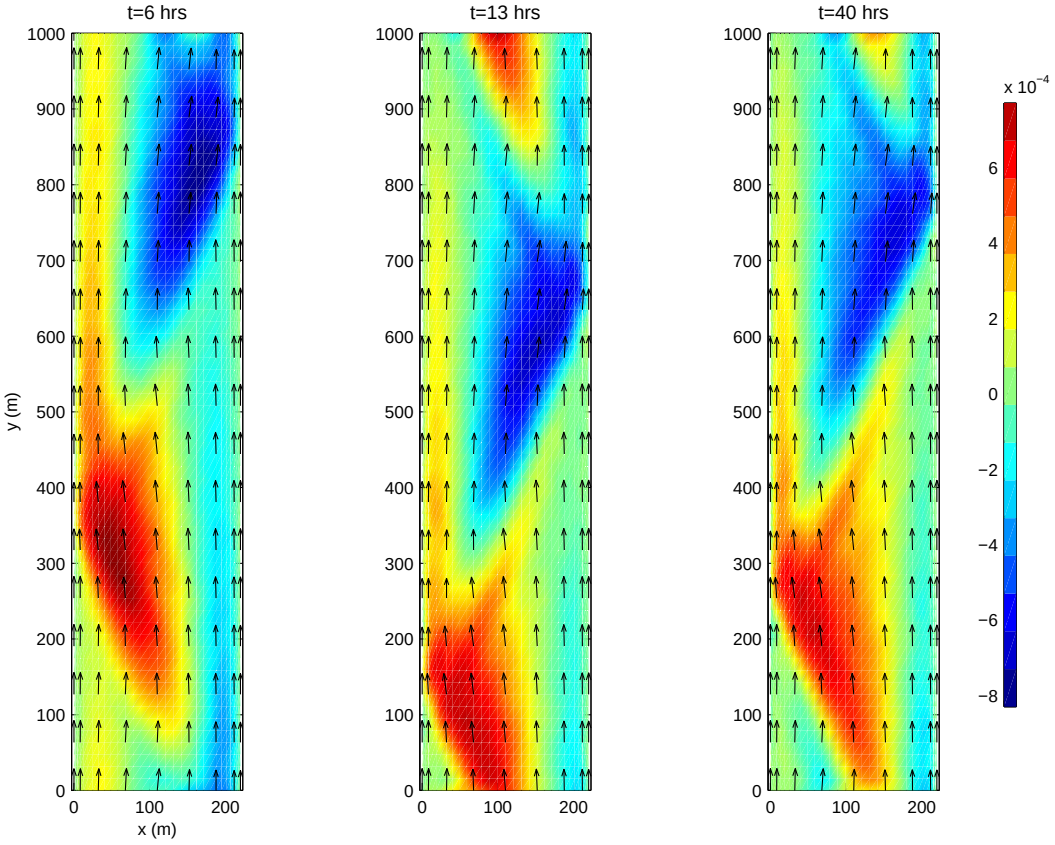

Figure 5.19: Snapshots of the velocity field on top of the vorticity for $L_y = \lambda_y$, $k = 1.35$.

5.4.2 Results for $L_y = 2\lambda_y$

Similar to the previous simulations, here also a channel length twice as long as the unstable wavelength is used in order to investigate the effect on the bed evolution. The channel length becomes $2000m$. The other parameters are again kept the same.

The time series of u, v and h are shown in Figure 5.20. There is a lag which increases in time between the previous and present case, but the general shape of the fluctuations is almost the same. The final bar amplitude is slightly larger overall. An important point to note is that the growth becomes non-periodic. Looking at the time series of h, a lower peak passes by, around 27 hours. After that the bedforms start to grow again. This does not happen in the previous cases. Schielen *et al.* (1993) identified quasi-periodic behaviour of the bed in time and space for long-term simulations. In this behaviour a non-periodic motion can be observed in which different independent fundemantal frequencies of the bedforms exist. Although not as obvious as in the case of Schielen *et al.*, the present non-periodic behaviour of h resembles a similar feature in time. This kind of behaviour is easier to detect for smaller time and spatial scales as noted by Schielen *et al.*. For a longer simulation this behaviour could become more evident.

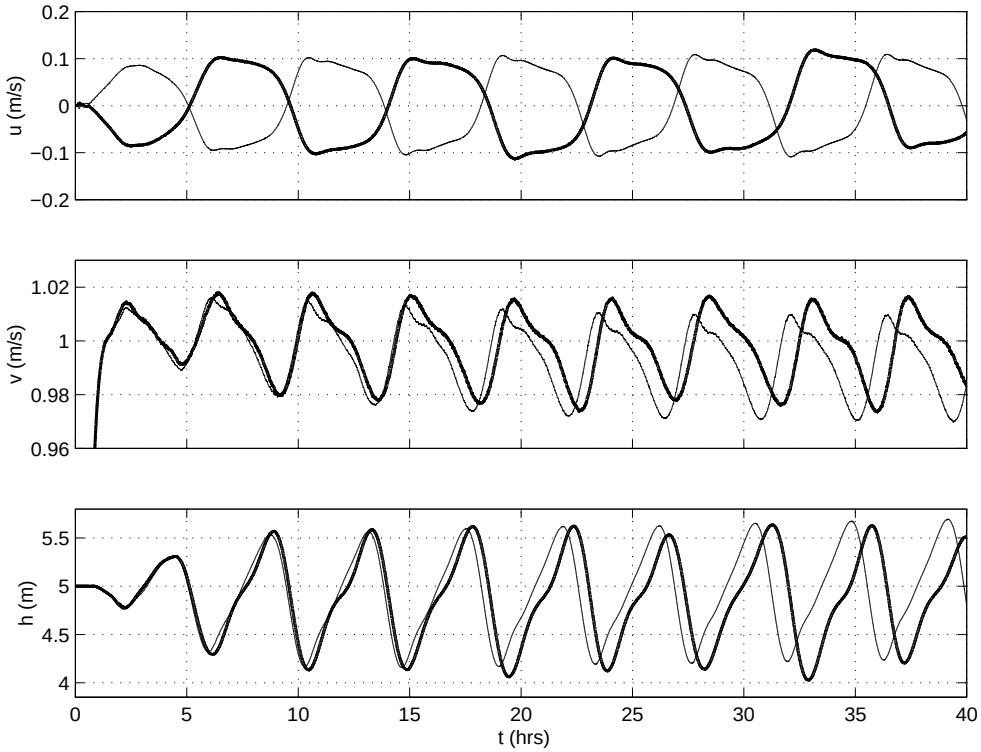

Figure 5.20: Time series of u, v and h at $(x, y) = (110m, 0.5L_y)$ for $k = 1.35$. (——)$L_y = 2\lambda_y$, (——)$L_y = \lambda_y$

The average nondimensional frequency is $\omega'_{av} = 2.15$, and the bedform propagation speed is $C_{bed} = 0.0318m/s$. The propagation speed from the dispersion relationship is $C'_{bed} = 0.0339m/s$. Using lag-correlation the speed ranges between $0.0176m/s$ and $0.0353m/s$.

The simulated bed evolution is shown in Figure 5.21. The highest point within the channel after 40 hours is $2.7424m$ and the lowest is $7.6709m$. Compared to the previous case it is obvious that more erosion and deposition occured for this case. Details of the resulting topography can be seen in the next figure.

The meandering flow structure for this case is more pronounced. The maximum vorticity reaches a value of $1.1 \times 10^{-3}\ s^{-1}$ in 40 hours, whereas in the previous case the maximum value is significantly smaller and the vorticity is also decreasing in time. A comparison is given in Figure 5.22, where snapshots of the flow field on top of the vorticity and the depth contours are included. Note the difference in the vorticities. The meandering nature of the flow is obviously more pronounced for this case, which is shown in Figure 5.22(b). The resulting depth contours are also different, and the contours are more fluctuating in this case. It is also evident that the propagation of the instabilities is different in each case.

It is clear from the time series, the flow field and the resulting topography that as the channel length increases the propagation of the instabilities increases too. The opposite occurs when the most unstable wavenumber is used in the first three simulations. Comparing the last two simulations with k_{max}, the propagation speed decreases as the channel length increases. The initial condition on the flow field and the bottom perturbation are also important, but from the simulations at hand, the growth rate and propagation speed of the instabilities are obviously effected and they change in time, although the overall alternate bar pattern is preserved.

5.5 Simulation for a Smaller Wavenumber, $k < k_{max}$

Similar simulations have been obtained using a smaller wavenumber of $k = 0.67$ for the initial bed perturbation (see Figure 5.4). This corresponds to a wavelength of $\lambda_y = 2000m$. For this case a channel length of $L_y = 2000m$ has been used, so one perturbation wavelength fits into the domain. The rest of the parameters are the same.

The nondimensional frequencies from the dispersion relationship are $\omega_r = 0.5947$ and $\omega_i = 0.339$. From the real frequency a dimensional propagation speed of $C'_{bed} = 0.0177m/s$ can be obtained. The approximate average period of $T_{av} \approx 31hrs$ which corresponds to a nondimensional frequency of $\omega'_{av} = 0.623$ is computed from the time series of h. Using this frequency and the perturbation wavenumber, the propagation speed of the bedforms is around $C_{bed} = 0.0186m/s$. Lag-correlation gives speeds from $0.009m/s$ to $0.0186m/s$.

The comparison of the time series of h for this case and the previous cases is shown in Figure 5.23. According to the linear dispersion relationship, a smaller wavenumber corresponds to a smaller propagation speed. This is evident in the time series plot, where the least amount of fluctuations is found for $k = 0.67$. Although the general trend of growth is present in each case, the form of the fluctuations for $k = 0.67$ is different than the others. A similar form is present for the time series of u and v.

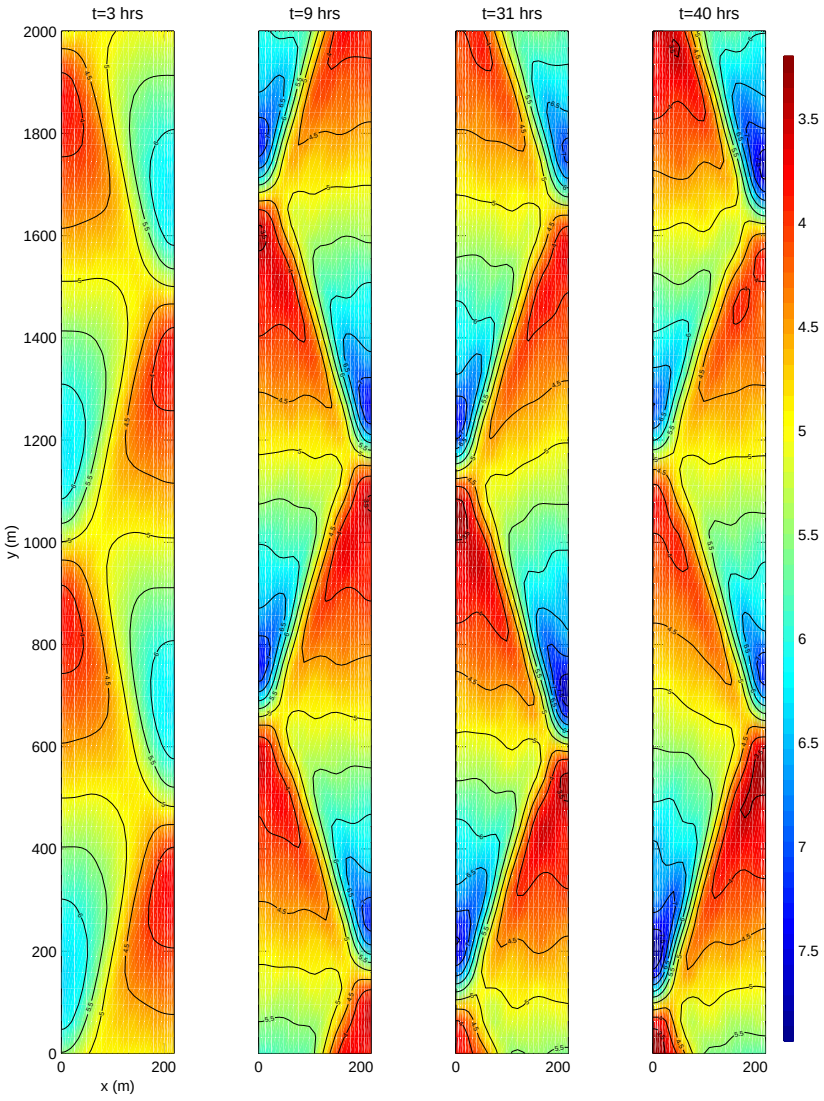

Figure 5.21: Simulated bed evolution for $L_y = 2\lambda_y$, $k = 1.35$.

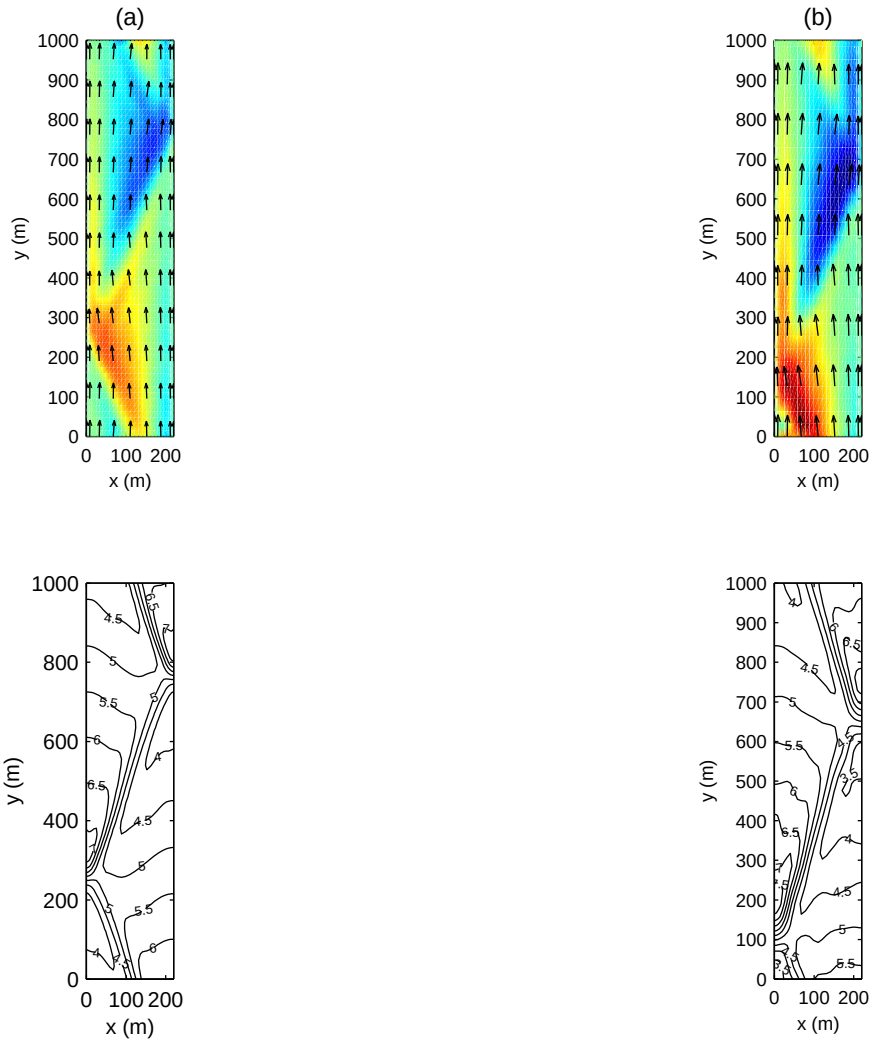

Figure 5.22: Snapshots of the flow field, corrsponding vorticity and topography at $t = 40hrs$ for $k = 1.35$. (a)$L_y = \lambda_y$, (b)$L_y = 2\lambda_y$. Top panel: flow field and vorticity, bottom panel: depth contours.

The bed evolution in general is again in the same form, although at later stages the flactuating wave fronts are more pronounced (Figure 5.24). The alternating bar pattern evolves within the first 10 hours, but at points around the wave front the shape starts changing at 16 hours. The fluctuations are very strong compared to the other cases. This becomes especially evident after 30 hours, and at 40 hours a spit-like feature has developed along the wave front (Note the red areas in the pseudocolor plots). Looking at the three-dimensional picture of the topography shown in Figure 5.25, these features can be seen more clearly. At an earlier stage the sand waves attain a steeper front slope as before, but at 40 hours the fluctuations around the wave front alter the smooth shape of the waves. Note especially the second smaller wave that has formed right in front of the larger wave. An additional 8 hour simulation shows that the overall growth of the sand waves continues. The smaller wave shows a fluctuating nature; as it evolves it does not exceed its height developed

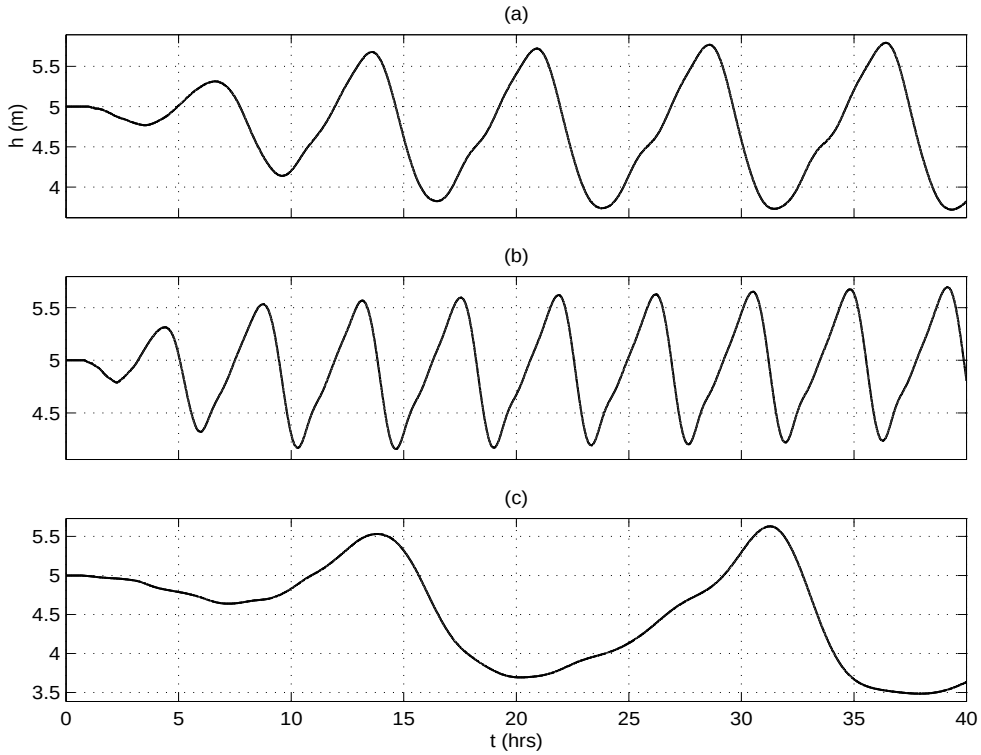

Figure 5.23: Time series of h at $(x, y) = (110m, 0.5L_y)$ for (a)$k = 1.05$, (b)$k = 1.35$, (c)$k = 0.67$.

at 40 hours and it does not fall below a certain height. Additional fluctuations over the higher sections at the back of the larger wave start forming at 41 hours, but they smooth out at 48 hours. Since no significant changes occur, the bed evolution beyond 40 hours has not been shown.

The evolution of the flow field shown in Figure 5.26 is very similar to the flow fields of the other cases; a meandering pattern is present. The magnitude of the vorticity shows a larger growth over time than before. Note how the vorticity at 6 hours compared to the one at 40 hours is extremely weak. The largest vorticity values are confined to a very thin section of the channel, very close to the walls. Those sections correspond to the points where separation of contours emerge and the spit-like wave front occurs. The maximum vorticity is 0.0287 s^{-1} which is considerably higher than the values from the previous simulations.

5.6 Effects of Different Parameters

The equations governing the evolution of the combined flow-bed system incorporate certain parameters which can be considered as 'fudge factors'. Most of them are only determinable through laboratory measurements and for some cases only through observations. In the present problem the friction factor c_f and the velocity power b in the sediment transport equation are considered. Other factors that could affect the bed evolution are the width-to-

depth ratio R of the channel, the parameter γ' or the coefficient ν in the transport equation.

From the stability analysis point of view, it is obvious that the growth rate and propagation of the bedforms will be affected by changing these parameters. The morphological time scale for example, includes ν, b, the channel width y_* and the channel depth h_*. The morphological time scale directly governs the magnitudes of the growth rate and propagation speed. Colombini *et al.* (1987) and Schielen *et al.* (1993) obtained differential equations which govern the bedform amplitudes (The Landau and Ginzburg-Landau equation). These equations include c_f, ν, b and γ'; so depending on these parameters the resulting beforms could change.

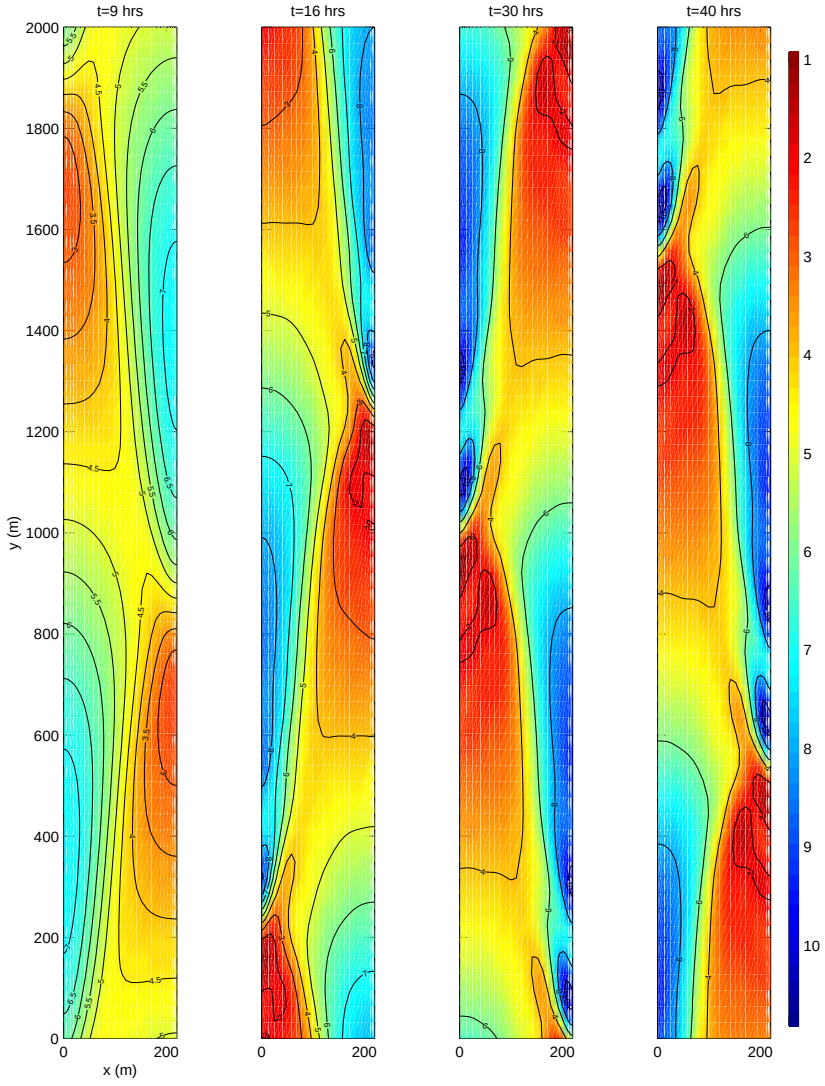

Figure 5.24: Simulated bed evolution for $L_y = \lambda_y$, $k = 0.67$.

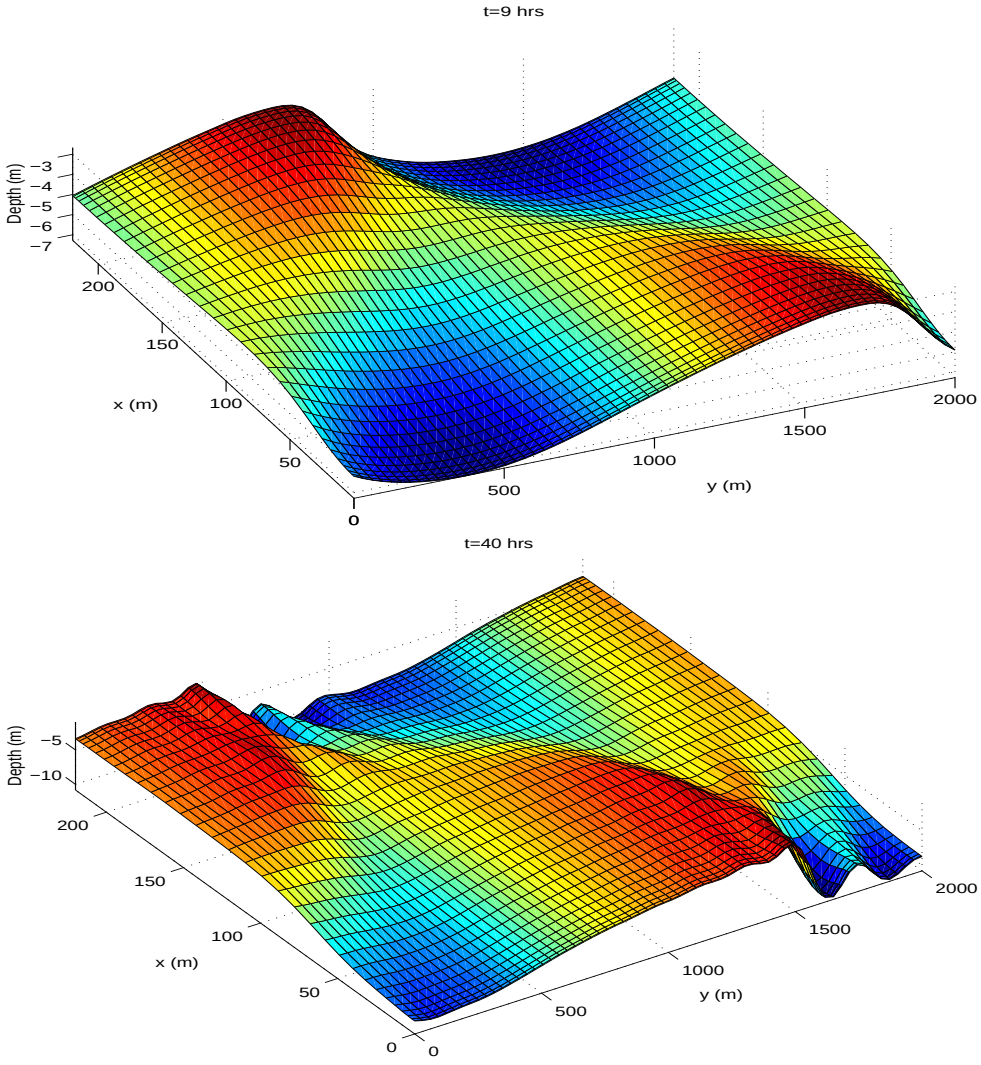

Figure 5.25: Snapshots of the bed evolution in 3D for $L_y = \lambda_y$, $k = 0.67$.

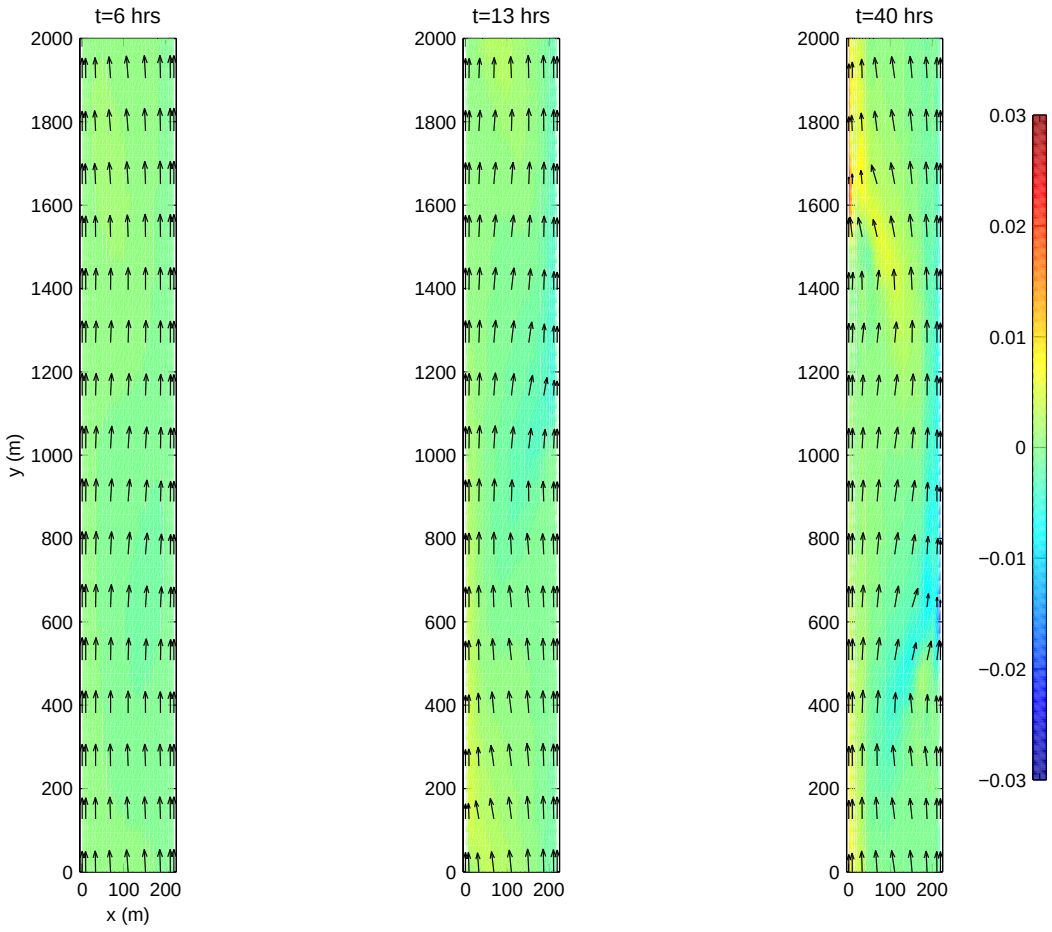

Figure 5.26: Snapshots of the flow field and corrsponding vorticity for $L_y = \lambda_y$, $k = 0.67$.

Looking at the transport equation (4.14), the parameter ν changes only the magnitude of the resulting transport rate. Tests with different ν values confirm this fact, and the resulting bedforms were not affected significantly. Given the same initial conditions, its effect on the bed evolution is in the form of either faster or slower growth/decay depending on the instability and the morphological time scale. The parameter b governs the relative magnitude of the transport rate since it is the power of the velocity. There exists a critical velocity value which produces the same transport rate regardless of what b is. For a simplified version of the transport equation $q = u^b$, that velocity value is 1. For larger b values a velocity value smaller than the critical one corresponds to lower transport rates and a velocity larger than the critical corresponds to higher transport rates. This affects the morphological time scale, too. Considering also that the flow may develop complicated patterns depending on the friction factor and other interaction machanisms in the system which were neglected in the stability analysis, it may be important to investigate the actual effects of changing these parameters.

5.6.1 Different Values of the Friction Factor c_f

Simulations have been run for two different c_f values, one smaller and one larger than $c_f = 0.003$. The most unstable wavenumber for the bed perturbation obtained in section 5.3, the same channel geometry and sediment transport parameters are retained. The channel length is chosen such that one perturbation wavelength fits into the domain.

First a value of $c_f = 0.001$ corresponding to an along-channel basic flow velocity of $V = 1.7312 m/s$ with a channel slope of $i_o = 6.11 \times 10^{-5}$ has been considered. The dispersion relationship for $k = 1.05$ and $c_f = 0.001$ predicts that the bedforms are stable (Figure 5.27(a)). The time series show that this is true to a certain extend. The bedforms start out with some growth, but reach equilibrium in approximately 5.55 hours (Figure 5.28). It is also obvious that the bedforms propagate a lot faster. The dispersion relationship gives frequency values of $\omega_r = 42.0042$ and $\omega_i = -0.8873$. The dimensional propagation speed can be computed as $C'_{bed} = 21.5386 m/s$ which is extremely large. The numerical results do not show such a high propagation speed. The resulting bar pattern is the same as before, therefore the bed evolution results are not shown here. The amount of erosion and deposition is smaller than all the previous results. The overall structure of the bar pattern is slightly smoother and the flow field, too. The maximum value of vorticity for this case is 8.18×10^{-4} s^{-1} which is again smaller than before. This means that the meanders are not as pronounced as before.

In the second run a friction factor of $c_f = 0.03$ has been used. This corresponds to a basic along-channel velocity of $V = 0.3161 m/s$. Although the dispersion relation predicts that growth happens for $k = 1.05$ (Figure 5.27(b)), the numerical results do not show any growth or propagation.

Another case where $c_f = 0.03$ and the corresponding most unstable wavenumber has been used to determine the bed perturbations shows that the bedforms can evolve into somewhat different shapes. The nondimensional most unstable wavenumber obtained from the linear stability analysis is $k = 3.1$ and the frequencies are $\omega_r = 8.477$ and $\omega_i = 3.095$. The basic along-channel flow now corresponds to $V = 1 m/s$, and the channel length is

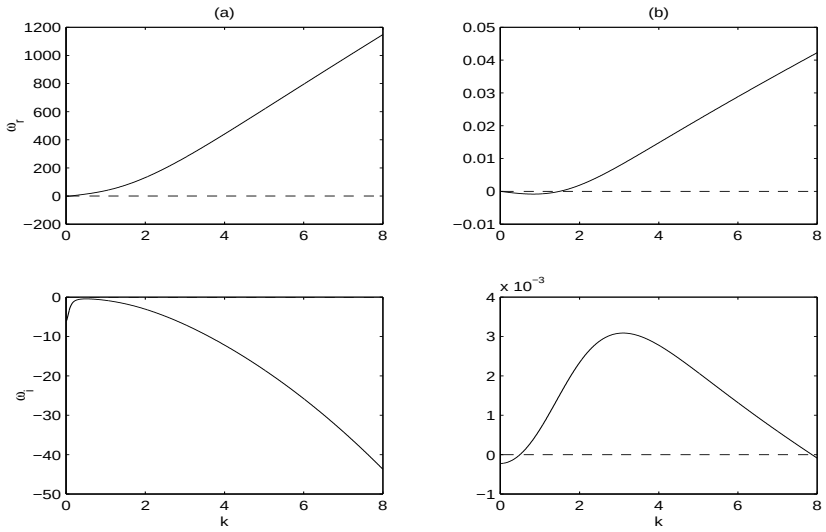

Figure 5.27: Dispersion curves for (a)$c_f = 0.001$, (b)$c_f = 0.03$.

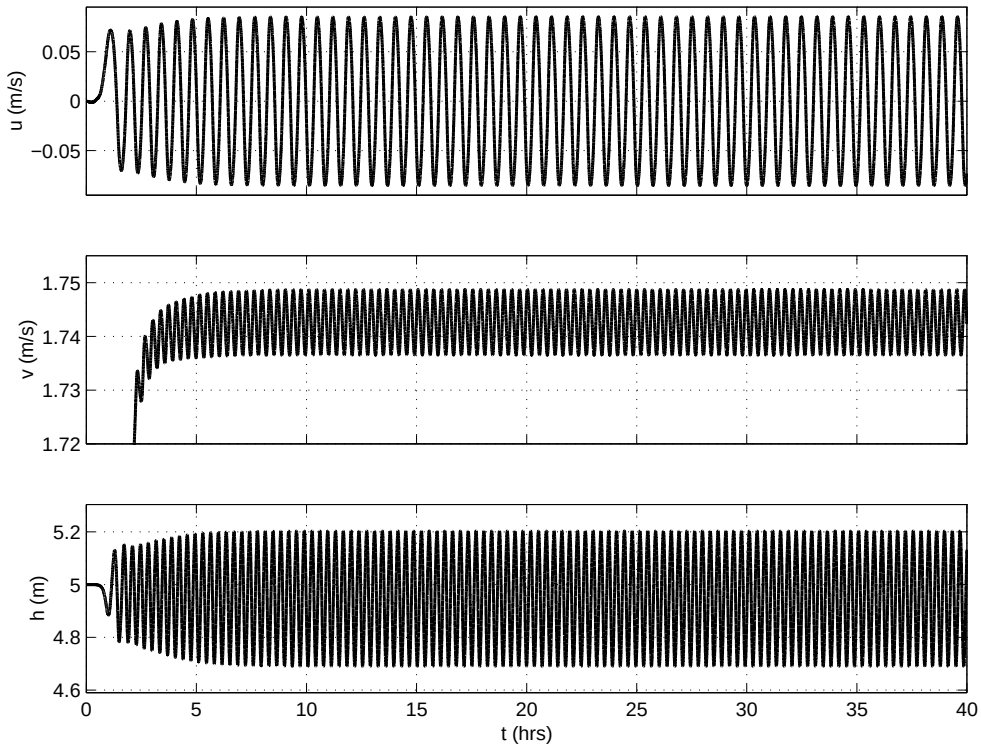

Figure 5.28: Time series of h at $(x, y) = (110m, 0.5L_y)$ for $k = 1.05$ and $c_f = 0.001$.

approximately $446m$. The general pattern of alternate bars is preserved but the fluctuating wave fronts cause significant contour separations, which can be seen as deep scour holes in Figure 5.29. The bar front is not as significant as in the other simulations. Although the most unstable wavenumber is used to determine the bed perturbation, growth only happens

to a certain extend. The bedforms seem to have reached equilibrium by 10 hours. The bedforms start out with some growth which is followed by some decay. This is evident from the time series (Figure 5.30) where also the general form of fluctuations is different from the previous cases.

The flow field directly responds to the bed change as before and no significant difference was observed. The meandering nature of the flow is much stronger since higher values of vorticity are attained. The maximum is around $0.064s^{-1}$ at 5 hours, but than drops to $0.044s^{-1}$ by the end of 10 hours.

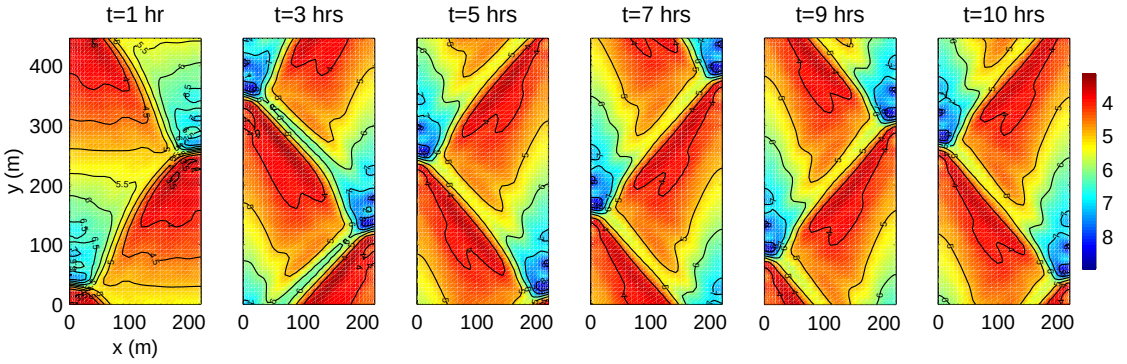

Figure 5.29: Snapshots of the bed evolution for $L_y = \lambda_y$, $k = 3.1$ and $c_f = 0.03$.

5.6.2 Different Values of b

A parameter governing the sediment transport rate is the power b of the velocity in the transport equation. In order to investigate its effect we carried out two simulations with two different values of b. For $b = 2$ and $k = 1.05$ the stability analysis predicts decay of bed features. This is also confirmed by the numerical results. The bed change at the mid-section of the channel starts out with a certain amount of decay the first 4.44 hours which turns into growth until equlibrium is reached at approximately 13 hours (Figure 5.31(b)). After this point the bedforms are stationary, they neither propagate nor show growth. Looking at the whole channel, the bedforms experience an overall decay while reaching equilibrium. The nondimensional frequencies are $\omega_r = 0.7381$ and $\omega_i = -0.11931$. The resulting bed pattern is also not the same as before, for this case the meanders are not visually detectable. The steep wave fronts are still present, but the shape of the bar front across the channel is different; it does not resemble the idealized alternate bar formation in alluvial channels. The results are shown in Figure 5.32, note that the bedforms do not show any change or propagation after 14 hours.

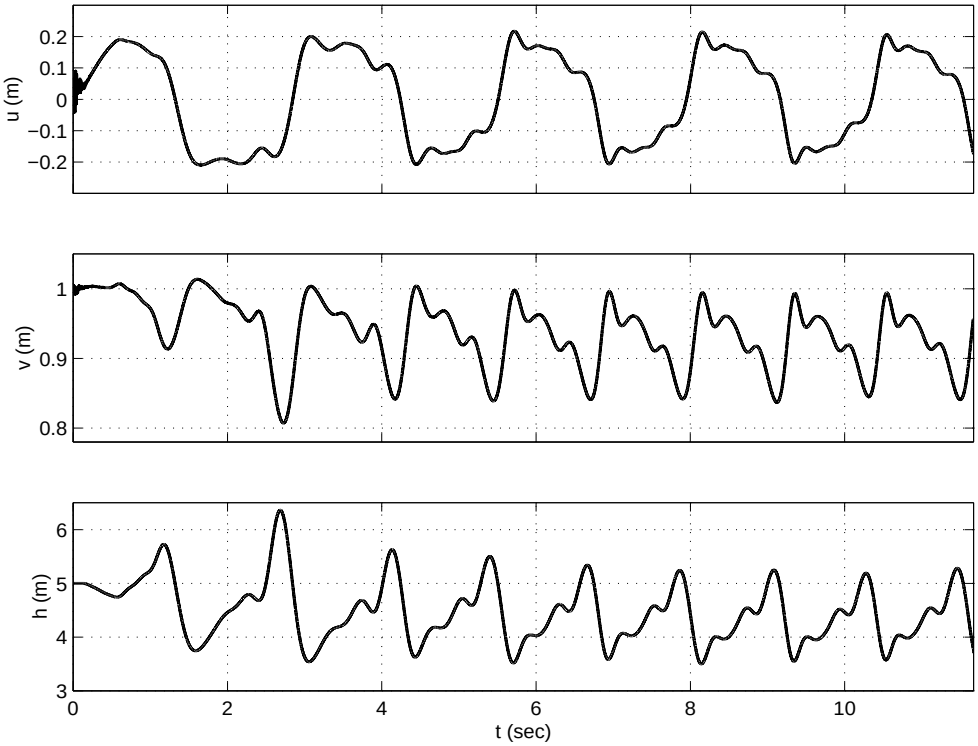

Figure 5.30: Time series of u, v and h at $(x, y) = (110m, 0.5L_y)$ for $k = 3.1$ and $c_f = 0.03$.

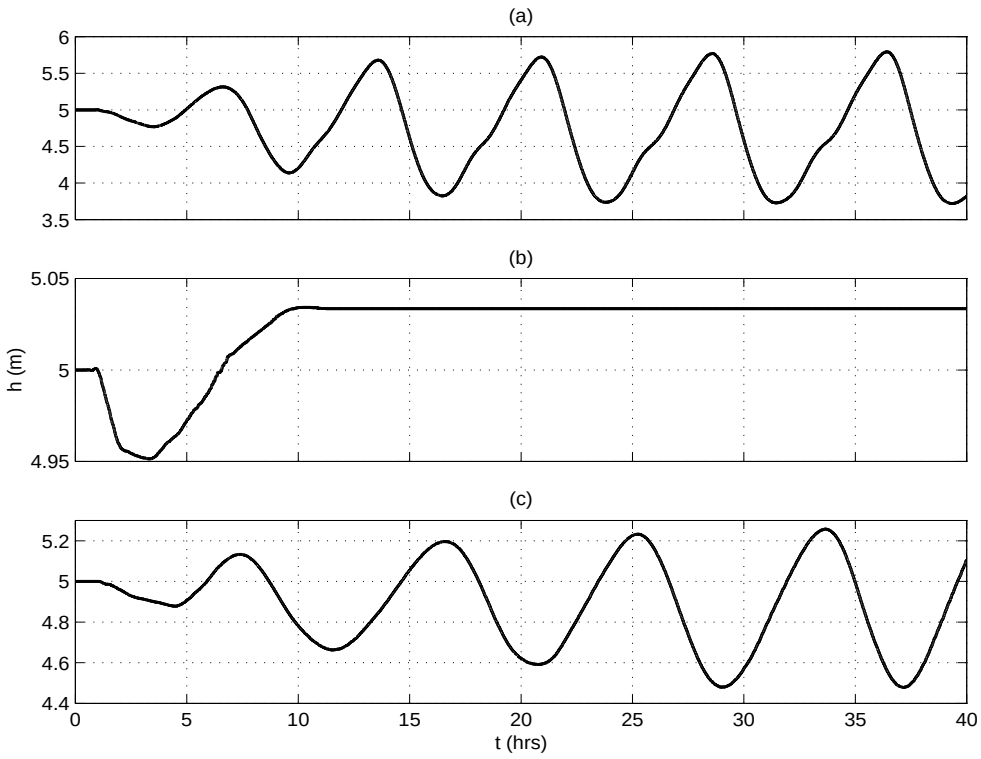

Figure 5.31: Time series of h at $(x, y) = (110m, 0.5L_y)$ for (a)$b = 6$, (b)$b = 2$, (c)$b = 4$.

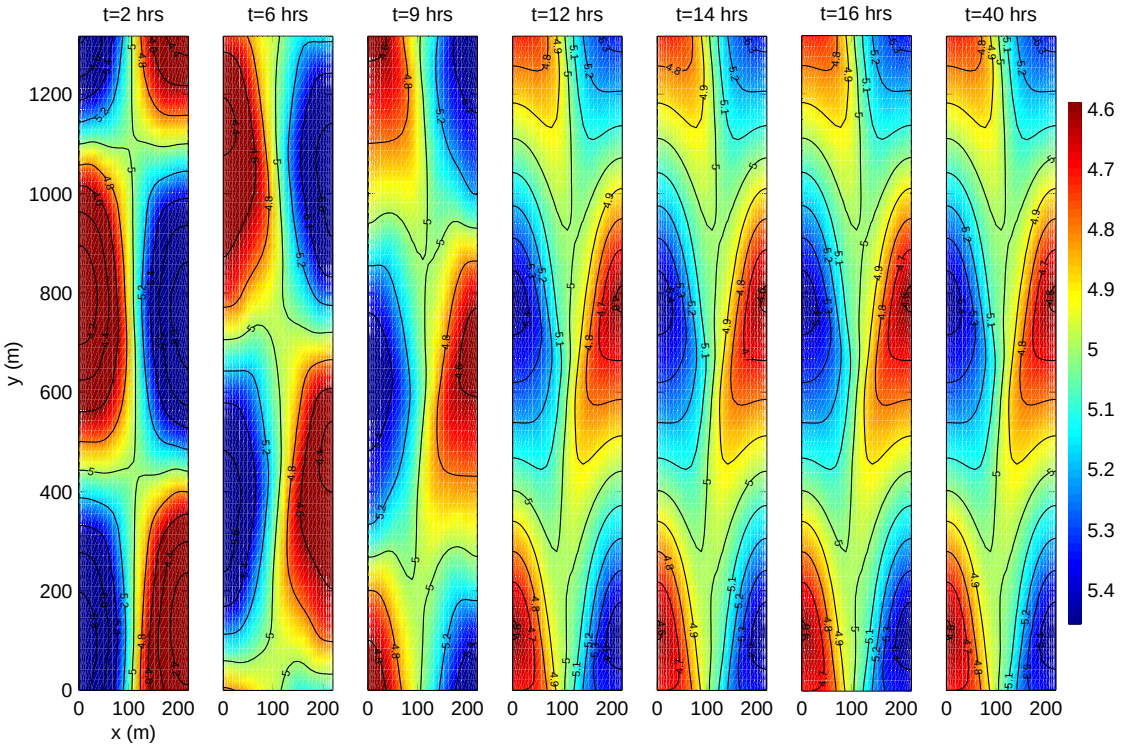

Figure 5.32: Snapshots of the bed evolution for $k = 1.05$ and $b = 2$.

The deepest point in the domain is $5.4576m$ and the lowest is $4.5893m$ after 40 hours. The amount of erosion and deposition is obviously lower for this case and the bedforms travel with a much slower speed. The speed obtained from the dispersion relation is $C'_{bed} = 0.0141m/s$.

The corresponding flow field and vorticity shown in Figure 5.33 obviously do not show any signs of meandering. Although hard to notice, a slight convergence of velocity vectors over the orange colored sections and a divergence over the deep blue colored sections are present. These are divided in two portions towards the middle of the channel. This flow field structure explains the sharp and peaky forms of the $5m$ contour towards the mid-section, and also why the alternate bar pattern does not form.

For a value of $b = 4$ the most unstable wavenumber is $k = 4.36 \times 10^{-3}$. The nondimensional frequencies are $\omega_r = 1.192$ and $\omega_i = 0.1224$. The time series of h for this case is similar to the case where $b = 6$ (Figure 5.31(a)-(c)). The resulting alternate bar pattern is smoother and the overall sediment transport amount is smaller accompanied with a slower propagation speed of the sand waves. Using the stability analysis, the propagation speed of the forms is around $C'_{bed} = 0.0231m/s$, and from the frequency obtained from the time series and the wavenumber $C_{bed} = 0.0245m/s$. The speeds obtained from lag-correlation range from $0.0062m/s$ to $0.0310m/s$. Since the resulting bar pattern and flow field are essentially very similar to the previous results, they are not shown here.

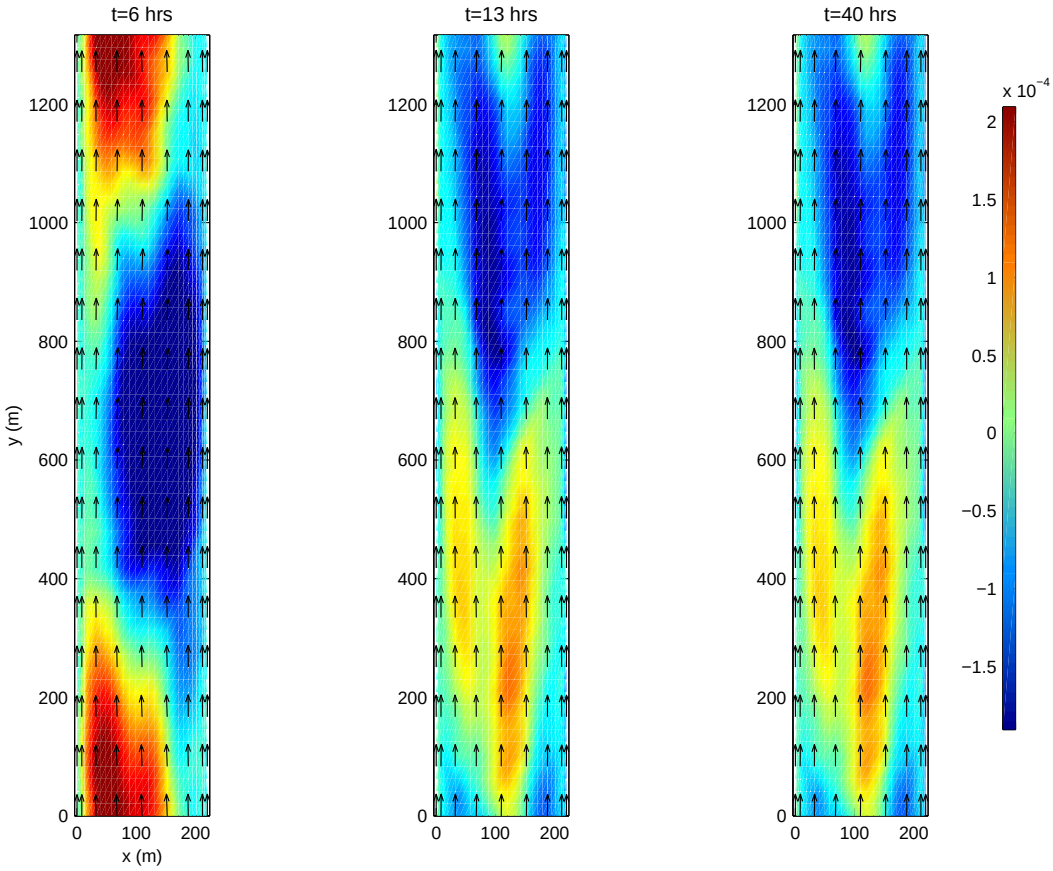

Figure 5.33: Snapshots of the flow field and vorticity for $k = 1.05$ and $b = 2$.

5.7 Effects of Different Initial Bed Perturbations

In order to investigate the effect of initial conditions we obtained results with two different initial bed perturbations. The channel is long enough to include two perturbation wavelengths corresponding to $k = 1.05$. The first bed perturbation includes its lower harmonics as well, and the second perturbation includes one wavelength plus half a wavelength

$$z_b(x, y, t = 0) = z_c cos(d_{c1}x)[cos(d_{c2}y) + cos(Kd_{c2}y)] \tag{5.2}$$

where $K = 2$ for the first perturbation and $K = 1/2$ for the second one. The rest of the parameters are the same for the case with the first perturbation. For the second one, in order to be able to simulate the bed evolution for a considerably long period, a lower perturbation amplitude of $z_c/10$, and a lower transport coefficient of $\nu = 0.07$ have been used.

Results for the first case are shown in Figures 5.34 and 5.35. The bed starts to show changes after the first 40 minutes which is more significant at 60 minutes. The $5m$ contour has separated to form the spit-like part reaching to the $5.5m$ contour. Two significant scour holes are formed at 190 minutes (note the $6m$ and $7m$ depth contours, or the deep blue colored areas), and the $4.5m$ contour on one side of the channel is pairing with the one on the other side, which is more evident at 290 minutes. At 250 and 290 minutes the higher

harmonics of the perturbation have almost diminished. Obviously, the second harmonics of the perturbation are smoothed out, and the contours are rearranging such that the bed pattern reaches the same alternate bar configuration. From 360 to 390 minutes, the bed configuration becomes more organized, especially by the separation and paring of the $5m$ contours. The pattern is well organized by 500 minutes, no significant contour pairing and separation occurs beyond this time. In 10 hours the bed configuration has again developed into an alternate bar pattern.

Compared to the results in section 5.3.2 where higher harmonics are not included, the resulting pattern in this case is very similar. It is in general smoother and the amount of erosion and deposition in 10 hours is about the same for both simulations.

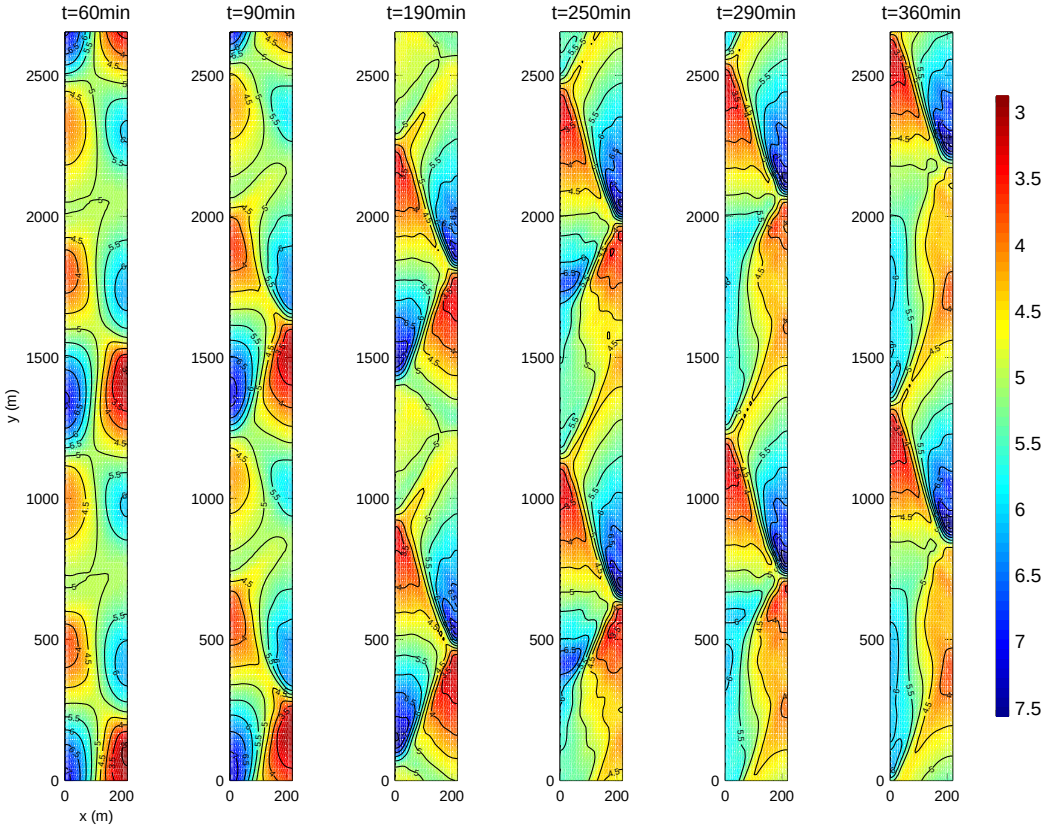

Figure 5.34: Snapshots of the bed evolution for $k = 1.05$ with $K = 2$ in the bed perturbation.

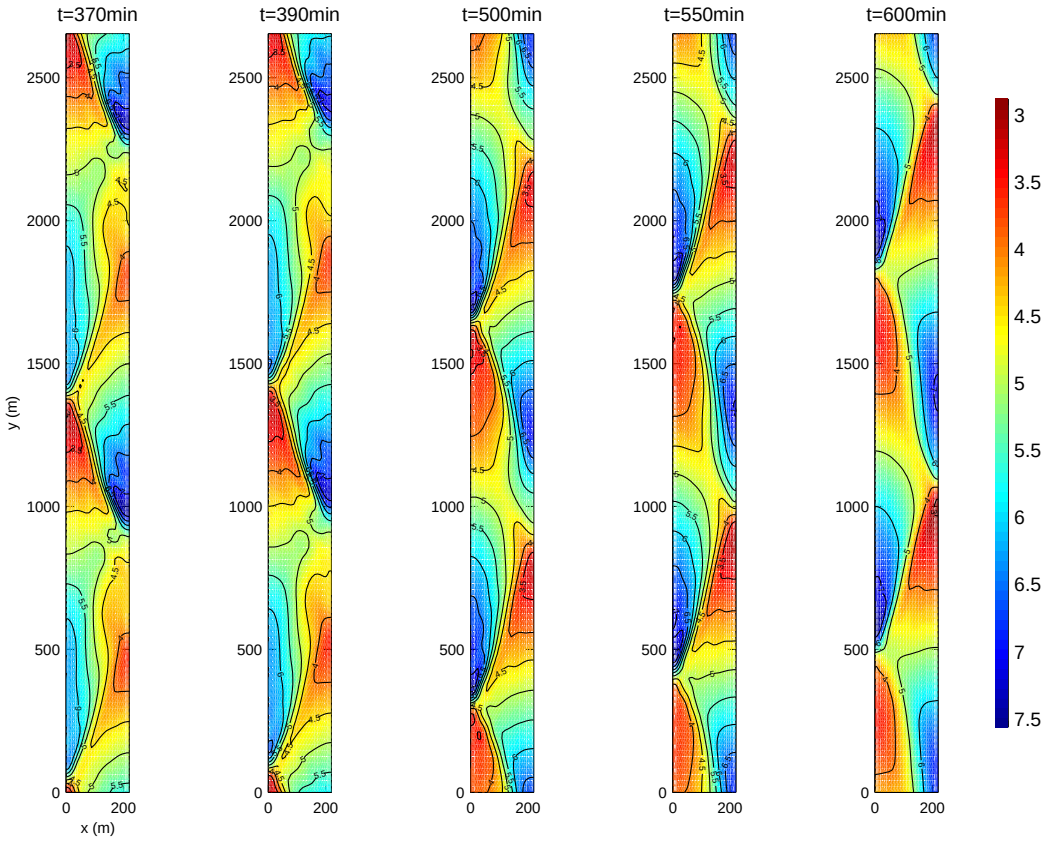

Figure 5.35: Snapshots of the bed evolution for $k = 1.05$ with $K = 2$ in the bed perturbation (continued).

The flow field once again adjusts itself instantaneously to the bed evolution and the general form of meandering flow is attained at 10 hours. Overall the flow field does not show an evolution significantly different than the previous results. The magnitude of the vorticity reaches a maximum of 0.0013 s^{-1}, which is smaller than the maximum vorticity at 10 hours in section 5.3.2. This matches the bed configuration where less meandering and a less energetic flow cause a more smoother bed pattern.

For the second case the initial perturbation evolves into a pattern similar to an alternate bar form, but now with a bigger sand wave followed by a smaller one (Figure 5.36). This configuration is preseved through the whole simulation time which is 2 days. The steep wave fronts and the fluctuations around them form once again. At 36 hours the $3m$ contour separates followed by the $4m$ contour at 40 hours. The smaller wave significantly deformes as it propagates behind the bigger one. The bigger sand wave is very similar to the sand waves forming in the previous examples.

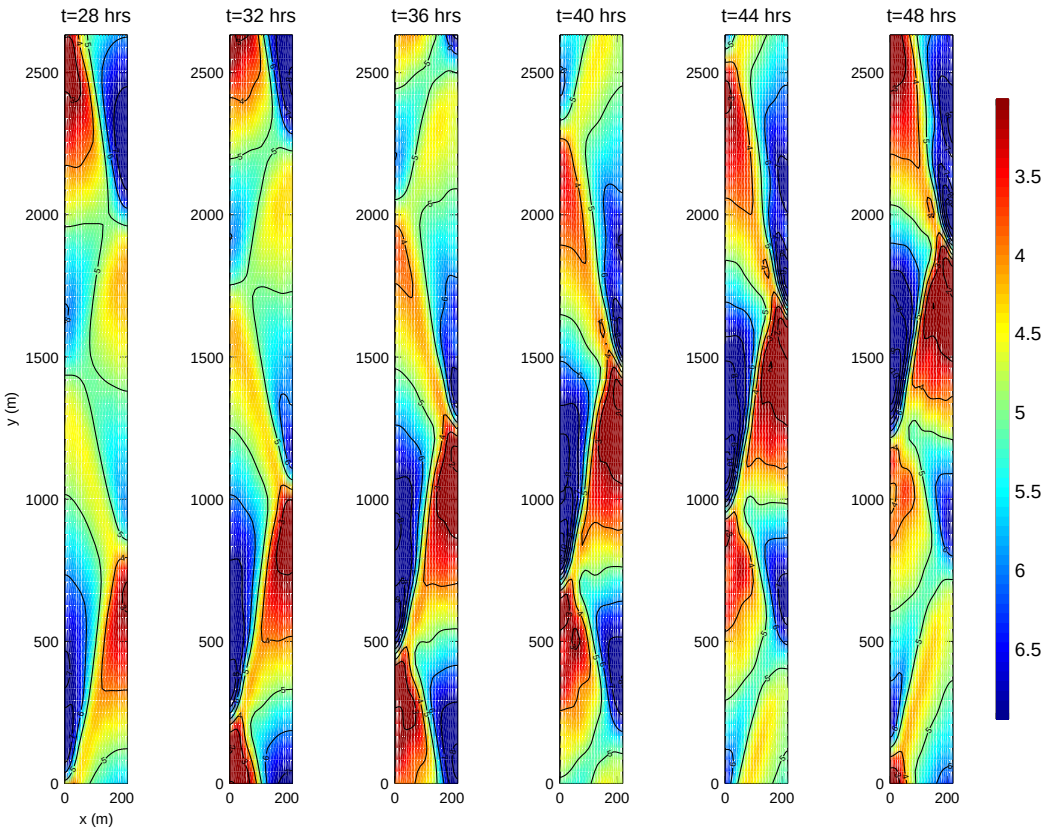

Figure 5.36: Snapshots of the bed evolution for $k = 1.05$ with $K = 1/2$ in the bed perturbation.

5.8 Alternate Bars in a Flume Experiment

Uchijima (1990) performed a series of experiments in a laboratory flume to study the deformation of alternate bars. A straight flume with $0.3m$ width, $0.4m$ height and $14m$ length is used. The experiment consists of three sets. First, two patterns of single-row alternate bars, stable and developing ones are formed for the initial bed. In the second set, tests on the deformation of the bars at low stage are conducted. These are continued until the local scour stabilized. In the third set the discharge used in the first set is used on the resulting bed from the second set in order to examine the hysterisis effect. We are concerned with the first two sets of the experiment. The discharge used in the first set is $Q = 2.12\ l/s$ and the flume slope is $i_o = 1/70$.

There were two major difficulties involved in the simulations. The first one is choosing the correct friction factor c_f and the transport coefficient ν. The second problem is computing an appropriate flow depth which is not given in the data. Since the discharge, the channel width and slope are known we picked a friction factor and tried to calculate a flow depth. Considering the basic flow state in a rectangular channel, i.e. $i_o g = c_f U^2/d$, a very large friction factor of $c_f = 0.09$ gives a flow depth of $d = 3.17mm$. Looking at the experimental results the flow depth should be larger than the resulting bedforms (Figure 5.37).

In the results only the eroded sections are shown. Considering an alternate bar pattern, the maximum height of accretion should match the maximum scour depth. Since the deepest point measures $-15mm$, our choice of $31.7mm$ flow depth seems to be appropriate. Note that the bedforms are measured taking the unperturbed bed level as reference where the 0 contour corresponds to the flume bed. Unfortunately due to the extremely small flow depths and small bed features involved, the numerical model was not able to compute results in a practically feasible simulation time and again due to the same reasons numerical stability problems occured (i.e. violation of the Courant condition). Therefore in order to still use this data and investigate the same patterns we used one of the previous simulations.

The simulations carried out for different channel lengths showed that the resulting bed features do not change significantly, therefore we decided to use the same simulation in section 5.3.2. First, a simulation has been run long enough to obtain the same ratio of maximum scour depth-to-flow depth ratio as in the experiment. With the computed flow depth, this ratio is about 1/2. Starting out with an unperturbed channel depth of $5m$, a close ratio is obtained after 7 hours of simulation, when the maximum scour depth reaches about $2.47m$ (taking the channel bed as reference). Similar alternate bars are obtained. In the second run, the flow has been reduced the same amount as in the experiments. In the experiments, the discharge of 2.12 l/s is reduced to 0.6 l/s. In our simulations the first basic flow velocity of 1 m/s is reduced to 0.283 m/s. This has been achieved by setting the along-channel slope to $i_o = 4.898 \times 10^{-6}$ and keeping the rest of the parameters the same. The channel bed obtained from the first 7 hours run is used as input for the second run with reduced flow velocity.

Results for 104 hours (4 days) have been obtained. These are shown in Figure 5.38 and 5.39. The alternate bar pattern forming in the channel is very similar to the experimental result (first panel in Figure 5.37). The general shape of the bars at 7 hours starts changing right away and looking at the flume results, within 16 hours a more similar alternate bar pattern is formed. This pattern is stable and the bar deformation seen in the flume does not happen the same way. The deformation is only happening as contour separations of higher sections in the channel, whereas in the flume the separated higher sections are moved to the middle of the flume. Another difference is that in the experimental results the bars show a small amount of propagation. In the simulations the propagation of the bars is very significant.

The deformation of the bars at 10 and 50 minutes shown in Figure 5.37 is similar to the bed evolution in the case where higher harmonics were included in the bed perturbation (see Figure 5.34 and 5.35). The two scour regions are connected with a channel-like feature (note the $-5m$ contour), which is destroyed at 80 minutes with the formation of higher bed forms. A similar channel forms also in Figure 5.35 at $t = 390min$ for the scour and higher regions (the blue and red areas). It is not as pronounced as in the flume case and its orientation is reversed. This only acts as a transition after which the same alternate bar pattern is formed.

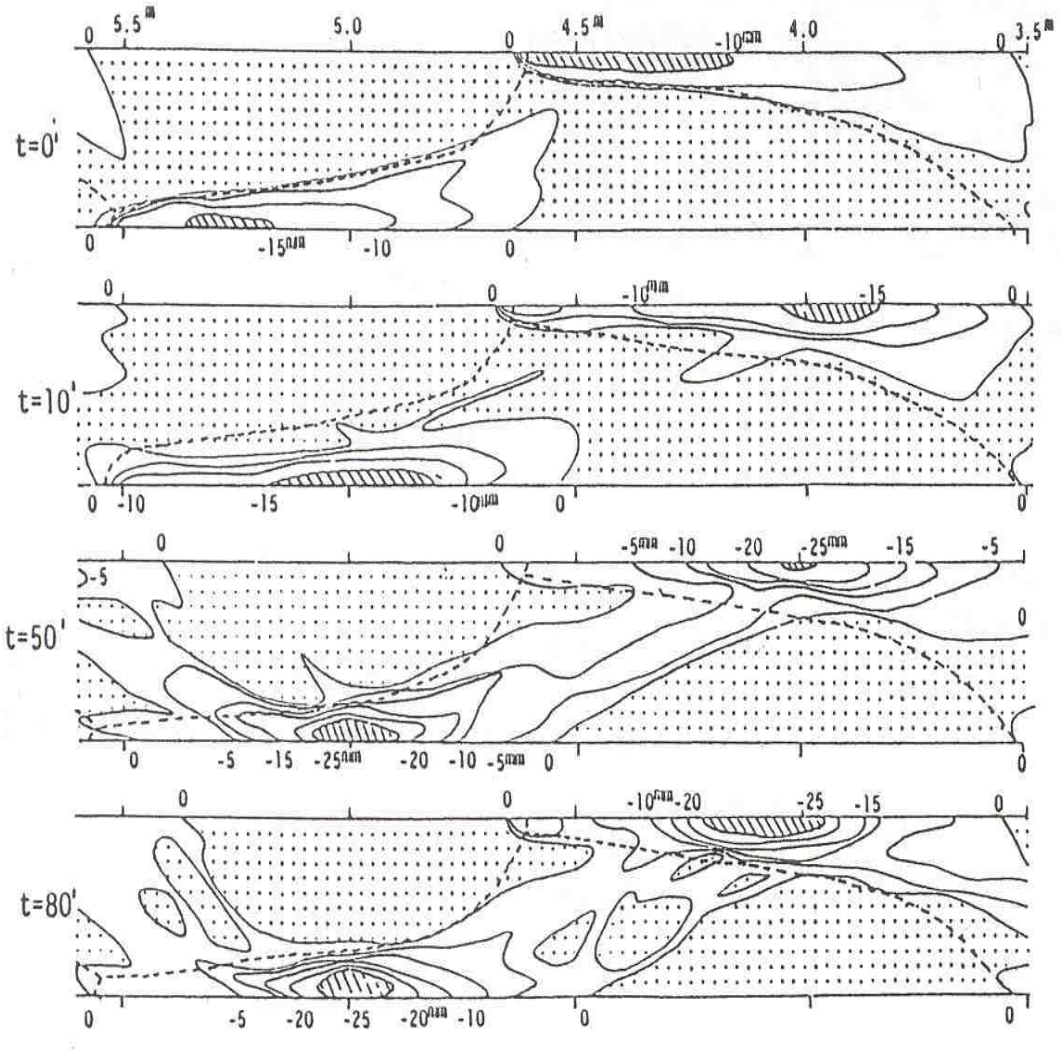

Figure 5.37: Alternate bar deformation in a laboratory flume (Uchijima, 1990). Hatched sections: scour, smudged sections: high bed level. The dashed line represents the barfront.

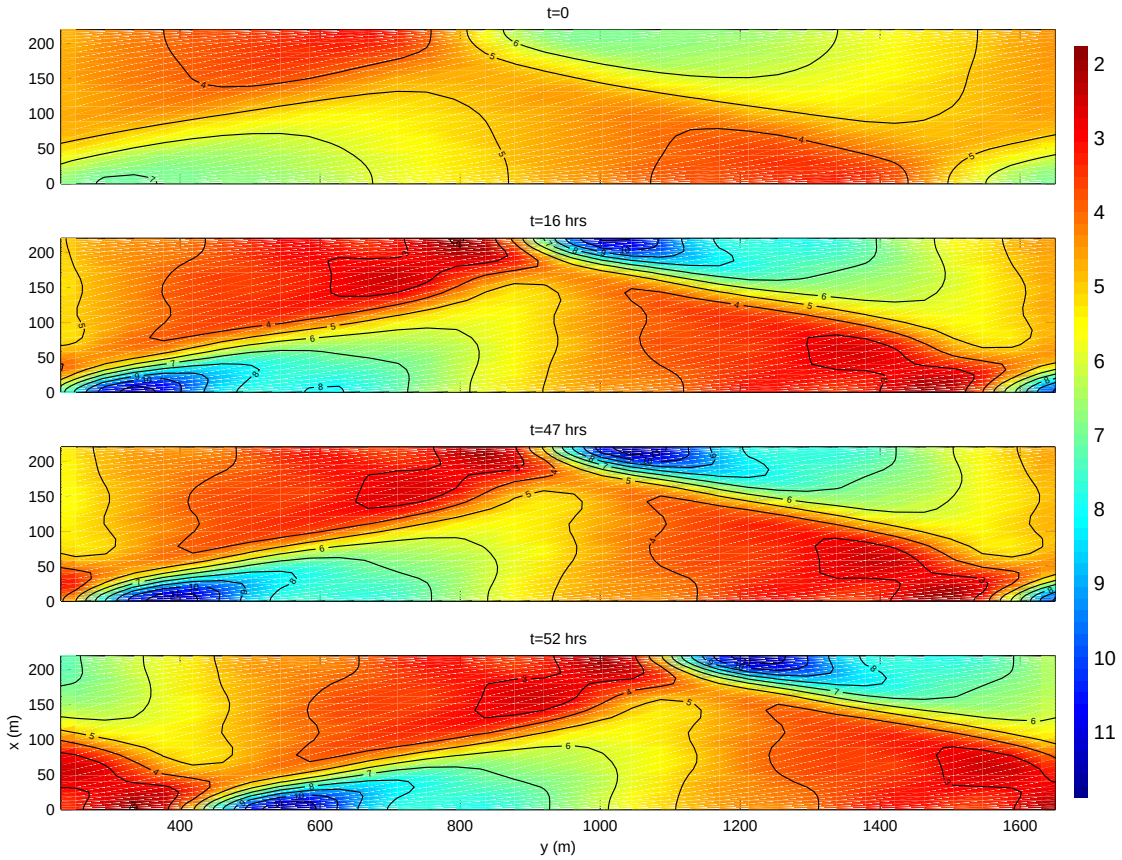

Figure 5.38: Simulated bed evolution with lower flow velocity for $k = 1.05$.

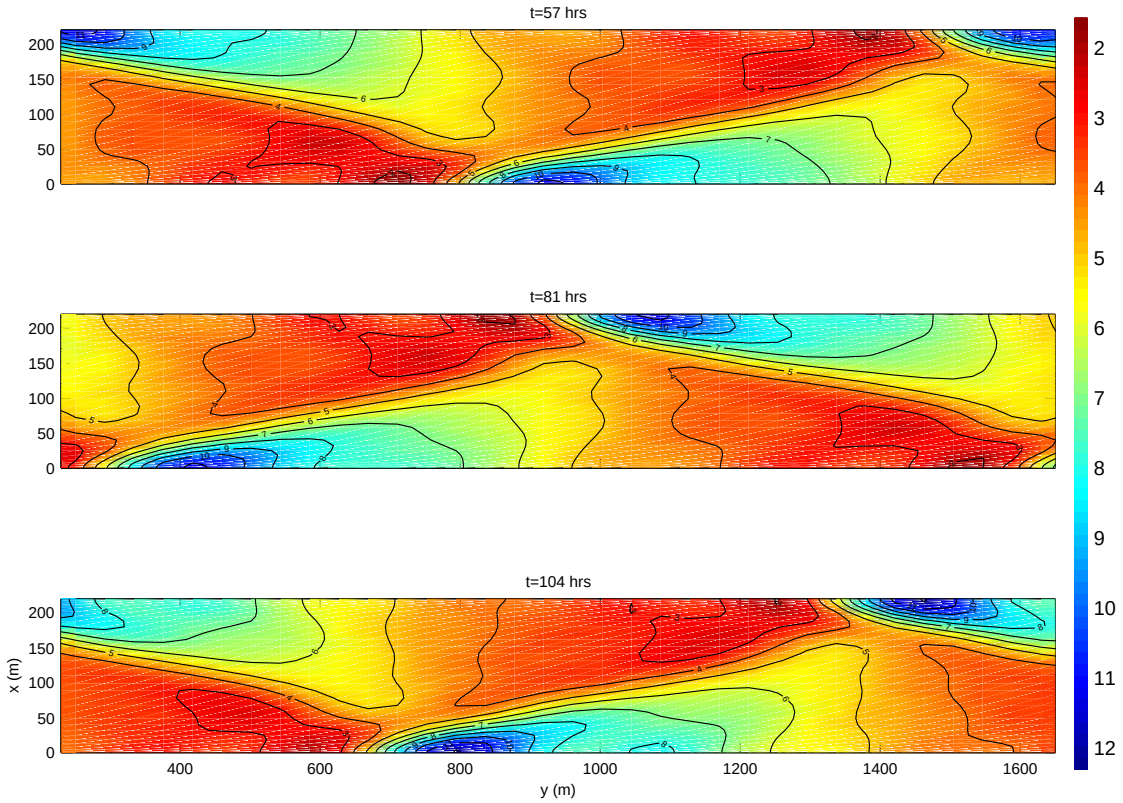

Figure 5.39: Simulated bed evolution with lower flow velocity for $k = 1.05$ (continued).

It is clear that in our results the bedforms attain a very stable form. The deformation of the bars is not triggered in the simulations. Although a similar flow condition was tried to be imposed in the runs, it may be that additional perturbations are necessary in the system which are obviously not present or not strong enough in our runs. One approach could be introducing a random and small perturbation to the flow field after reducing the flow. A bed perturbation with higher harmonics could have been used as well, but in the light of the previous results most probably this also would have been evolved to the same alternate bars.

Another uncertainty involved is the determination of a correct friction factor c_f and transport coefficient ν. Fixing the friction factor using an appropriate flow depth and adjusting ν accordingly seems to be the most suitable approach. It has to be kept in mind that the transport equation used in these simulations is fairly simple and effects like the grain size distribution or suspended sediment load are not included. Despite all of these uncertainties, it is striking that alternate bar patterns very similar to actual laboratory results can be predicted with such a simple sediment transport formulation.

5.9 Summary

In this chapter the evolution of bed instabilities in a rectangular channel are investigated. A standard stability analysis has been used to identify the most unstable wavenumber, the propagation and growth of the bed forms. With this information the bed is initially perturbed and the whole system is solved numerically including nonlinearities which are neglected in the stability analysis.

The coupled model first was tested for a channel case where a cross-channel slope was introduced as initial bed configuration. Results show that the model can predict the expected profile equilibriation.

In almost all of the simulations where initial bed perturbations were included, an obvious alternate bar pattern is formed in the channel. This pattern consists of sand waves with a steep wave front which was also predicted by Colombini *et al.* (1987) and Schielen *et al.* (1993).

Different effects on the bed evolution have been investigated, as well. Longer channels seem to have very slight effects on the bed evolution and resulting flow field. The most evident consequence of longer channels is that the bed forms evolve more freely and can propagate with higher speeds than predicted by the stability anlaysis. Contour pairing and separation also happens more frequently and faster in longer channels. Fluctuations around the steep wave front form in each case independent of the channel length. The corresponding flow field consists of a meandering along-channel stream. For longer channels the meandering nature may gain more strength.

Simulations for wavenumbers larger and smaller than the most unstable one show that the general alternate bar pattern is formed in each case. The growth and propagation predicted by the stability analysis matches the numerical results within acceptable limits, although we were only able to determine crude and approximate values from the simulations. For a larger wavenumber the resulting bar pattern was smoother than the ones for the most unstable wavenumber. The same case with a longer channel resulted in more fluctuating contours. For a smaller wavenumber spit-like features developed at high sections of the bars which were due to separating contours.

For two different friction factor values although the stability analysis predicts growth of the bed perturbations, the numerical results tend to show the opposite. In the simulations obtained for very small and very large c_f values growth only happens for a certain period, or not at all. The general characteristics of the flow field for smaller c_f values is that it is less energetic, so the stream is less meandering. This is also evident from the vorticity values obtained. For larger c_f values the meandering flow field is more pronounced. For a larger value of c_f, although the stability anlaysis predicts growth the bed forms reach equilibrium within a period of 10 hours and do not resemble the alternate bar pattern as before. Obviously for very small and very large values of the friction factor, the bed instabilities may evolve into different patterns and the linear stability analysis may be applicable only to a certain extend.

The velocity power b in the transport equation seems to be critical in the formation of alternate bars. As shown in the dispersion curves in Chapter 3, for $b = 2$ and $k = 1.05$

growth of bed instabilities does not happen. The numerical results also show that alternate bars do not form, but the bedforms decay as predicted by the stability analysis. For $b = 4$ the resulting patterns are very similar to the previous results.

The effect of including higher harmonics in the initial bed perturbation is in the form of significant deformations of the bar structure until the final configuration consisting of the same alternate bar pattern is attained. For a second perturbation which had one wavelength plus a half wavelength along-channel, no significant changes occured. A pattern similar to an alternate bar form developed, only with a larger wave followed by a smaller one this time.

The present model is able to predict alternate bar patterns very close to the pattern observed in the experimental study carried out by Uchijima (1990). The bar deformation observed at low flow was not predicted by the model. It is possible to obtain bed patterns qualitatively similar to observations and experimental results, but the bar deformation obviously involves other mechanisms which are not strong enough or not present in our simulations. Different perturbations can be introduced into the simulations which may act as mechanisms triggering the observed bar deformation. More accurate comparisons require the appropriate determination of ν and c_f, or a more sophisticated transport model which considers effects like suspended sediment load or grain size distribution. Another important point is that the model is not able to handle very low flow depths and small bed features due to numerical problems and extended simulation periods which in the practical sense may not be feasible.

Chapter 6

EVOLUTION OF MORPHODYNAMIC INSTABILITIES ON A PLANE BEACH

In this chapter preliminary results of bed evolution for a plane beach with initial bed perturbations are presented. The main focus is on the coupled evolution of seabed and flow instabilities. The sediment transport equation is the same used in the channel simulations.

A wall boundary condition is imposed at the shoreline in order to decrease computational time. The effect of a moving shoreline has not been addressed in this study.

The initial plane beach is perturbed with a small wave-like disturbance. The momentum forcing terms are computed using wave information specified at the offshore end of the domain. Two different wave and beach conditions are considered. The first one is for a mild sloping beach with low wave height and incident angle. The second case is for a steeper beach with larger wave height and incident angle. For each simulation two different instability types are imposed, bed-surf and bed-flow instability as described in Chapter 2. The effect of a different position of the initial bed perturbation is also investigated.

The results are mostly presented as snapshots of bed change contours, three-dimensional view of the resulting topography, flow field and corresponding vorticity. The following section contains a short description of the model formulation. The results are presented in section 6.2 and a summary is included in section 6.3.

6.1 Model Implementation

In order to obtain a plane beach topography, a bottom slope and an offshore open boundary are specified in the model. At the shoreline a wall boundary condition is specified. The condition of periodic lateral boundaries is retained. In this case x points in the offshore

direction and y in the longshore direction.

In accordance with the simulations for the rectangular channel case, in order to maintain spatial accuracy a minimum of 32 collocation points per perturbation wavelength in the y-direction and 32 points in the x-direction are utilized in the simulations.

The initial bottom perturbation is in the form of longshore periodic waves. This form has been obtained by including a sinusoidal change in the y-direction to the barred beach topography formula used by Deigaard *et al.* (1994). The resulting equation of the bed topography is as follows

$$h(x, y, t = 0) = h_o(x, y) - z_b(x, y)(h_o(x, y) - d_c) \tag{6.1}$$

where $h_o(x, y)$ is the unperturbed plane beach profile and

$$z_b(x, y) = z_a \exp\left(\frac{-d_1(x - x_c)^2}{x_b^2}\right) \cos(d_2 y)$$

The parameters x_c and d_c determine the still water depth over the perturbation and its location. The width of the perturbation is determined by d_1, and the amplitude can be adjusted with z_a. The alongshore wavenumber of the perturbation is governed by d_2.

In order to compute the flow field, the time-varying short wave field is determined by solving the energy equation including effects of shoaling and breaking. The linearized form of the energy equation including the effects of currents derived by Phillips (1977) can be expressed as

$$\frac{\partial E}{\partial t} + \frac{\partial}{\partial x}[E(u + c_g \cos\theta)] + \frac{\partial}{\partial y}[E(v + c_g \sin\theta)] + S_{xx}\frac{\partial u}{\partial x} + S_{xy}\left(\frac{\partial v}{\partial x} + \frac{\partial u}{\partial y}\right) + S_{yy}\frac{\partial v}{\partial y} = \epsilon_b \tag{6.2}$$

where E is the short wave energy density, c_g is the group velocity, θ is the angle of incidence, ϵ_b is the energy dissipation due to wave breaking, and S_{xx}, S_{xy} and S_{yy} represent the radiation stress tensor. The energy density, group velocity and the radiation stress components were described in Chapter 4.

The energy dissipation due to breaking ϵ_b is defined by Thornton and Guza (1983)

$$\epsilon_b = \frac{3\sqrt{\pi}}{16}\rho g \frac{f_p B^3}{\gamma^4 h^5} H_{rms}^7 \tag{6.3}$$

In this expression, H_{rms} is the root-mean-squared wave height and f_p is the peak frequency of the spectrum. The intensity of wave breaking is determined by the coefficient B which accounts for the different breaker types and can be considered as a function of the proportion of the foam region on the breaker face. The coefficient γ can be considered as a breaking index roughly relating water depth to wave height. Values of $B = 0.78$ and $\gamma = 0.45$ have been used.

The energy equation is integrated along with the other governing equations in the numerical scheme of the model. Initial values of the wave height, frequency and angle of

incidence are specified at the offshore end of the domain. For a smooth start-up, the offshore wave height is introduced using a ramping function in time.

The refraction of the waves is governed by the irrotationality of the wavenumber

$$\frac{\partial}{\partial x}(\tilde{k}\sin\theta) = \frac{\partial}{\partial y}(\tilde{k}\cos\theta) \tag{6.4}$$

This expression reduces to Snell's law for straight and parallel bottom contours. The dispersion relationship for the waves including currents is given by

$$(\omega - \tilde{k}u\cos\theta - \tilde{k}v\sin\theta)^2 = g\tilde{k}\tanh(\tilde{k}h) \tag{6.5}$$

Here $\omega = 2\pi\tilde{f}$ is the absolute frequency with $\tilde{f}$ being the short wave frequency. At every time step after the current velocities are computed the dispersion relationship is solved for $\tilde{k}$ using a Newton-Raphson iteration method. Given the offshore values of $\tilde{k}$ and θ, equation (6.5) is solved to determine the wave direction θ in the modeling domain.

The rest of the terms in the momentum equations were described in Chapter 4.

The parameters in the transport equation are chosen as $b = 2$ and $\gamma' = 1$. An arbitrary and small threshold velocity v_c is defined in the simulations. The rest of the parameters are described in each section.

6.2 Bedform Evolution Under Two Different Wave and Bed Conditions

A wave-driven flow field is considered over a specified topography. The wave field is resolved and thereby radiation stress components are computed as forcing terms in the momentum equations. Wave-current interaction and mixing processes are not included in the simulations. Refraction is included up to the level where the wave height is fully developed within the domain (due to the ramping function mentioned previously), so the bed change does not affect wave refraction. Sediment transport is activated after 1 hour of simulation time.

We consider two types of wave and beach conditions. In the first case the beach slope is mild. The offshore wave height and incident angle are low. This case can be considered similar to the situation referred to as 'wave-dominated' by Falqués *et al.* (1996b). The second case has a steeper beach slope with a larger offshore wave height and incident angle. This case is referred to as 'current-dominated'. The main aim is to observe how the bed evolution is affected by a strong current over a steeper beach, and a weaker current over a milder beach. The simulations for each wave and beach condition are also divided into 'bed-surf' and 'bed-flow' instability cases (Falqués *et al.*, 1996a, 1996b). In the case for bed-flow instability the bed instabilities do not affect the forcing terms in the momentum equations. This situation has been created by first running the model for a certain time in which the flow field developed over the specified topography. Then the numerical values of the forcing terms in both directions are used as input for the rest of the simulation when sediment transport is activated after 1 hour. Obviously, for this case the forcing is constant throughout the whole simulation. For bed-surf instability where the instabilities affect the

forcing terms, the simulation has been run without interruption and without using constant forcing terms as input.

Nondimensional wavenumber values for the initial bed perturbation have been chosen from cases presented by Falqués *et al.* (1996b). In these results values of $R = c_f/m$, the incident wave angle at breaking and the Froude number $F = U/\sqrt{gL_v}$ are given. Here $L_v = mL_H$ is a vertical length scale, L_H is a horizontal length scale corresponding to the offshore distance of the breaking point, and U is a velocity scale (see Chapter 2). In order to dimensionalize the wavenumber, the length scales are computed using the above given relations and the numerical results obtained from simulations for a planar beach with slope m and a chosen friction factor c_f. From the breaking wave angle the offshore incident wave angle is obtained through Snell's law. The offshore wave height has been determined considering only shoaling and also the simple relationship between the breaking wave height and water depth at the breaking point used in Falqués *et al.*'s study, so the breaking depth from the simulations approximately matches the one obtained by Falqués *et al.*. The length scales L_H and L_v then can be computed using the definition for the Froude number F and the velocity scale U. The cross-shore length of the domain and the wave period have been chosen arbitrarily. Since in this study we did not have direct access to the wavenumber-frequency curves for planar beaches, with this approximate approach we tried to obtain simulations close to the instability condition for given beach and wave conditions.

6.2.1 Deformation of Longshore Rhythmic Bedforms

For the first case, the nondimensional longshore perturbation wavenumber is $k = 3.5$. In computing these wavenumbers, lateral momentum mixing was also incorporated in the system (Falqués *et al.*, 1996b) whereas in our cases mixing is not considered. Lateral mixing may significantly affect the bed evolution, but in terms of growth of the bed instabilities the computed k values should not change significantly. Therefore, as the results confirm, excluding lateral mixing may not hinder the growth of the bed perturbation. Also, with the above mentioned approach in obtaining dimensional wavenumber values, lateral mixing effects can not be directly included.

The beach slope is $m = 0.006$ and the friction factor is chosen as $c_f = 0.003$. The offshore wave height and angle of incidence are $H_o = 0.3727m$ and $\theta_o = 6.9^o$, respectively. For a plane sloping beach this wave breaks around an offshore distance of $175m$ and the maximum longshore current occurs at $75m$. Using this length the dimensional wavenumber for this case is $0.0459rad/m$. An arbitrary peak period of $T = 7.7s$ and cross-shore domain length of $L_x = 350m$ have been used. The shoreline wall is $0.35m$ deep.

The bed perturbation is around the region of wave breaking with its highest point right at the breaking point. The parameters for the bed perturbation are $z_a = 0.2$, $d_1 = -15$, $x_c = 75$, and $d_c = 0.2$. The longshore length of the domain is chosen long enough to include two perturbation wavelengths. This corresponds to a length of approximately $L_y = 270m$. The spatial accuracy is again maintained by specifying 32 grid points per wavelength in the longshore direction and 32 grid points in the cross-shore.

The morphological time scale is chosen to be around 45 minutes. Using this time scale and the definitions for U, $F = 0.16$ and the length scales, a value of $\nu = 0.1107$ can be

obtained to be used in the transport equation. The critical velocity is $v_c = 0.0055 m/s$.

Bed-surf Instability Results

The results are shown as bed change and depth contours in Figures 6.1 and 6.2. The initial bed perturbation starts to change within half an hour after the sediment trasnport is activated. The bed change contours at 1.5 hours are very similar in shape to the results shown by Falqués *et al.* (1996a) (see Figure 2.5). Compared to their results this bottom change corresponds to the second mode. In the next 30 minutes, the first row of bed change around $75m$ offshore moves slightly in the flow direction as the second row which is closer to the shore moves in the opposite direction and connects with the first row. This corresponds to a spreading of the perturbation over the surf zone. Small oblique channels oriented in the flow direction are formed. In the next two hours the perturbation spreads further to the offshore as it grows. The topography changes to a complicated pattern in which still longshore periodicity can be identified. A three-dimensional view of the resulting topography is shown in Figure 6.3. The periodicity can be better observed in the contour plots.

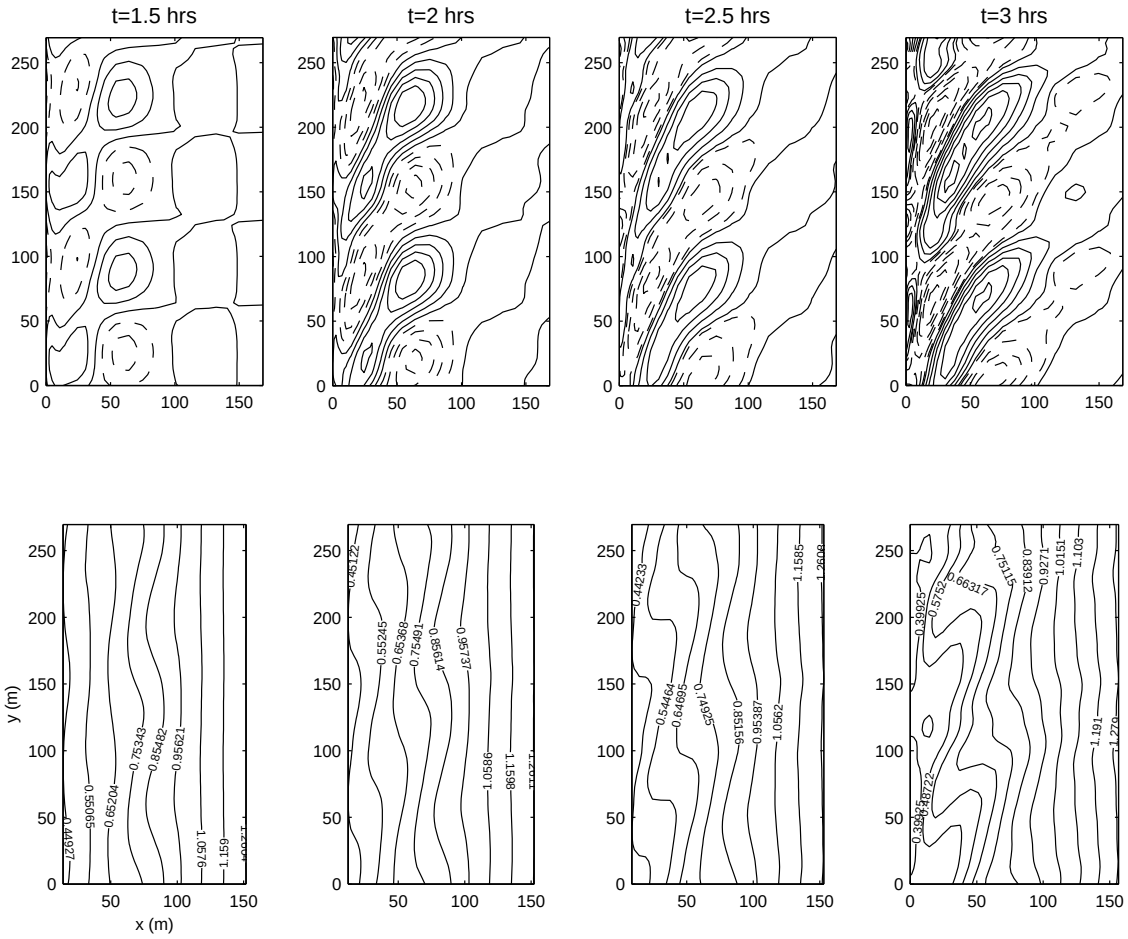

Figure 6.1: Simulated bed evolution for $k = 3.5$, $m = 0.006$, $H_o = 0.3727m$, $\theta_o = 6.9^o$, $f = 0.13rad/s$, $c_f = 0.003$. Top panel: bed change contours (dashed lines: erosion, solid lines: deposition). Bottom panel: topography.

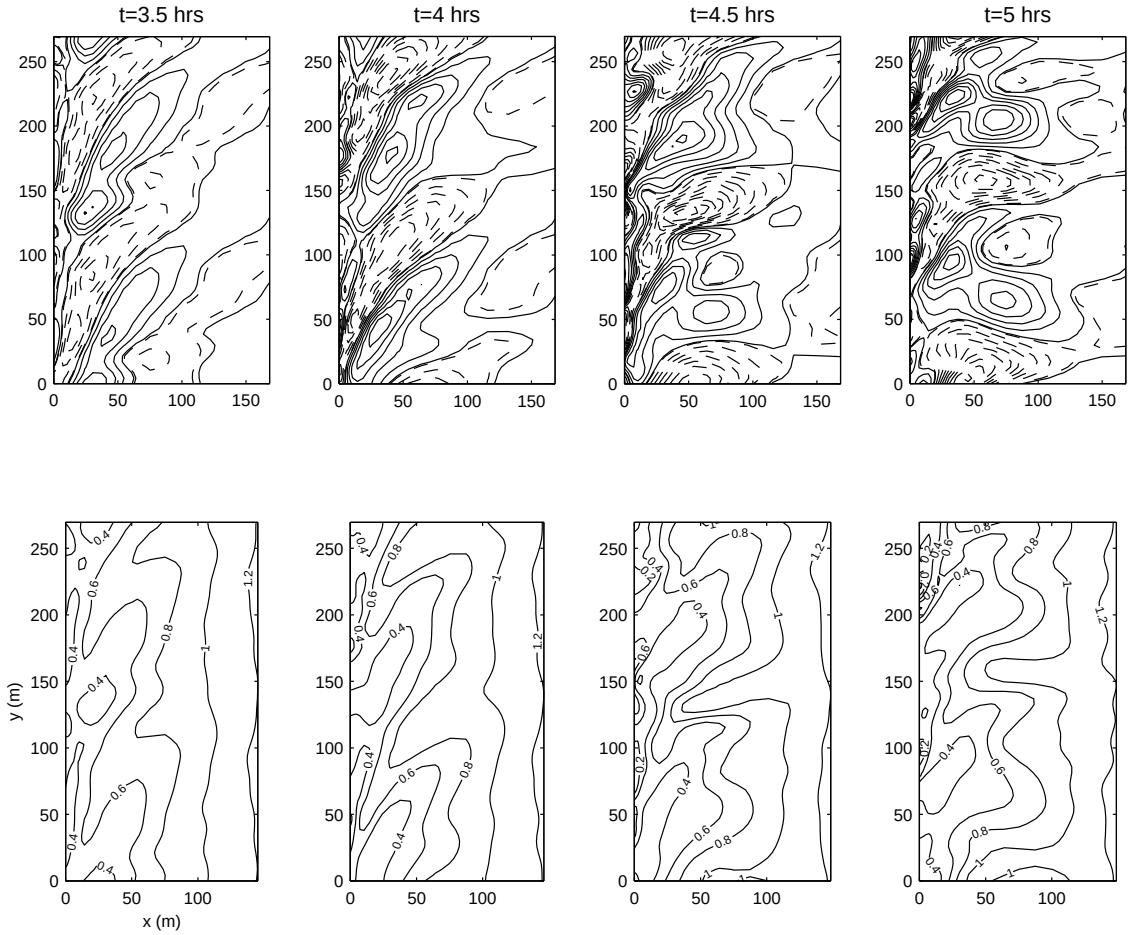

Figure 6.2: Simulated bed evolution for $k = 3.5$, $m = 0.006$, $H_o = 0.3727m$, $\theta_o = 6.9^o$, $T = 7.7s$, $c_f = 0.003$ (continued). Top panel: bed change contours (dashed lines: erosion, solid lines: deposition). Bottom panel: topography.

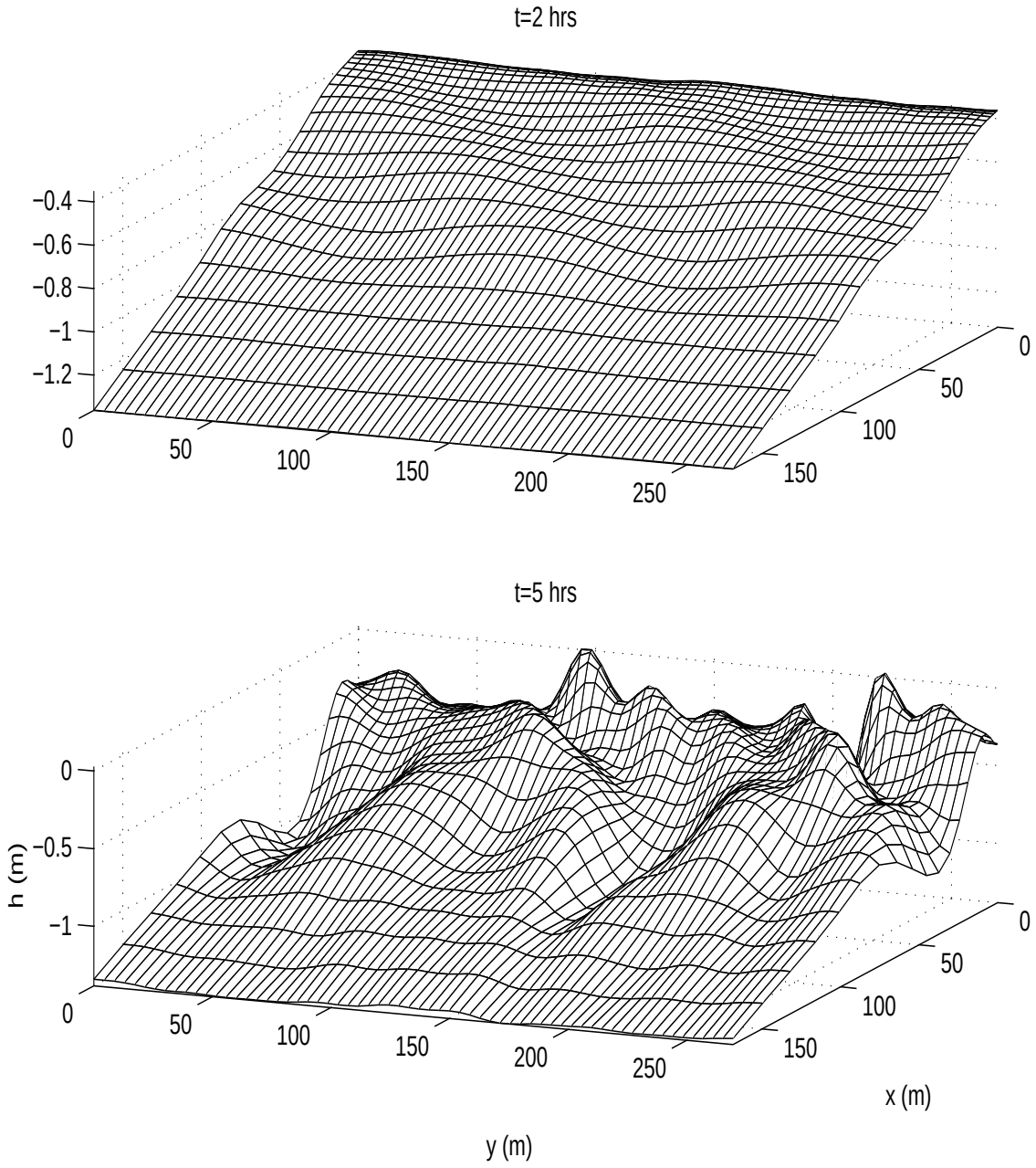

Figure 6.3: 3D view of the topography for $k = 3.25$. The flow is from left to right.

Utilizing the same cross-correlation method used for the channel simulations in order to determine the longshore speed of the bedforms, an approximate interval of $0.005 - 0.014 m/s$ can be obtained. The average value is $C_{bed} \approx 7.7 m/hr$.

The resulting topography is comparable to laboratory observations of skewed rhythmic bedform development under oblique waves (Sonu, 1973). According to these observations the offshore located bed feature (a bar or, as in this case, a bed perturbation) spreads over the surf zone as it gets skewed and finally attaches to the shore forming small spit-like features (Figure 6.4). In our simulation a directly shore-attached feature may not be so easy to develop since islands forming at the shoreline would cause the model to stop, which in fact happens in this simulation. After 5 hours the sand waves forming at the shoreline wall exceeded the wall depth. It is still possible to see the formation of the spit-like forms, especially at 4 hours (note the smaller $0.4m$ contour towards the shoreline). Although the smaller one is destroyed by the formation of the oblique channel, a second similar form grows as it starts propagating in the flow direction (the larger $0.4m$ contour).

Snapshots of the flow field, the vorticity and the corresponding depth contours are shown in Figure 6.5. Velocity vectors every second grid point in the longshore direction are plotted to maintain a better visual resolution. Although the wavy structure of the longshore current is evident, vorticity only starts to gain more strength as the topography becomes more complicated. There are strong vorticities very close to the shore moving alongshore and some are shed offshore. The maximum absolute velocity values ($|V_m| = \sqrt{u^2 + v^2}$) are included in the title of each snapshot. Note how the depth contours match the flow field, especially at the points of high vorticity.

The Effect of a Different Initial Bed Perturbation Location

The effect of moving the bed perturbation slightly offshore has been investigated in the next simulation. Using the same parameters the bed perturbation is moved to around $100m$ offshore. With this length scale the dimensional perturbation wavenumber becomes $k = 0.0345 rad/m$. This gives a longer beach where $L_y \approx 360m$. The wall at the shoreline is smaller for this case, $h_o = 0.1m$.

The resulting bed evolution is very similar to the previous case (Figure 6.6). Due to the location of the perturbation the bottom change spreads to a longer offshore distance, and the shoreline is affected after 7.5 hours when the bed starts forming shoals at the shoreline wall. The bottom attains a complicated though visually more periodic pattern. Similar patterns of shoals and channel-like structures evolve (Figure 6.7). The longshore bedform speed values range between $0.0031 m/s$ and $0.0062 m/s$. The average value is $C_{bed} \approx 3.42 m/hr$.

The flow field with alongshore moving and offshore shedding vorticities is also very similar to the previous results (Figure 6.8). The only difference being that the vorticity field looses some of its strength in time, although the velocity magnitudes are very close. This means that the flow field is not as energetic as in the previous results in terms of its meandering and vortex structure, probably due to the smoother bed evolution and slower bedform propagation.

In both these cases, the initial bed perturbation evolves into a rather complicated

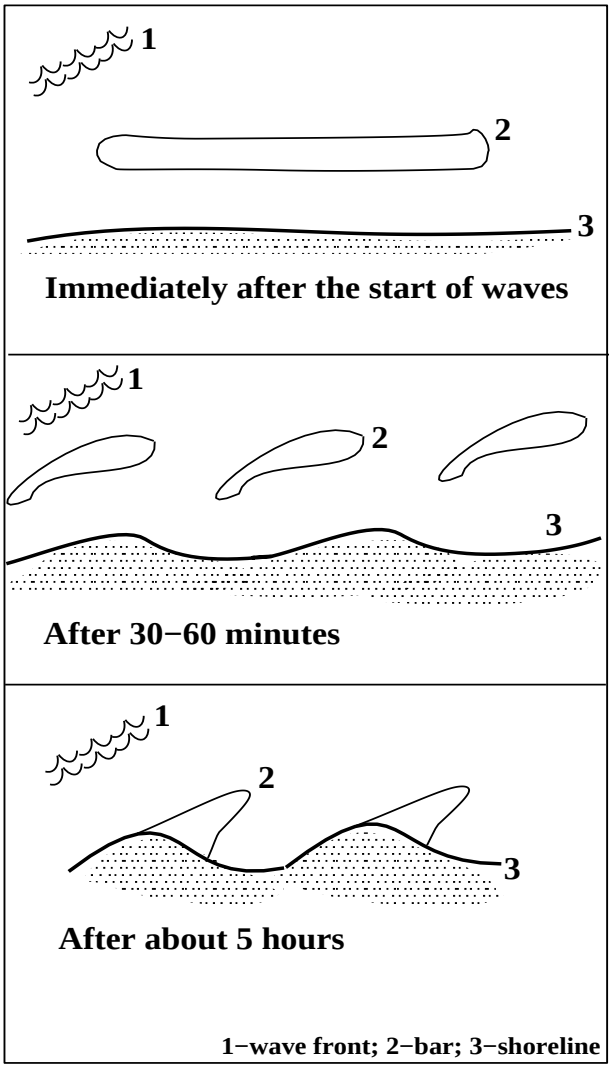

Figure 6.4: Laboratory observation of the development of a skewed rhythmic topography under oblique waves (after Sonu (1973)).

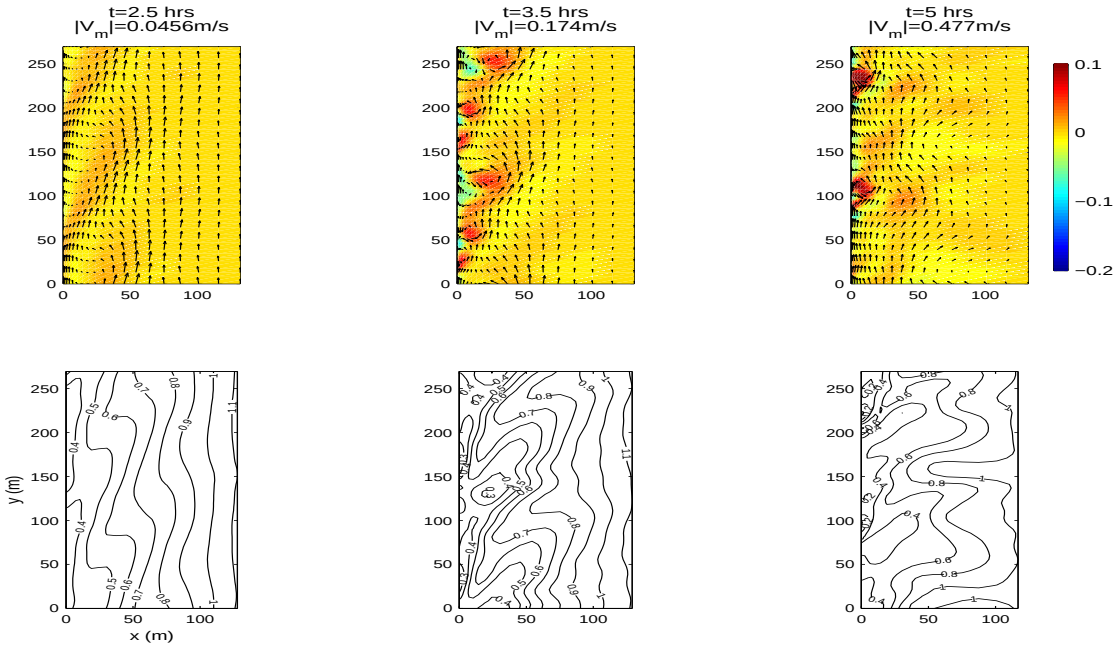

Figure 6.5: Upper panel: snapshots of the flow field and corresponding vorticity for $k = 3.5$. Lower panel: snapshots of the corresponding depth contours for $k = 3.5$.

pattern where still some periodicity remains. Instead of growth of only the initially perturbed area, the topography changes to a series of longshore periodic bump and channel-like scour regions and their growth continues as they spread over the profile, especially at the shoreline. The overall propagation is small and happens significantly only at the offshore and shoreline regions. Growth continues until shoals form at the shoreline. Considering that the bottom evolution is taking place in a considerably short duration, a larger morphological time scale and therefore a smaller transport coefficient ν can be chosen in order to let the bed evolve over a longer period. The determination of a realistic ν value depends on many factors, and as a rather uncertain coefficient it is still possible that such significant bed evolution can happen in such a short time with the corresponding ν value used in these simulations.

For both cases the bed evolution resembles the patterns observed in the sequence of rhythmic shoal formation under oblique wave action at Seagrove, Florida shown by Sonu (1973). The alongshore length scales of the bedforms more-or-less match the numerical results and the channel-like formations are significantly similar, although in the observations this evolution happens over a period of several days and the incident wave angle changes from oblique to shore normal.

Bed-flow Instability Results

In the next results constant forcing terms are used in the momentum equations. The rest of all the parameters are kept the same as in the first simulation. The initial bed perturbation is located at an offshore distance of $x = 75m$.

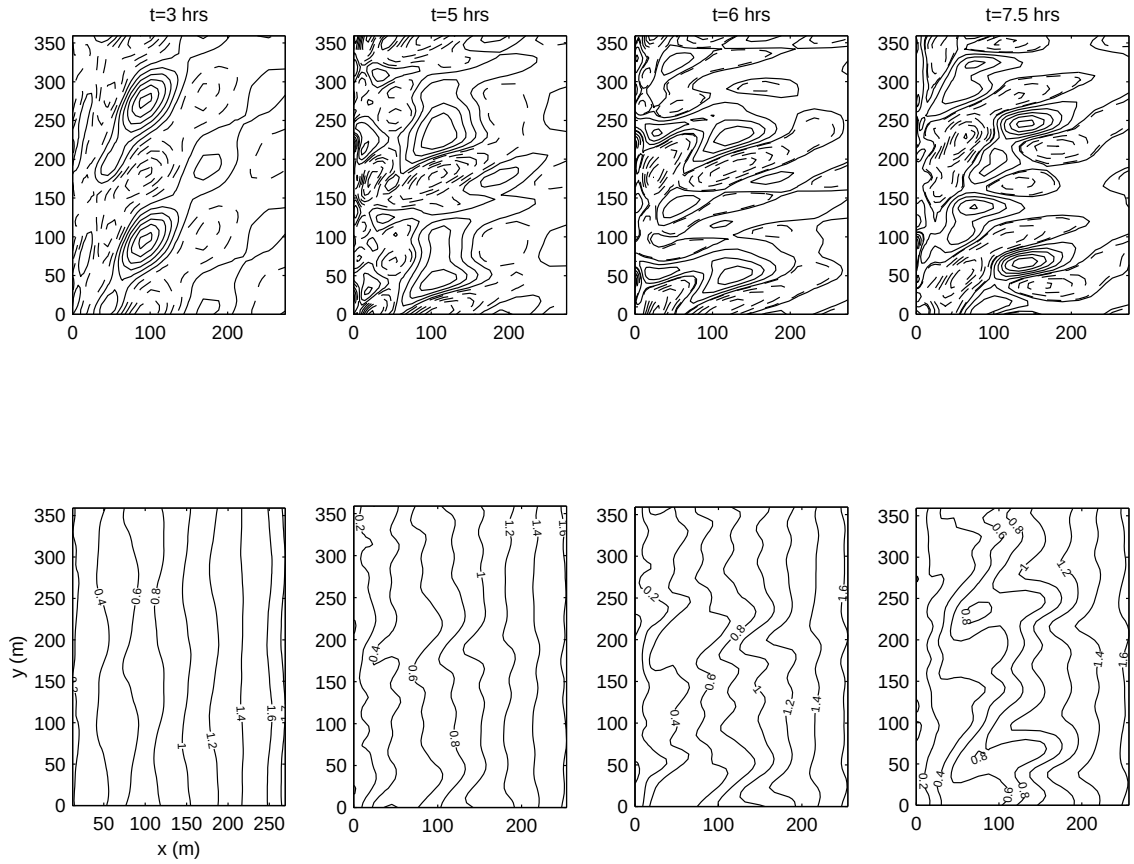

Figure 6.6: Simulated bed evolution for $k = 3.5$, $m = 0.006$, $H_o = 0.3727m$, $\theta_o = 6.9^o$, $T = 7.7s$, $c_f = 0.003$. Initial bed perturbation located around $x = 100m$. Top panel: bed change contours (dashed lines: erosion, solid lines: deposition). Bottom panel: topography.

It was possible to carry out the simulation for a whole day. Unlike in the first results, shoals did not grow out of the water at the shoreline in this case. The bed evolution is smoother and more organized compared to the first two examples. Periodicity of the bedforms is easily recognizable. The depth change and resulting topography are shown as contour plots in Figures 6.9 and 6.10. Compared to the previous results, the bed starts changing in a very similar way within the first 2 hours. Following that, channel-like scour regions form, but this time they are not as obliquely oriented as before although the depth contours have almost the same values. At 4.5 hours two sand waves at the shoreline (the $0.4m$ contour) and two wavy regions skewed in opposite directions have significantly evolved further offshore (the $0.5 - 0.6m$ and $0.8 - 0.9m$ contours). This becomes even more evident in the next 3 hours. The overall longshore propagation of the bedforms is very small and the lag-correlation method used in Chapter 5 to determine their speed reveals that at certain intervals they do not propagate at all. The average propagation speed is $C_{bed} = 4.278m/hr$. In the later stages the bedforms at the shoreline go through a series of pairing and separation, forming smaller sand waves and spit-like features. This starts smoothing out after 18 hours as the two oppositely oriented sand wave regions evolve into one. At 22.5 and 24

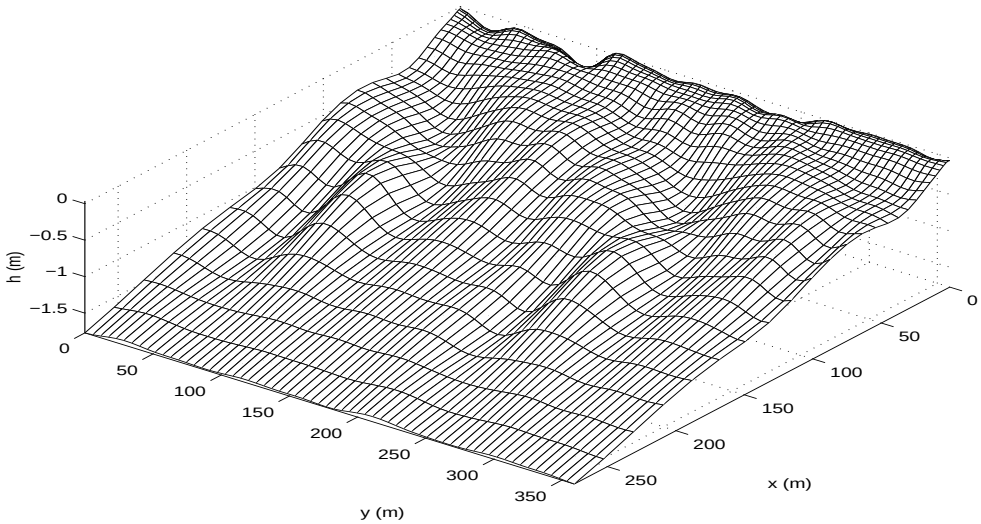

Figure 6.7: 3D view of the topography for $k = 3.25$ at $t = 7.5$ hours. Initial bed perturbation located around $x = 100m$. The flow is from left to right

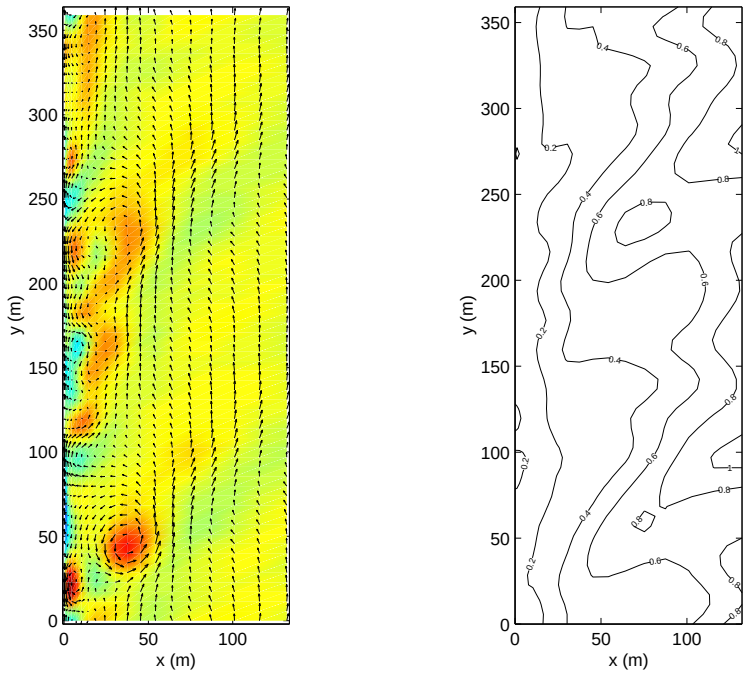

Figure 6.8: Left panel: flow field and vorticity ($|V_m| = 0.448m/s$). Right panel: corresponding depth contours for $k = 3.25$ at $t = 7.5$ hours. Initial bed perturbation located around $x = 100m$.

hours the channel-like regions are oriented in the flow direction and the sand waves at the shoreline are also smoother. The three-dimensional view of the bed evolution sequence is shown in Figures 6.11 and 6.12. The oblique orientation of the bars is more evident in these figures. The longshore propagation of the bedforms closer to the shoreline is more obvious than the ones located further offshore. The general trend of the bed evolution is in the form of cross-shore spreading as the oblique bars and channel-like scours form.

The depth change contours look similar to the results presented by Falqués *et al.* (1996a), although their shape slightly changes in time. According to Falqués *et al.*'s results the simulated depth change contours correspond to a cross-shore mode number of 5 if the offshore contours are counted as well. The number of modes depends on the cross-shore domain length and the offshore extend of regions where effective sediment transport is happening. The highest number of modes shown by Falqués *et al.* is 4.

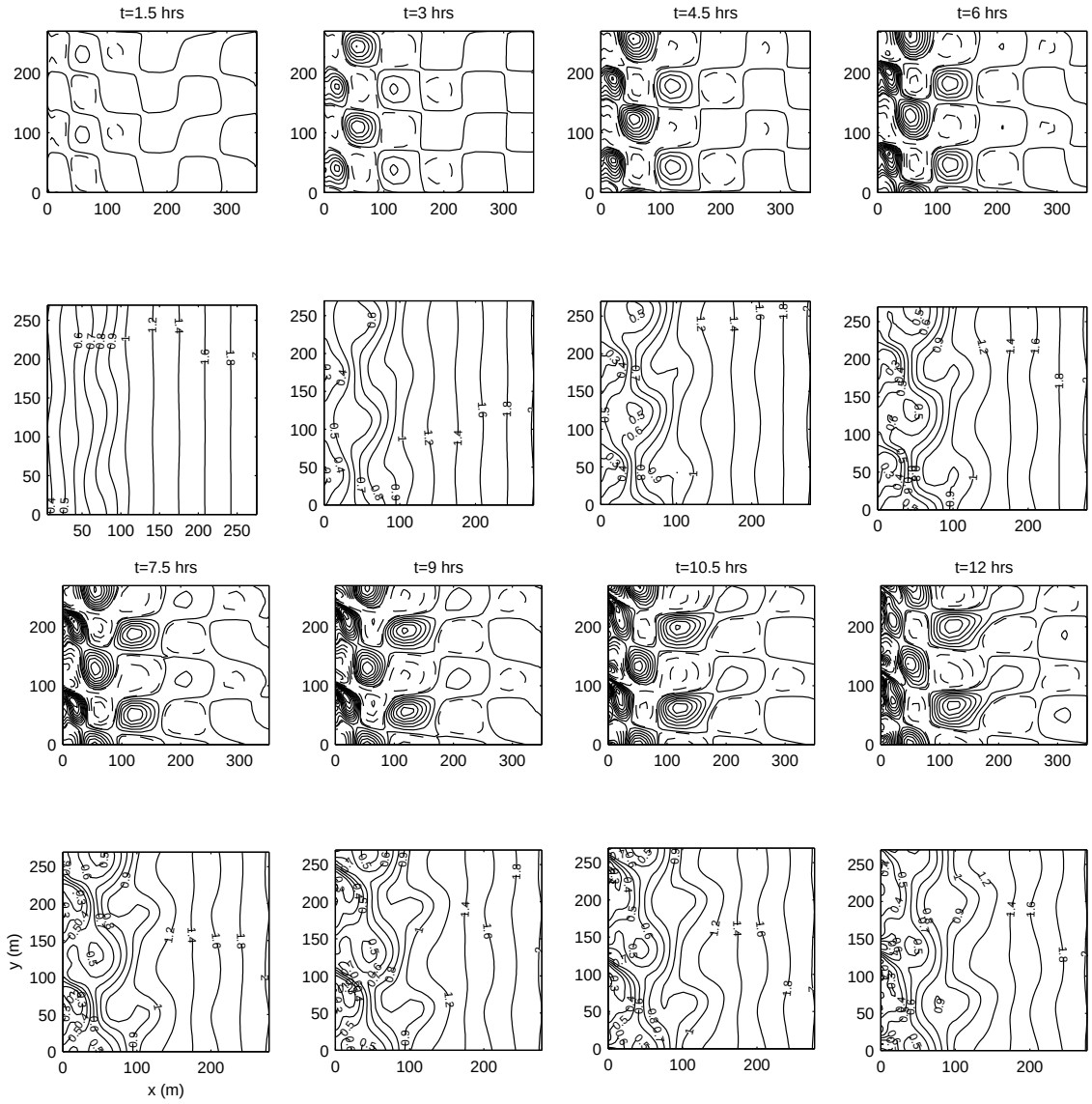

Figure 6.9: Simulated bed evolution for $k = 3.5$, $m = 0.006$, $H_o = 0.3727m$, $\theta_o = 6.9^o$, $T = 7.7s$, $c_f = 0.003$ with constant momentum forcing terms. First and third panel: bed change contours (dashed lines: erosion, solid lines: deposition). Second and bottom panel: corresponding topography.

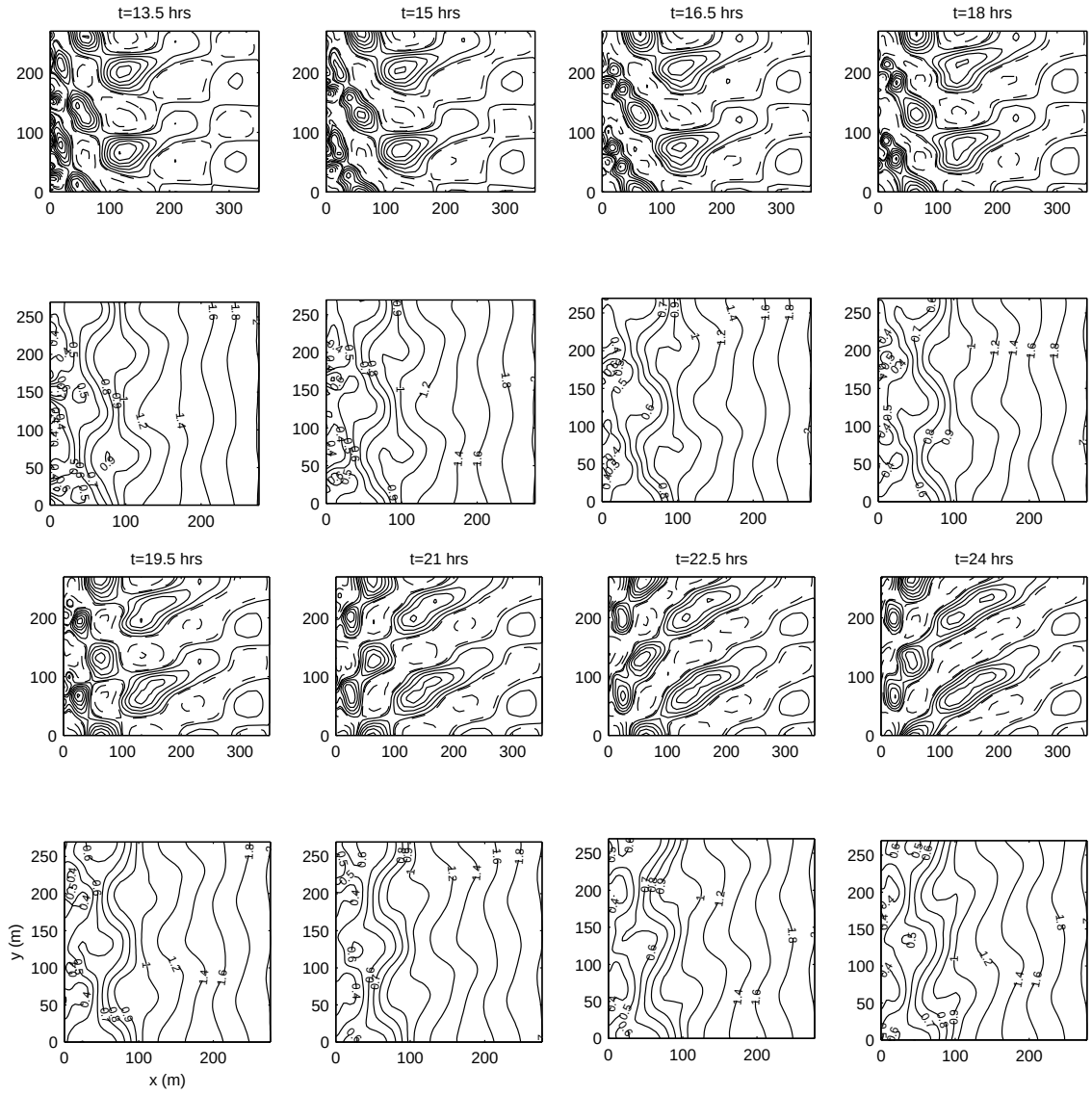

Figure 6.10: Simulated bed evolution for $k = 3.5$, $m = 0.006$, $H_o = 0.3727m$, $\theta_o = 6.9^o$, $T = 7.7s$, $c_f = 0.003$ with constant momentum forcing terms (continued). First and third panel: bed change contours (dashed lines: erosion, solid lines: deposition). Second and bottom panel: corresponding topography.

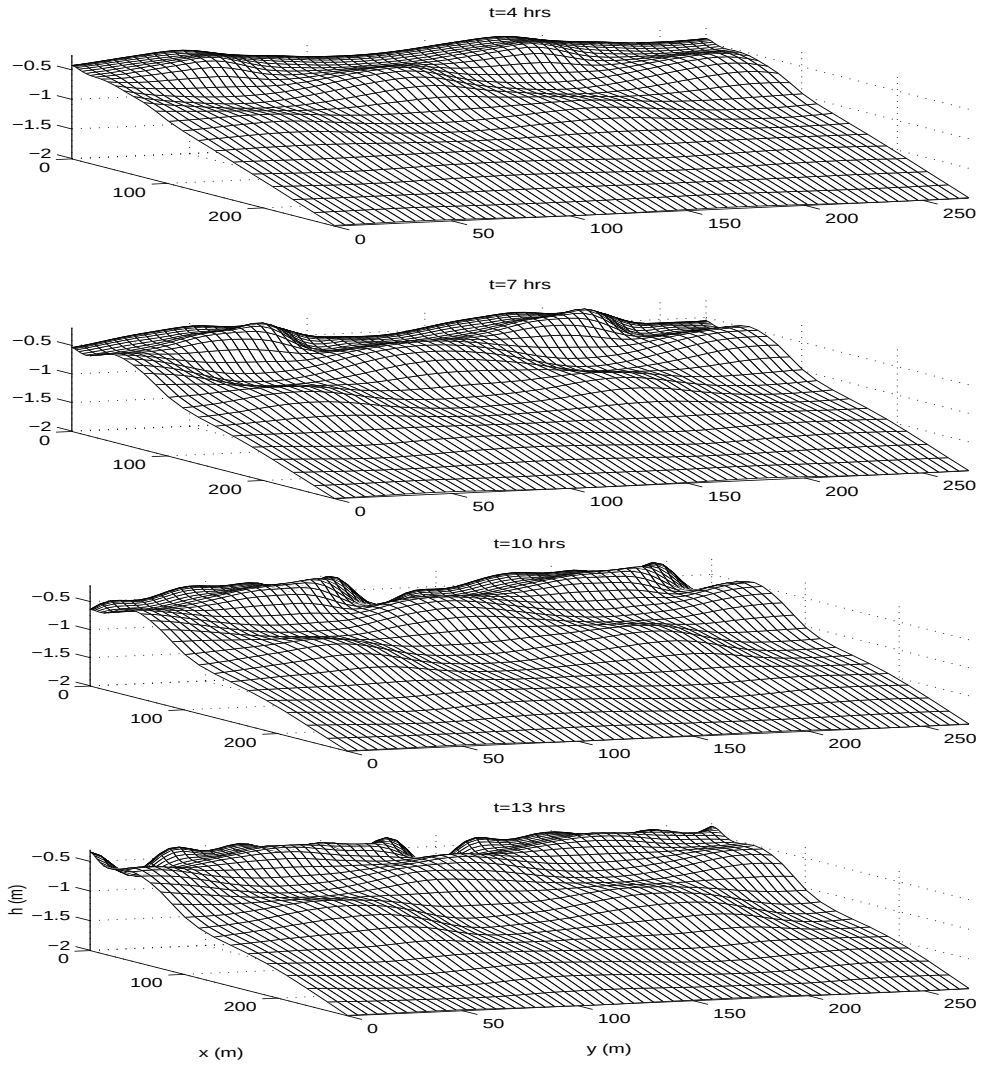

Figure 6.11: 3D view of the topography for $k = 3.25$ with constant momentum forcing terms. The flow is from left to right.

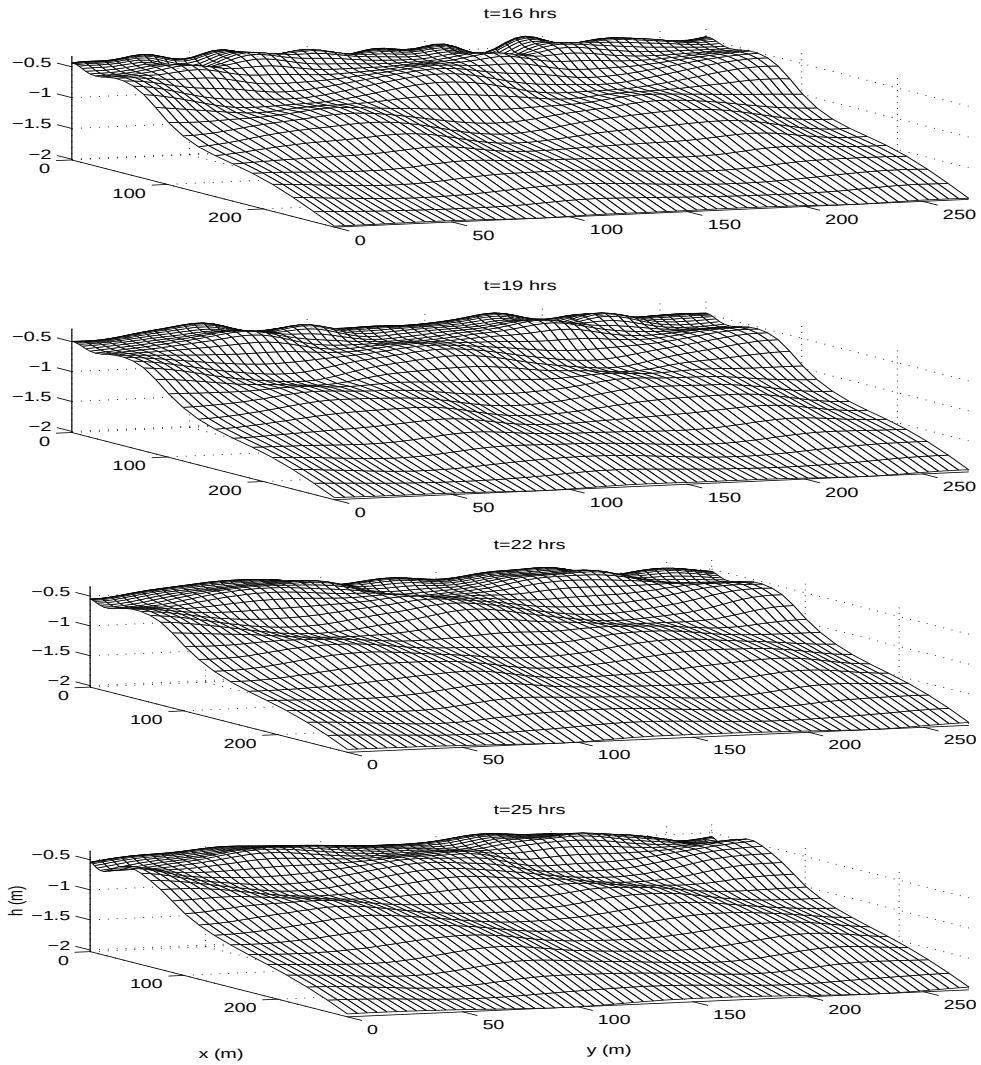

Figure 6.12: 3D view of the topography for $k = 3.25$ with constant momentum forcing terms. The flow is from left to right (continued).

The flow field matches the resulting topography. The velocity vectors at every second grid point in the longshore direction, the corresponding vorticity and depth contours are shown in Figure 6.13. Note that two rows of meandering longshore current have formed, the first between $x \approx 25 - 50m$ and the second between $x \approx 70 - 100m$. The velocity vectors converge over the holes and diverge over the bumps. Longshore propagation of the vorticity is generally happening slightly closer to the shoreline, but overall the velocities are stable and do not change magnitude and orientation a lot.

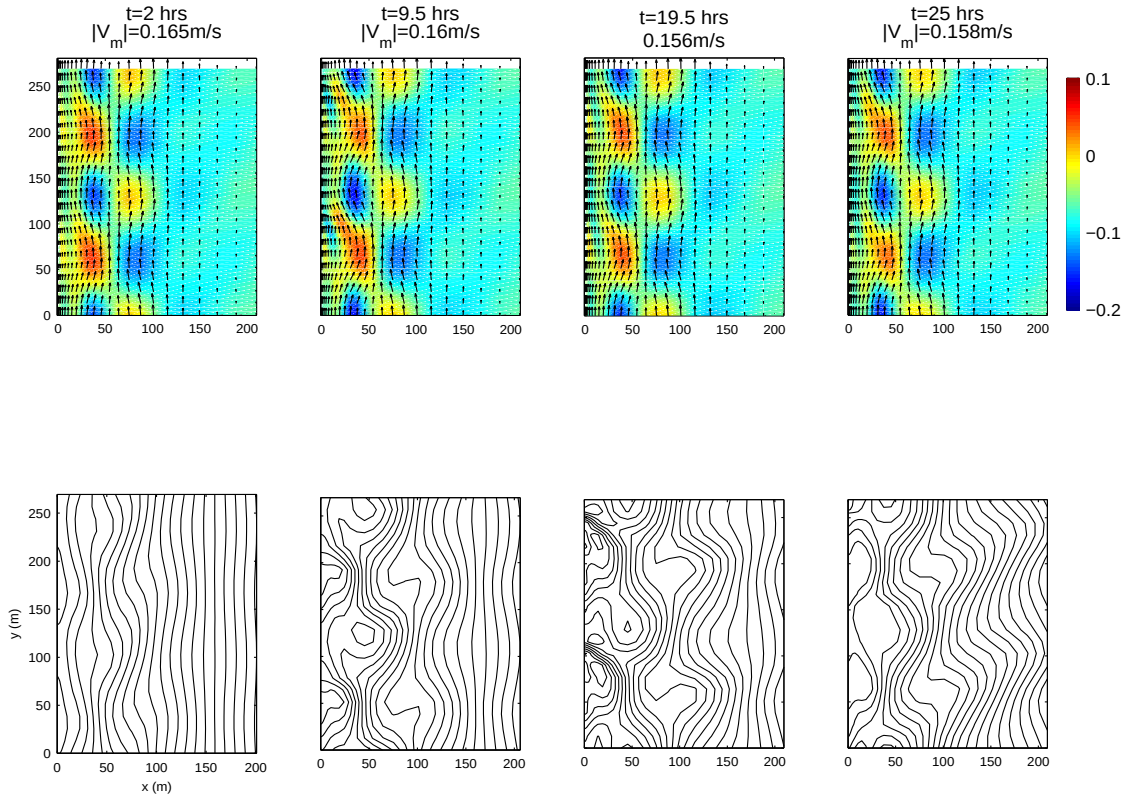

Figure 6.13: Top panel: snapshots of the flow field and vorticity. Bottom panel: corresponding depth contours for $k = 3.25$ with constant momentum forcing terms.

6.2.2 Formation of Cusp Pattern

In these simulations the beach has a steeper slope of $m = 0.03$. A higher offshore wave height $H_o = 0.91m$ and a larger incident angle $\theta_o = 25.33^o$ with the same period $T = 7.7s$ have been used. The nondimensional perturbation wavenumber for the bed is $k = 1.14$ which gives a longshore domain length of approximately $L_y = 1112.4m$. The location of maximum bed perturbation is around the breaking point which is $L_H \approx 45m$. The parameters for the bed perturbation are $z_a = 0.1$, $d_1 = -15$, $x_c = 45.3$, and $d_c = 0.2$. The shoreline wall is $0.05m$ deep.

The morphological time scale is 1 hour which corresponds to a transport coefficient of $\nu = 0.00447$. Since the resulting velocities are expected to be much larger than the previous case, a higher critical velocity value of $v_c = 0.2m/s$ has been used.

Bed-surf Instability Results

The trend of erosion/deposition and therefore the bed evolution are completely different in this case. Depth change contours are shown in Figure 6.14. Here, erosion happens in the region between the shoreline and the initial bed perturbation. The eroded material is deposited offshore while the initial perturbation is also spread over the profile. Alongshore propagating sand waves form at the shoreline wall as the bed slope significantly decreases to about 0.013 for that specific region which extends to about $x = 45m$ offshore. A slightly wavy bar covers the profile between $x \approx 50m$ and $x \approx 200m$. The sand waves towards the shoreline are more significant. This configuration is also evident in Figure 6.15 where cross-shore profiles of the initial and final topography are shown.

The sand waves forming towards the shoreline can be better seen in Figures 6.16 and 6.17 where the three-dimensional planform of the topography is shown for the last 8 hours of the simulation. In accordance with the initial bed perturbation and the alongshore domain length, two waves are forming in the alongshore direction. The sand waves continue to grow as they propagate and as the bed slope at that portion of the profile continues to decrease. The tendency of sand waves to form seems to be more pronounced over milder bed slopes. Note that the amplitude of one of the waves is larger than the other one. The wavy bottom forming offshore can also be seen, although very insignificant compared to the sand waves towards the shoreline. The sand waves attain a steeper wave front similar to the bedforms evolving in the channel simulations. After 22 hours the wave with smaller amplitude starts leaving the domain as the one behind it seems to reach a higher amplitude.

The formations at the shoreline wall can be considered as large cusp formations. Falqués *et al.* (2000) identified very similar bedforms in their stability analysis performed on a plane beach under a wave-driven flow field. In their study this type of formation is associated with a constant stirring function involved in the sediment transport equation. This is essentially the same transport equation used in the present study. The stirring function is the coefficient ν. Falqués *et al.* (2000) also considered cases where a cross-shore variation was assumed for this function. For a constant function the bottom perturbation extends to the

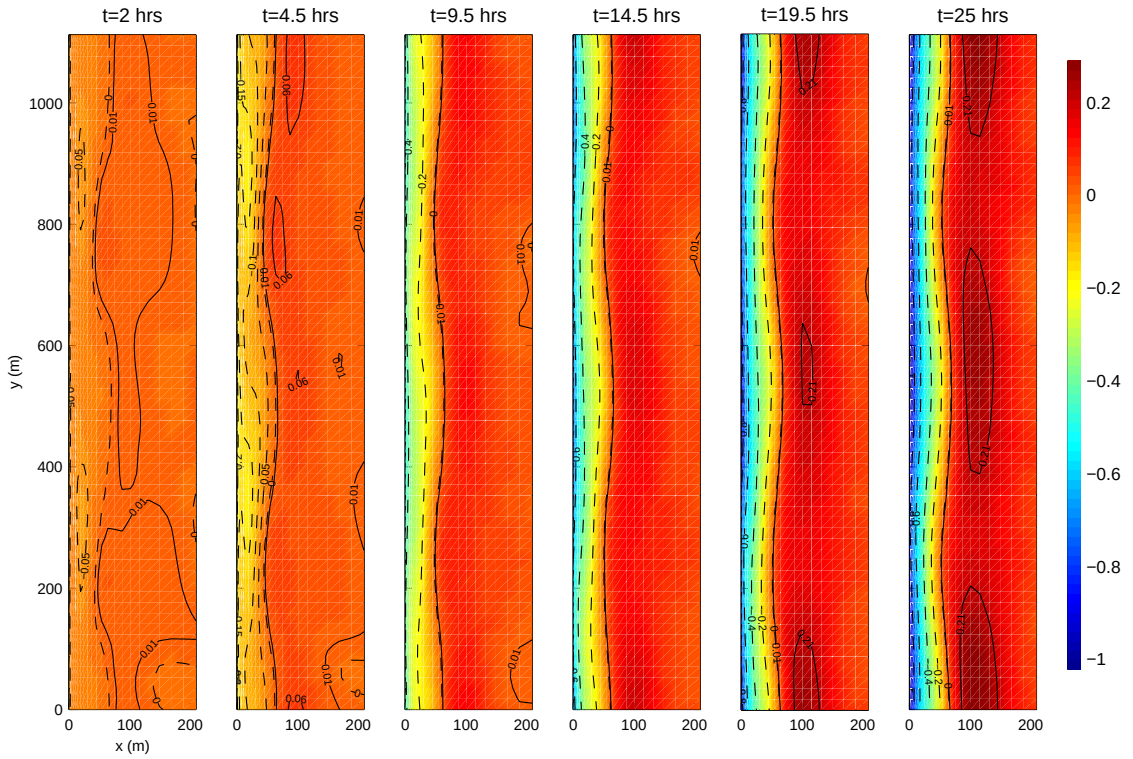

Figure 6.14: Depth change contours for $k = 1.14$, $m = 0.03$, $H_o = 0.91m$, $\theta_o = 25.33^o$, $T = 7.7s$, $c_f = 0.003$. Negative contours correspond to erosion, and positive to deposition. The flow is from bottom to top.

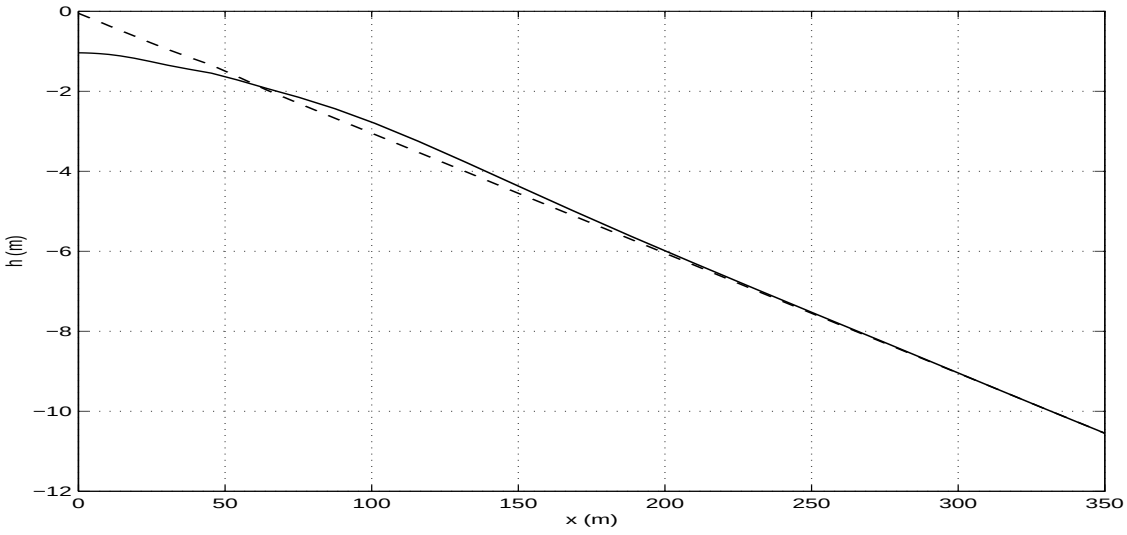

Figure 6.15: Bed profile at $y \approx 88m$ for $k = 1.14$, $m = 0.03$, $H_o = 0.91m$, $\theta_o = 23^o$, $T = 7.7s$, $c_f = 0.003$. Solid line: profile at $t = 25hrs$, dashed line: initial profile.

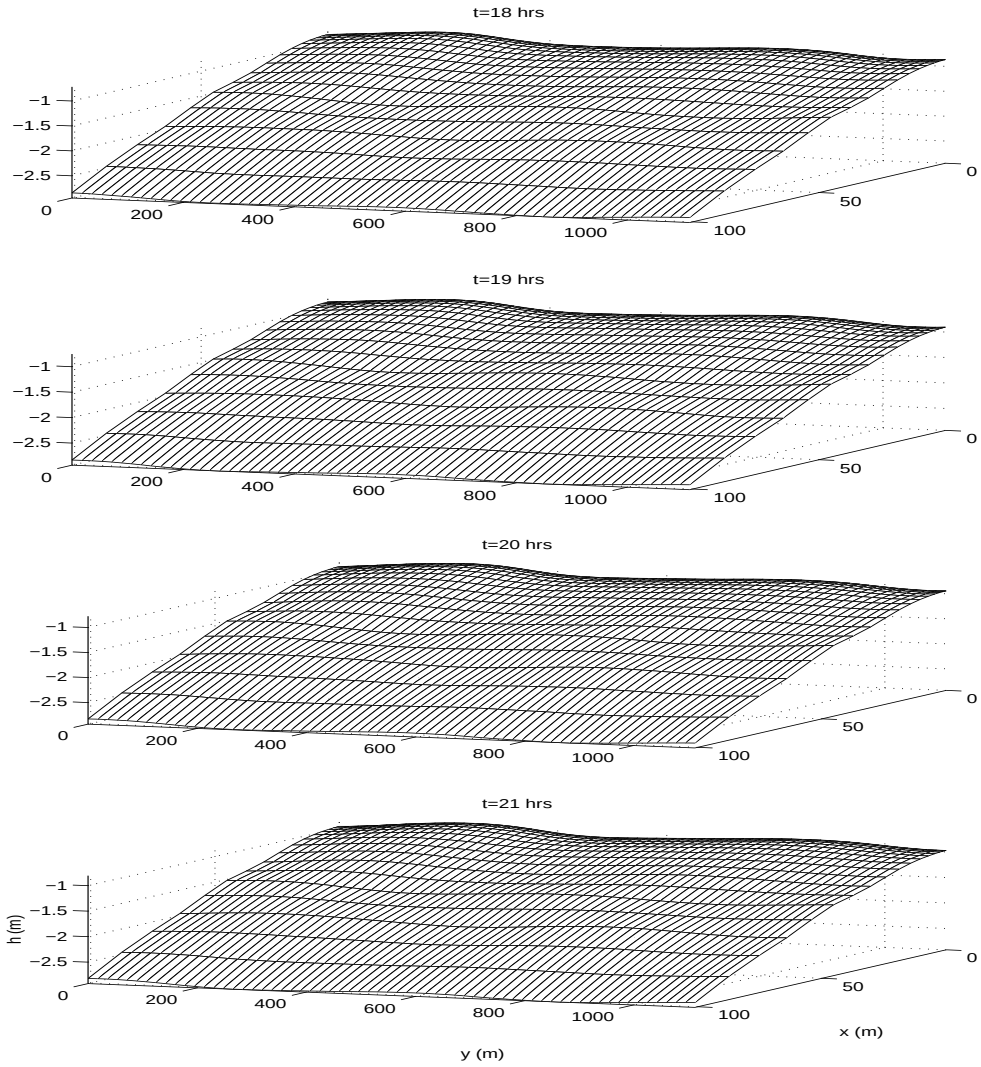

Figure 6.16: 3D snapshots of the topography for $k = 1.14$. The flow is from left to right.

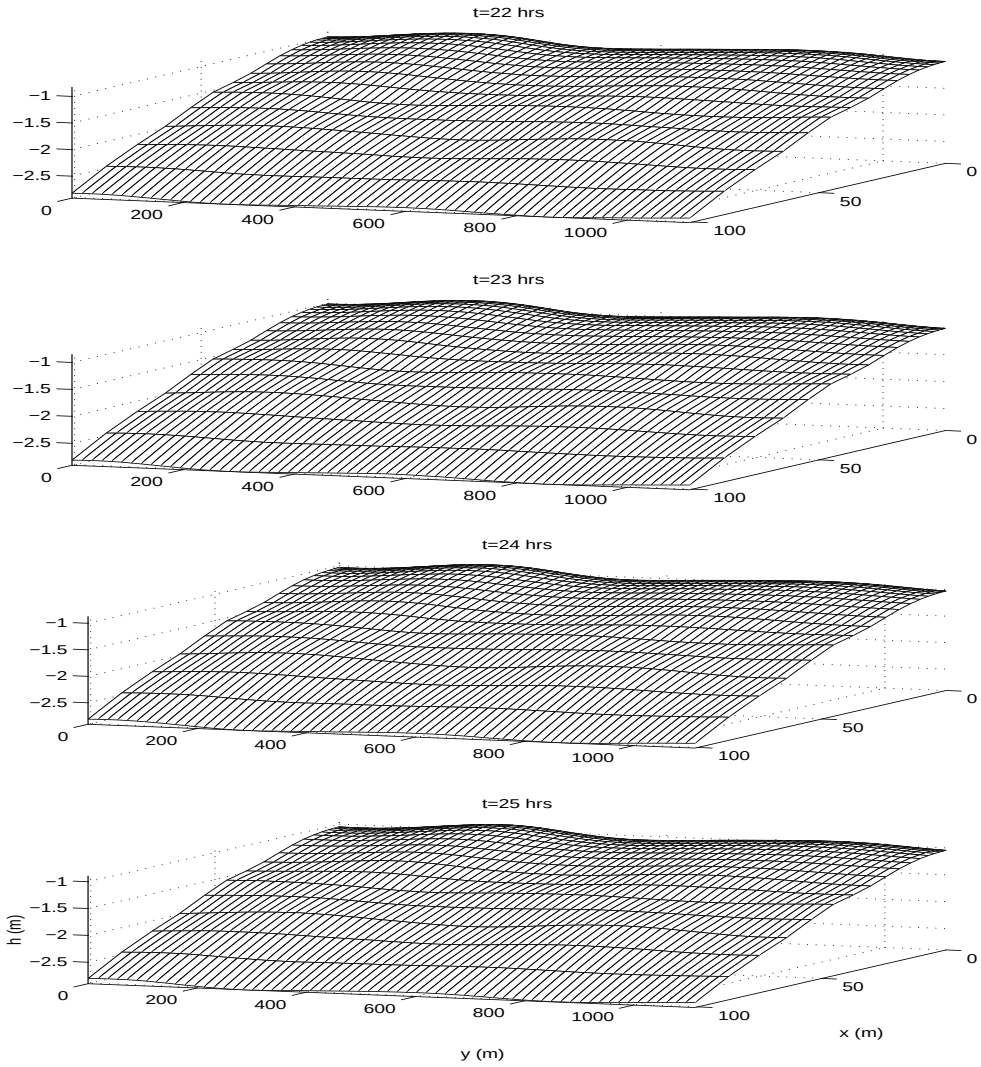

Figure 6.17: 3D snapshots of the topography for $k = 1.14$. The flow is from left to right (continued).

shoreline just as in our case, although no change occurs in the profile slope. Most probably for longer simulation periods, the profile where the cusps are located will continue to erode until equilibrium is reached with the offshore located wavy bottom. One thing to keep in mind is that this transport equation does not consider transport due to waves, so cross-shore profile changes are only due to slope effects and cross-shore directed mean flows. The model can not predict on-offshore transport depending on waves or the effect of undertow.

The resulting flow field is suprisingly different than the previous case and the results by Falqués *et al.* (Figure 6.19). The flow pattern is very energetic and the longshore flow goes through a series of deformations in the form of offshore shedding vorticies and alongshore meandering. In general the flow field seems to be rather unaffected by the bed evolution. The cusps forming at the shoreline have very little effect on the flow field, since no visually detectable changes occur in the flow field. From the snapshots it is evident that the vortex structure is propagating alongshore while gaining or losing strength. Studying the time series of u, v and h taken over the bed perturbation, periodic movement of the flow field is not obvious (Lower time series in Figure 6.18). The time scales associated with these fluctuations are fairly short, less than 30 min for each series. In addition to the short scale fluctuations an almost linear increase is associated with h, which corresponds to erosion.

This flow pattern is similar to some of the cases Özkan-Haller and Kirby (1999) observed in their simulations for plane and especially barred beaches, but in their results shear waves are definitely present and the onset of the flow instability can not be considered due to the topography.

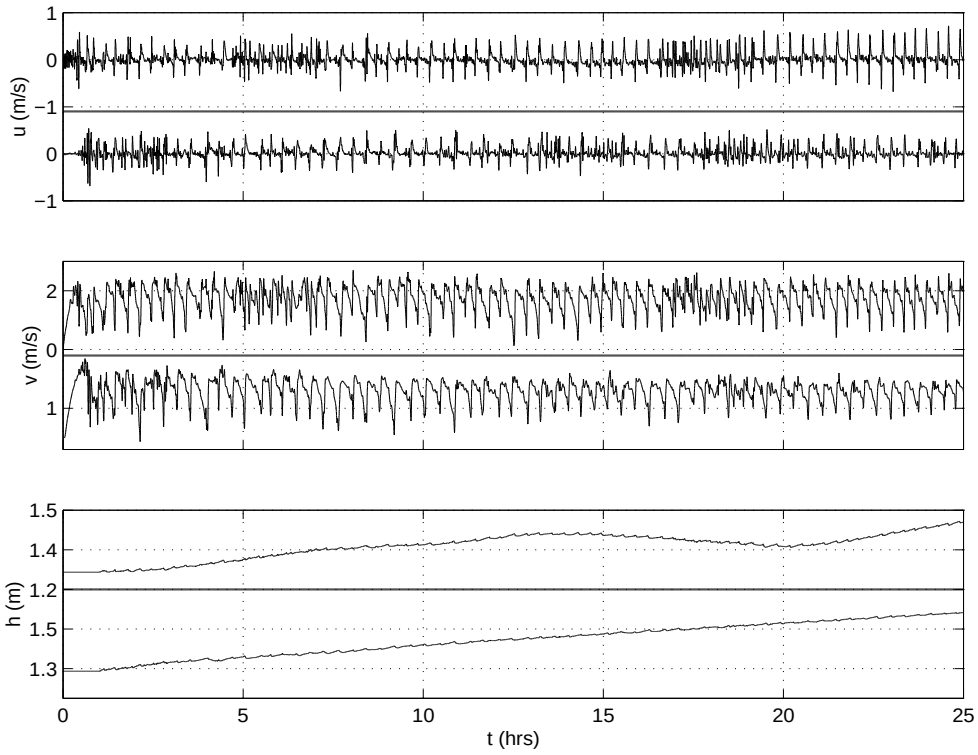

Figure 6.18: Time series of u, v and h at $(x, y) = (45.3m, 0.5L_y)$ for $k = 1.14$. Upper series: bed-flow instability, lower series: bed-surf instability.

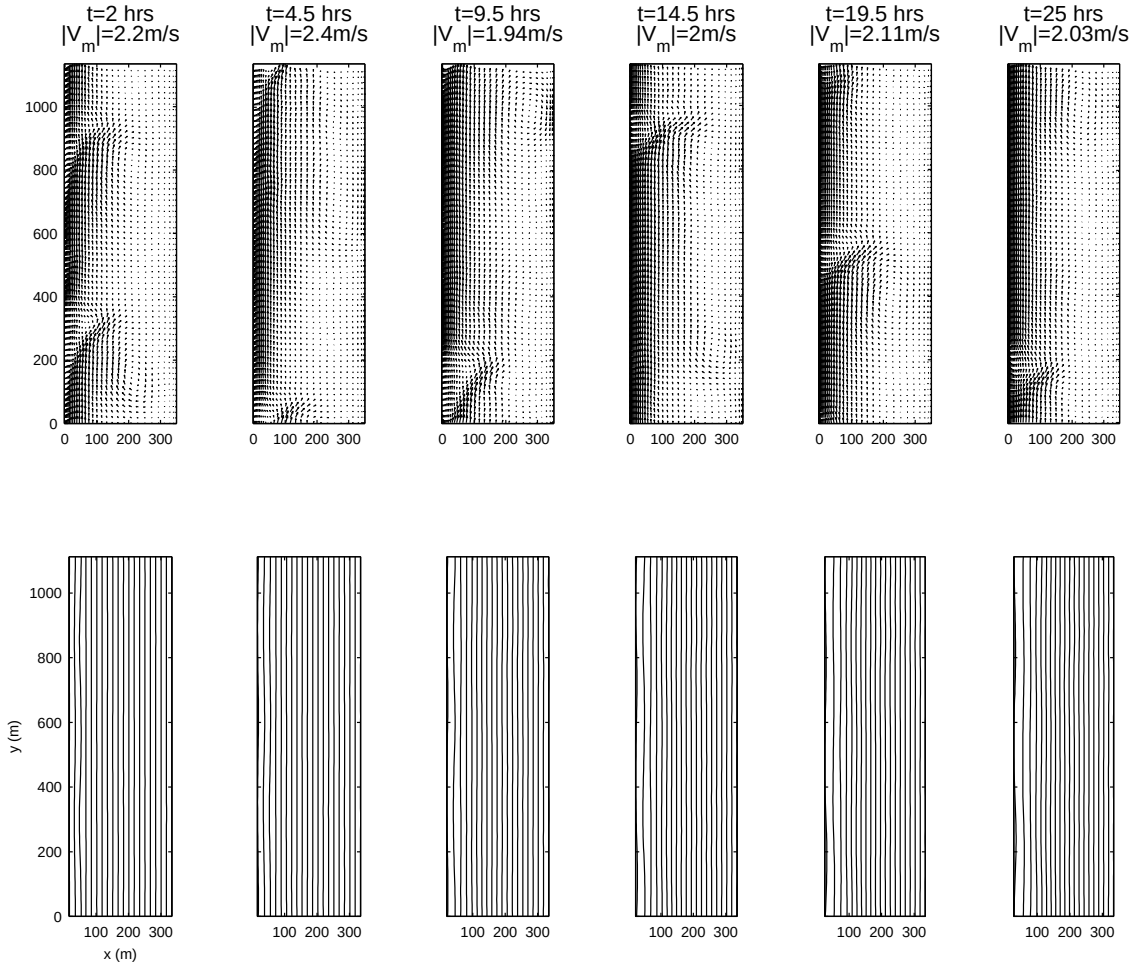

Figure 6.19: Upper panel: snapshots of the flow field, lower panel: corresponding bathymetry for $k = 1.14$.

Bed-flow Instability Results

The results for bed-flow instability where constant forcing terms are used in the momentum equations are presented next. All of the parameters are the same as before.

Depth change contours are shown in Figure 6.20. The major difference from the previous results is that for this case more erosion and deposition happens. The general shape of the bed deformation is very similar to the previous case. The sand waves forming towards the shoreline wall have a larger amplitude and they also travel faster, which is evident in the three-dimensional snapshots of the topography shown in Figure 6.21. Here again the sand waves towards the shoreline form over a milder bed slope which decreases down to approximately 0.00625.

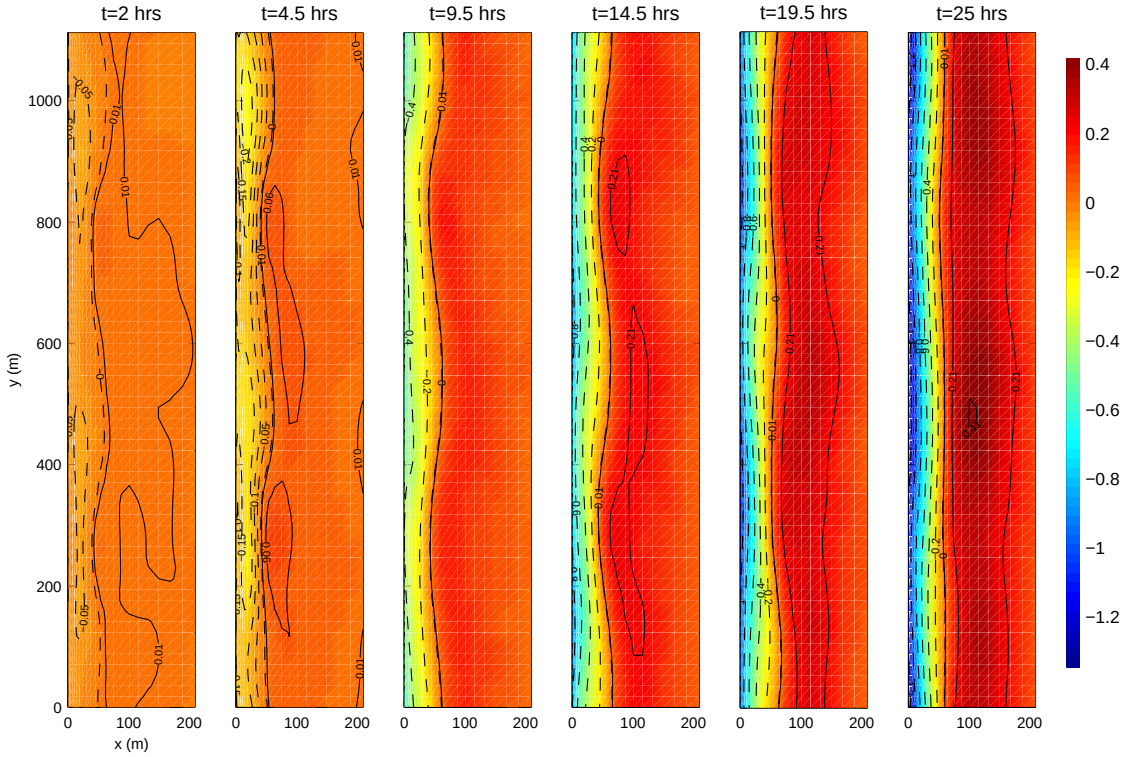

Figure 6.20: Depth change contours with constant forcing terms in the momentum equations. Negative contours correspond to erosion, and positive to deposition. The flow is from bottom to top.

Time series of u, v and h are shown in Figure 6.18 (upper series). The fluctuations are almost the same as in the case of bed-surf instability. The amplitudes are larger for this case, especially after the first 10 hours of the series. The bed change also attains an additional larger fluctuation around the same time, as it deviates from its almost linear increase.

The flow field is very similar to the previous simulations with bed-surf instability. The same trend of longshore propagating vorticies is present with a slight increase in the velocity magnitudes. A direct match between the velocity vectors and the bathymetry is not possible. Due to the very similar character of the resulting flow field, the results are not shown here.

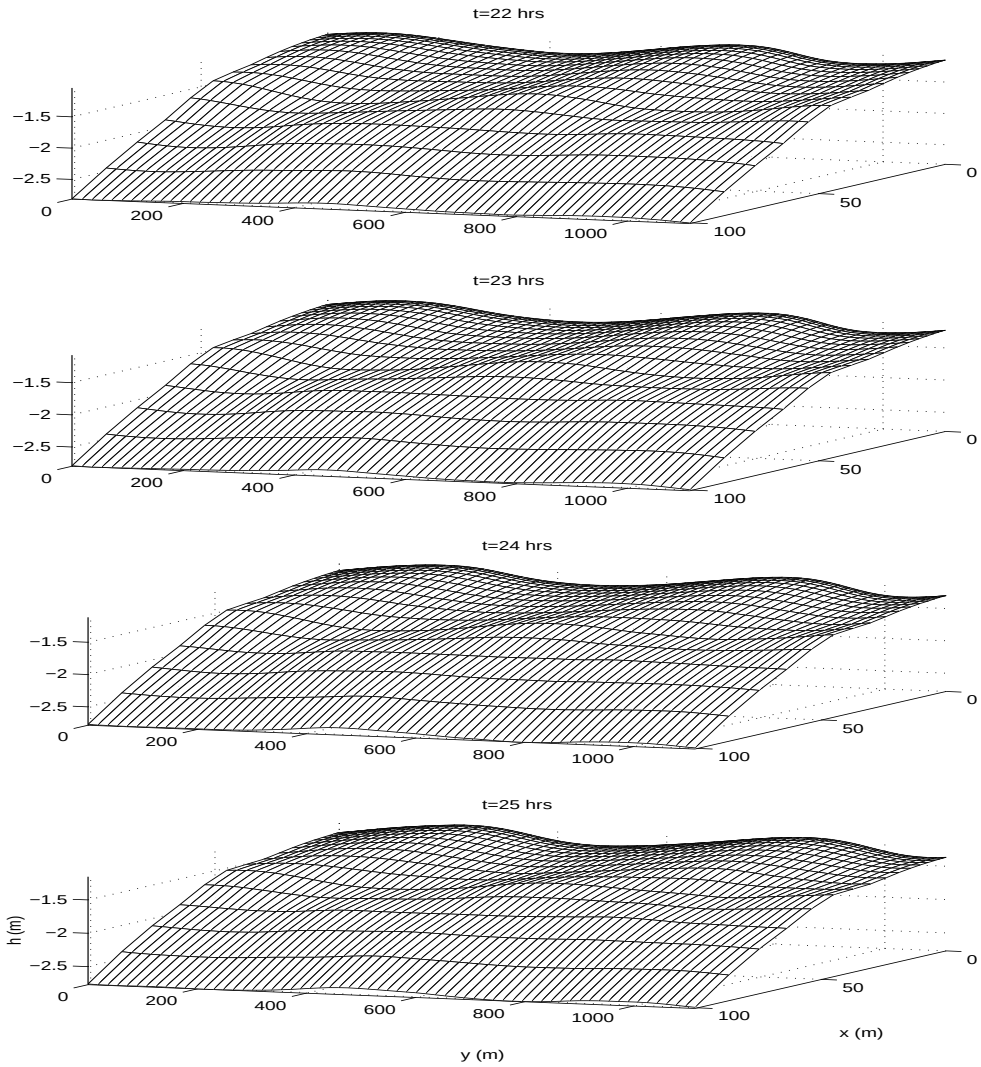

Figure 6.21: 3D snapshots of the topography for $k = 1.14$ with constant forcing terms in the momentum equations. The flow is from left to right.

6.3 Summary

In this chapter preliminary results of the evolution of coastal morphodynamic instabilites have been presented. The results serve as a general guide for future studies while showing the capability of the model.

Two different wave and beach conditions, and within each case two different types of instabilities defined by Falqués *et al.* (1996a, 1996b) have been considered. The first condition is for a beach with a mild slope, low wave height and incident angle. In the second case the beach has a steeper slope and the wave and incident angle are larger. The two types of instabilities are bed-flow instability, in which the bed evolution does not affect the momentum forcing terms, and bed-surf instability where the bed change affects these forcing terms.

In the first case the bed evolves into complicated patterns in which some longshore periodicity is detectable. The growth of the bedforms is very fast and within a very short period shoals form at the shoreline. As these formations start growing out of the water surface the simulation stops. A similar case has been considered where the initial bed instability is placed farther offshore. The results show no significant difference, other than that the resulting bedforms are more organized and that it takes longer for the shoreline shoals to form. When constant mometum forcing terms are considered the bed evolution is a lot more organized and slower. The shoals at the shoreline do not form as fast as in the previous case. Longshore periodic bumps and holes form. The most significant features are the oblique channel-like scour regions extending offshore. The bed evolution in both cases is comparable to field observations and analytical studies (Sonu, 1973; Falqués *et al.*, 1996a).

The second case shows significantly different results. The initial bed instability is quickly spread over the profile. As large cusp-like sand waves form towards the shoreline the bed slope in this region decreases. The sand eroded from this region is deposited offshore to form a slightly wavy bar region, but not as significant as the sand waves formed at the shoreline. The flow field is surprisingly different than the previous cases and it does not directly match the bed evolution. The flow field seems to be rather unaffected by the bed features, although an instability caused by the bedforms is present in the longshore flow. For the case of bed-flow instability the results show almost no difference. The only difference is that the bedforms grow and propagate faster.

From these results it seems that the bed slope plays an important role in the formation of longshore periodic bedforms. This is especially evident in the results for a steeper beach and pronounced wave conditions. Significant sand waves evolve over the region where the bed slope decreases, whereas for the cases with a milder beach slope the bed evolution is significant almost over the entire profile. There are also other factors which were not considered, like the effect of bottom friction or lateral mixing.

It has to be noted that this sediment transport model does not take into account transport due to waves. Cross-shore transport effects can not be modeled accurately with this type of a model. It is possible to study longshore rhythmic bedform evolution and it also seems possible to predict length scales of these bedforms up to a certain accuracy.

Field data specifically focused on rhythmic bedforms is not very common. Most of the

related studies focus more on the planform change sequences and length scales. An accurate quantitative comparison may be therefore difficult to accomplish. Such a comparison would involve the determination of the transport coefficient ν, bottom friction coefficient c_f and also the effects of lateral mixing, which makes it even more difficult. It is possible though to simulate the effects of changing wave conditions on the bed evolution, especially in order to identify bedform change sequences. Considering that waves are a dominant driving force in the coastal zone, a transport model including effects of both currents and waves is necessary.

Chapter 7

SEDIMENT TRANSPORT UNDER WAVES AND CURRENTS

Considering the surf zone, it is obvious that sediment transport occurs due to waves and currents. Besides being the driving force of the currents, waves can cause suspended sediment transport due to their oscillatory motion. The sediment transport equation in the previous chapters considers only the mean currents.

This chapter includes preliminary work on replacing the previous transport equation with a more sophisticated model that considers the effects of both waves and currents as well as bottom slope. Without addressing its accuracy or physical background, we incorporate an energetics type sediment transport equation into the hydrodynamic code (Bailard, 1981; Bailard and Inman, 1981). This model separates transport into bedload and suspended load. The main point to note in using this model is that it is for instantenous near-bed velocity values. The velocities include both mean currents and the oscillatory wave motion. Therefore, the velocity components are divided into a mean and wave part, and the transport equation is time averaged over one wave period. It is further assumed that depth-averaged mean velocities computed by the hydrodynamic code can be used as near-bed velocities.

The terms resulting from the time averaged wave part of the velocities are referred to as velocity moments. Depending on the wave theory used in the hydrodynamic code, these moments can be either directly computed numerically (using high order wave theories), or they can be approximated through empirical relationships and approximations.

The next section outlines the total load transport equation and how it is incorporated into the model including the computation of the velocity moments. A crude undertow formulation is included as well.

Preliminary results for a planar beach are also presented. The effect of the undertow on the beach evolution is addressed. Suggested applications of this extended model are outlined in the last section.

7.1 The Total Load Sediment Transport Equation and Inclusion of Undertow

Bailard (1981) used an energetics based total sediment transport model developed by Bagnold (1966), as a basis for the development of a total load model of time varying sediment transport over a plane beach. The total load transport which consists of bedload and suspended load depends on a velocity-induced component and a downslope acting gravity component.

Separating the total transport into bedload and suspended load components, $\mathbf{q} = \mathbf{q_b} + \mathbf{q_s}$, the transport equation in vectorial form can be written as

$$\mathbf{q} = k_b \left[\mathbf{u}|\mathbf{u}|^2 + \frac{|\mathbf{u}|^3}{\tan\phi} \nabla h \right] + k_s \left[\mathbf{u}|\mathbf{u}|^3 + \frac{\epsilon_s |\mathbf{u}|^5}{w} \nabla h \right] \tag{7.1}$$

where the first term is $\mathbf{q_b}$ and the second term is $\mathbf{q_s}$. In this equation h is the water depth, w is the sediment fall velocity and ϕ is the angle of repose of the sediment. Also, $|\mathbf{u}| = (u^2 + v^2)^{1/2}$, where u and v are the velocity components. The coefficients k_b and k_s are given as

$$\begin{aligned} k_b &= \frac{\rho}{\rho_s - \rho} \frac{c_f \epsilon_b}{\tan\phi} \\ k_s &= \frac{\rho}{\rho_s - \rho} \frac{c_f \epsilon_s}{w} \end{aligned} \tag{7.2}$$

Here ρ and ρ_s are the densities for water and the sediment, respectively. The friction factor is c_f. The coefficients ϵ_b and ϵ_s are bedload and suspended load efficiency factors, which govern the fraction of dissipated energy rate used in sediment transport.

The sediment conservation equation is as follows

$$(1 - n) h_t = \nabla \cdot \mathbf{q} \tag{7.3}$$

where n is the bed porosity.

Since a wave-averaged hydrodynamic code is used, this instantaneous transport model has to be integrated over one wave period. Therefore, first the velocity components are divided into a mean part and a wave-induced part

$$\mathbf{u} = \bar{\mathbf{u}} + \tilde{\mathbf{u}} \tag{7.4}$$

where $\bar{\mathbf{u}}$ is the mean part and $\tilde{\mathbf{u}}$ is the wave-induced part. The mean part results from the wave-averaging process. Note that in the transport equation direct integration of the four terms including $\mathbf{u}$ is not possible since it is necessary to know how $\tilde{\mathbf{u}}$ changes in time.

One approach could be using Stokes wave theory in which the time variation of the wave part $\tilde{\mathbf{u}}$ is explicitly known. In order to obtain velocity skewness terms and higher moments from the integration, a second-order or higher theory has to be used, or no terms will survive the integration over time. With the second-order theory, only the first term $\mathbf{u}|\mathbf{u}|^2$ can be analytically integrated. The other terms have to be computed numerically because the resulting integrals can not be analytically evaluated without certain approximations. Since

Stokes theory is not applicable for shallow water, and considering that we are specifically interested in the surf zone it is very likely that Stokes theory will lead to incorrect velocity moments and therefore incorrect sediment transport rates. This also has been confirmed by preliminary trial simulations with this hydrodynamic code. These results are not shown here.

Another approach that can be used involves approximating the wave-averaged terms in order to separate the velocity moments and use empirical formulations to evaluate them. An exact evaluation of the first term in the transport equation is possible without approximations.

The wave part can be written as

$$\tilde{\mathbf{u}} = \tilde{u_o}(\cos\theta, \sin\theta)$$

where $\tilde{u_o}$ is the oscillatory wave component oriented at the incident wave angle θ to the x-direction. Note that $\tilde{u_o}$ is time and space dependent and $|\tilde{\mathbf{u}}| = |\tilde{u_o}|$. Using this form and representing wave-averaged terms in brackets the following expression can be obtained for the first term

$$\begin{aligned}\langle \mathbf{u}|\mathbf{u}|^2 \rangle &= [\bar{u}(\bar{u}^2 + \bar{v}^2) + \bar{u}\langle \tilde{u_o}^2 \rangle + \langle \tilde{u_o}^3 \rangle \cos\theta + 2\langle \tilde{u_o}^2 \rangle \cos\theta(\bar{u}\cos\theta + \bar{v}\sin\theta)]\hat{i} \\ &\quad + [\bar{v}(\bar{u}^2 + \bar{v}^2) + \bar{v}\langle \tilde{u_o}^2 \rangle + \langle \tilde{u_o}^3 \rangle \sin\theta + 2\langle \tilde{u_o}^2 \rangle \sin\theta(\bar{u}\cos\theta + \bar{v}\sin\theta)]\hat{j}\end{aligned} \tag{7.5}$$

where θ is assumed to be independent of time.

The rest of the terms can be approximated by assuming weak currents or strong currents. A Taylor series expansion can be used as an approximation with the weak-current assumption, $|\bar{\mathbf{u}}| < |\tilde{\mathbf{u}}|$ (Roelving and Stive, 1989)

$$\begin{aligned}\langle |\mathbf{u}|^3 \rangle \nabla h &= [\langle \tilde{u_o}^3 \rangle + 3\langle \tilde{u_o}^2 \rangle(\bar{u}\cos\theta + \bar{v}\sin\theta) + ...](h_x\hat{i} + h_y\hat{j}) \,, \\ \langle \mathbf{u}|\mathbf{u}|^3 \rangle &= [\langle \tilde{u_o}^4 \rangle \cos\theta + \langle \tilde{u_o}^3 \rangle\{\bar{u} + 3\cos\theta(\bar{u}\cos\theta + \bar{v}\sin\theta)\} + ...]\hat{i} \\ &\quad + [\langle \tilde{u_o}^4 \rangle \sin\theta + \langle \tilde{u_o}^3 \rangle\{\bar{v} + 3\sin\theta(\bar{u}\cos\theta + \bar{v}\sin\theta)\} + ...]\hat{j} \,, \\ \langle |\mathbf{u}|^5 \rangle \nabla h &= [\langle \tilde{u_o}^5 \rangle + 5\langle \tilde{u_o}^4 \rangle(\bar{u}\cos\theta + \bar{v}\sin\theta)\frac{15}{2}\langle \tilde{u_o}^3 \rangle(\bar{u}^2\cos^2\theta + \bar{v}^2\sin^2\theta \\ &\quad + 2\bar{u}\bar{v}\sin\theta\cos\theta) + \frac{5}{4}\langle \tilde{u_o}^3(\bar{u}^2 + \bar{v}^2) + ...](h_x\hat{i} + h_y\hat{j})\end{aligned} \tag{7.6}$$

where $(\hat{i}, \hat{j})$ represent unit vectors in the (x, y) directions and $(\bar{u}, \bar{v})$ are the components of the mean velocity. Note also that, $\langle \tilde{u_o} \rangle = 0$. For the second and last term in the transport equation although the bed slope ∇h is time varying, too it is not included in the wave-averaging. Considering that the morphological time scale is larger than the time scale for wave motion (or the hydrodynamic time scale), the bed slope is not affected by this integration.

Assuming now strong currents, $|\tilde{\mathbf{u}}| < |\bar{\mathbf{u}}|$ the following expressions can be obtained

$$\begin{aligned}
\langle|\mathbf{u}|^3\rangle\nabla h &= [\bar{u_o}^3 + \frac{9}{2}\langle\tilde{u_o}^2\rangle((\bar{u}\cos\theta)^2 + (\bar{v}\sin\theta)^2 + \bar{u}\bar{v}\sin 2\theta + \bar{u_o}^2) + ...] \\
&\quad (h_x\hat{i} + h_y\hat{j}) \ , \\
\langle\mathbf{u}|\mathbf{u}|^3\rangle &= [\bar{u_o}^4\cos\theta + \frac{3}{2}\langle\tilde{u_o}^2\rangle\{\bar{u}^2\cos^3\theta + \bar{v}^2\sin^2\theta\cos\theta \\
&\quad +2\bar{u}\bar{v}\sin\theta\cos^2\theta + \bar{u}^2\cos\theta + \bar{u}\bar{v}\sin\theta + \bar{u_o}^2\cos\theta\} + ...]\hat{i} \\
&\quad +[\bar{u_o}^4\sin\theta + \frac{3}{2}\langle\tilde{u_o}^2\rangle\{\bar{u}^2\cos^2\theta\sin\theta + \bar{v}^2\sin^3\theta \\
&\quad +2\bar{u}\bar{v}\sin^2\theta\cos\theta + \bar{v}^2\sin\theta + \bar{u}\bar{v}\cos\theta + \bar{u_o}^2\sin\theta\} + ...]\hat{j} \ , \\
\langle|\mathbf{u}|^5\rangle\nabla h &= [\bar{u_o}^5 + \langle\tilde{u_o}^2\rangle\{\frac{15}{2}(\bar{u}^2\bar{u_o}\cos^2\theta + \bar{v}^2\bar{u}\sin^2\theta + 2\bar{u_o}\bar{u}\bar{v}\sin\theta\cos\theta) \\
&\quad +\frac{5}{2}\bar{u_o}^3\} + ...](h_x\hat{i} + h_y\hat{j})
\end{aligned} \tag{7.7}$$

where $\bar{u_o} = \sqrt{\bar{u}^2 + \bar{v}^2}$. The Taylor series expansions are carried out to the second order for both approximations.

As the next approximation velocity moments higher than 3 are neglected in equation (7.6). For the term $\langle\tilde{u_o}^2\rangle$ we will use Stokes first order theory. This gives

$$\langle\tilde{u_o}^2\rangle = \frac{1}{2}u_m^2 \tag{7.8}$$

where $u_m = \frac{cH}{2h}$. Here c is the wave phase speed, H is the wave height and h is the water depth.

For the velocity skewness $\langle\tilde{u_o}^3\rangle$ an empirical expression based on the study by Doering and Bowen (1995) is used

$$\langle\tilde{u_o}^3\rangle = [0.8 + 0.62\log_{10}(U_r)]\,cos\left(\left[\tanh\left(\frac{0.73}{U_r}\right) - 1\right]\frac{\pi}{2}\right) \tag{7.9}$$

where U_r is the Ursell number given as

$$U_r = \frac{3}{4}\frac{ak}{(kh)^3} \tag{7.10}$$

Here a is the wave amplitude and k is the wavenumber.

The empirical skewness equation is based on the bispectral analysis performed on field data taken at four different beaches. From these measurements $U_r \approx 0.03 - 10$, so the corresponding velocity skewness range is limited by these values.

In order to account for a more realistic cross-shore transport process, as a first approximation an average undertow velocity has been included only in the transport equation.

Considering short waves, the volume flux due to the wave consists of a Stokes drift part $\mathbf{Q_s}$ and a part due to the wave roller $\mathbf{Q_w}$. The wave roller is the foamy section located at the front face of a breaking wave.

Using linear waves the part due to Stokes drift can be represented as

$$\mathbf{Q_s} = \frac{gH_{rms}}{8c}(\cos\theta, \sin\theta) \tag{7.11}$$

where g is the gravitational acceleration, H_{rms} is the rms wave height and c is the phase speed of the waves.

The flux due to the roller of one wave can be written as

$$\mathbf{Q_w} = Af(\cos\theta, \sin\theta) \tag{7.12}$$

A is the roller area and f is the frequency associated with the wave. The expression for the roller area given by Engelund (1981) is used

$$A = \frac{(BH_b)^3}{4h\tan\sigma} \tag{7.13}$$

where B was previously defined in the dissipation term due to wave breaking (equation 6.4), H_b is the wave height at breaking and σ is the angle of the wave-roller interface. In a similar manner as it was done for the dissipation term due to wave breaking, H_b can be integrated through the probability density distribution for random waves. Following this approach Lippmann *et al.* (1996) obtained an expression for this integral

$$\langle H_b^3 \rangle = \frac{3\sqrt{\pi}}{4(\gamma h)^2} H_{rms}^5 \left(1 - \frac{1}{\left(1 + \left(\frac{H_{rms}}{\gamma h}\right)^2\right)^{5/2}} \right) \tag{7.14}$$

The volume flux then can be written as

$$\mathbf{Q_w} = \frac{f_p B^3 \langle H_b^3 \rangle}{4h\tan\sigma}(\cos\theta, \sin\theta) \tag{7.15}$$

The undertow is due to this volume flux which returns from the shoreline in the cross-shore direction and imposes additional discharge in the longshore direction. Dividing the total flux by the local water depth gives an average undertow expression

$$\mathbf{u_{tow}} = -\frac{\mathbf{Q_s} + \mathbf{Q_w}}{h} = -\frac{\mathbf{Q}}{h} \tag{7.16}$$

An accurate approach would require the inclusion of this undertow expression in the velocity components within the whole model, but as a preliminary approach it is only included in the velocities entering the transport equation.

7.2 Preliminary Results

As a preliminary simulation the model has been applied to a plane sloping beach. The main purpose is to observe how the beach profile responds to the wave and current field when both effects are considered in sediment transport.

The beach slope is $m = 0.05$ with a $h_o = 0.05m$ deep wall located at the shoreline. The cross-shore distance of the domain is $L_x = 410m$. The longshore domain width is arbitrarily set to $L_y = 42m$. Since the process is confined to the cross-shore, no longshore changes occur and the value of L_y does not affect the results. Due to the same reason only 4 collocation points in the longshore direction and 32 in the cross-shore direction are used. The offshore wave height is $H_o = 2.4m$ and the wave period is $T = 15s$. The waves travel with a shore normal angle. The bottom friction factor is $c_f = 0.003$ and lateral momentum mixing has been neglected.

The flow field developed in about an hour and sediment transport was activated after that. The coefficients in the transport equation are chosen according to Bailard (1981), Bailard and Inman (1981), and Roelvink and Stive (1989). The coefficients are as follows: $\phi = 32^o$, $\rho_s = 2650kg/m^3$, $\rho = 1000kg/m^3$, $n = 0.4$, $w = 0.01m/s$, $\epsilon_b = 0.2$ and $\epsilon_s = 0.025$.

The coefficients B, γ and σ which govern the wave energy dissipation due to breaking and the undertow are chosen from the values given by Thornton and Guza (1983) and Lippmann *et al.* (1996). These values are adjusted according to field data. For this case they are; $B = 0.78$, $\gamma = 0.45$ and $\sigma = 10^o$.

The beach slope and wave conditions are chosen arbitrarily, but still they can be considered as representative of real field conditions, in particular based on the above mentioned studies.

The wave and beach conditions produce a significant offshore transport, where a major scour forms right at the shoreline wall and the sand transported offshore forms a bar around the point of wave breaking. The erosion at the shoreline wall is very severe and causes unrealistic steep slopes and water depths. This situation is shown in Figure 7.1. Within a few hours this situation causes numerical problems in the model (i.e. Courant condition violation). Therefore the shoreline wall boundary condition of zero cross-shore transport rate, $q_x = 0$ has been changed to zero cross-shore transport gradient, $\partial q_x / \partial x = 0$. This condition prevents the unrealistic scour to form at the shoreline, but it also means that every time step a certain amount of sand volume is added to the system at that point. This sand is eventually transported and deposited to the offshore.

A simulation for 25 hours has been obtained using this boundary condition. Snapshots of the beach profile every $5.5hrs$ are shown in Figure 7.2. A significant amount of offshore transport is happening where the profile is eroded towards the shoreline and all this sediment is deposited offshore forming a bar around the point of wave breaking. After 12 hours erosion almost stops as the growth and offshore movement of the bar continues. This is due to the shoreline boundary condition mentioned above. The profile in fact has almost reached equilibrium in 12 hours, but the shoreline boundary condition imposes additional sediment volume into the domain which is causing the continuing bar growth.

In Figure 7.3, cross-shore profiles of the wave height, undertow, sediment transport rate and the topography are shown at 25 hours. Studying this figure the offshore bar is obviously forming around the point where wave breaking happens. The average undertow increases as the waves reach their maximum value at breaking, and after that as the depth decreases it continues increasing with its peak value at the shoreline. Except for the high values closer to the shoreline, the cross-shore magnitudes of the undertow are within average undertow

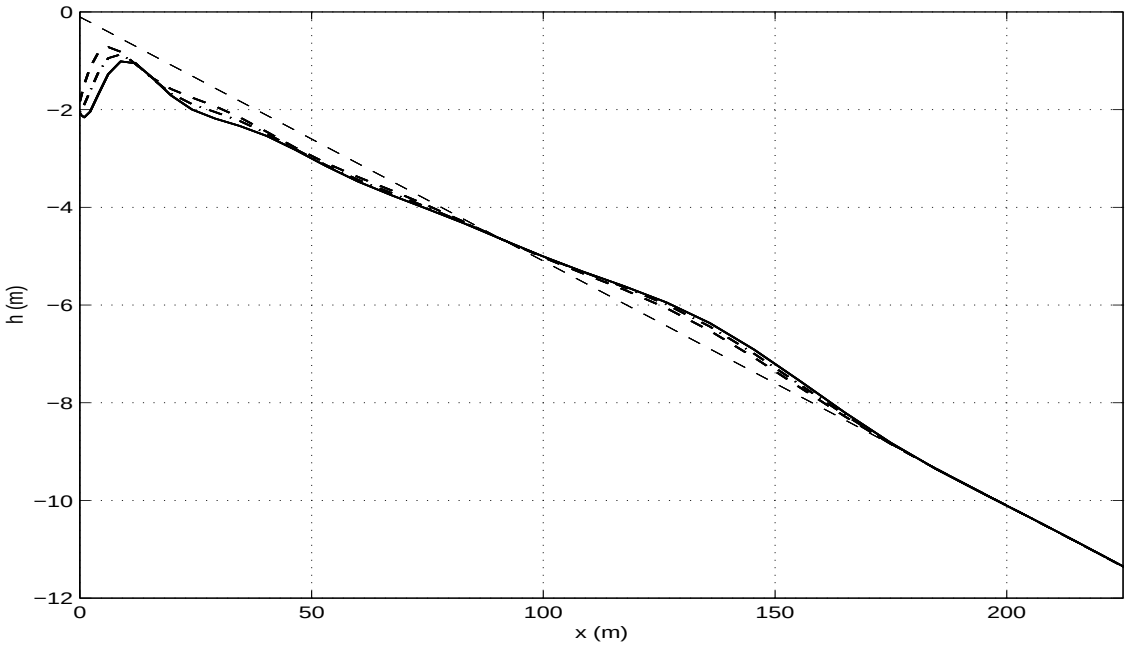

Figure 7.1: Snapshots of cross-shore beach profile with $q_x = 0$ boundary condition at shoreline. Thin dashed line: initial profile.

values observed under field conditions based on the study by Faria *et al.* (2000). With shore normal approaching waves the only effective cross-shore flow is due to the offshore directed undertow. Therefore the resulting sediment transport is also offshore directed, which can be seen in Figure 7.3(c) as positive values. Note that positive values are directed offshore.

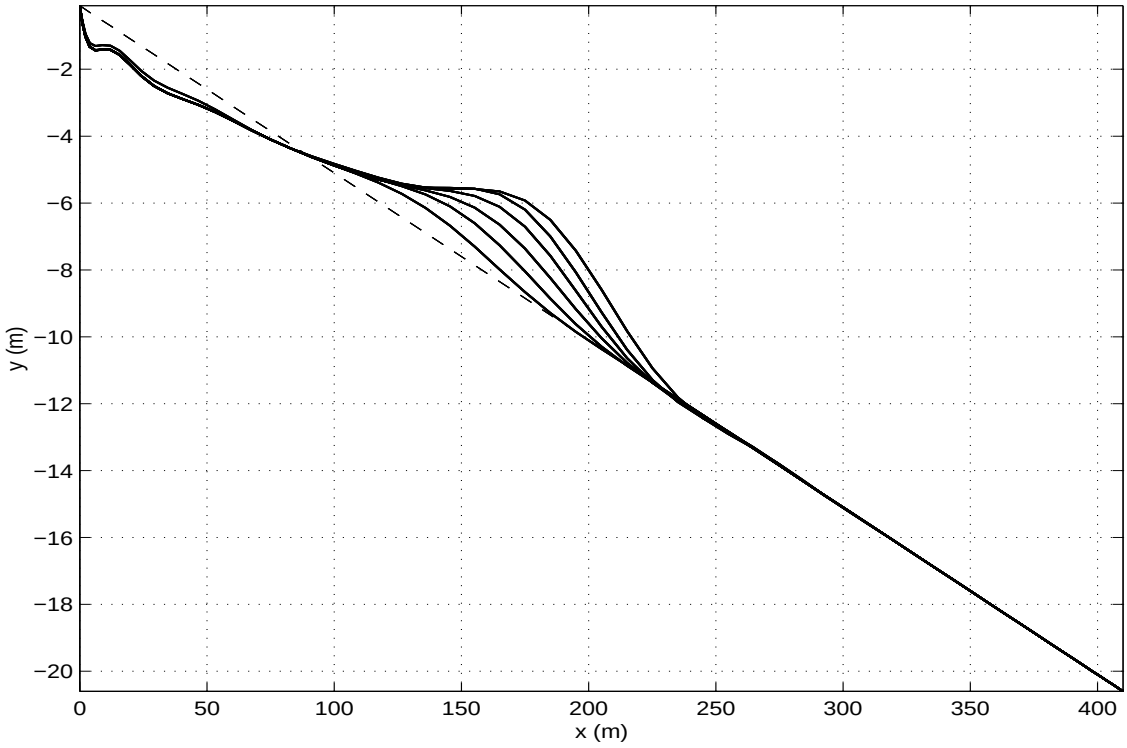

Figure 7.2: Snapshots of cross-shore beach profile with $\partial q_x/\partial x = 0$ boundary condition at shoreline. Solid lines: profile at every $5.5hrs$, dashed line: initial profile.

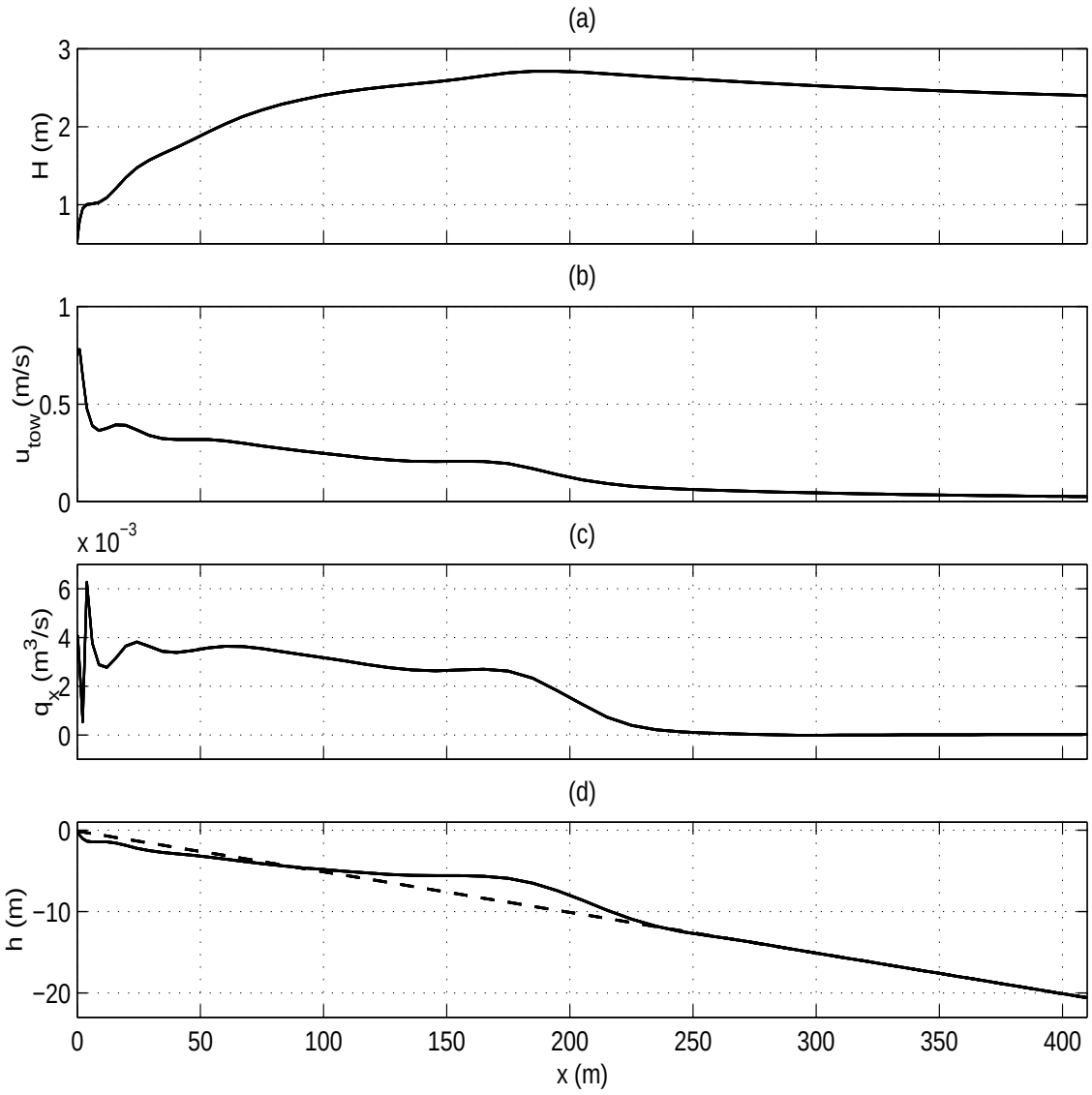

Figure 7.3: Cross-shore profiles at $t = 25hrs$. (a) Wave height, (b) Undertow, (c) Sediment transport rate, (d) Topography.

7.3 Further Applications

Obviously, the total load transport equation has to be tested for more cases. The accuracy of the undertow formulation, the weak- and strong-current approximations and how the bed evolution will be affected by these approximations especially when perturbations are introduced are some of the points which need further investigation.

For the simple case presented here as a preliminary result, the improved transport model seems promising. It is able to produce the classical bar-trough formation under breaking wave and strong undertow conditions. The boundary condition at the shoreline can be considered as one shortcoming of the model. The case with the more realistic condition of zero cross-shore transport at the shoreline wall produces very high offshore transport rates majorly due to the very high undertow values at those points. This causes severe erosion towards the shoreline. The undertow consists of the Stokes drift and the breaking wave roller effects. The formulation for the Stokes drift part is based on linear wave theory which for shallow water may not be accurate enough. Since towards the shoreline the water depth decreases significantly, the discharge computed form this formulation divided by small depths produces extremely high values of undertow velocities. Field and laboratory measurements specifically focused on undertow also indicate that towards the shore undertow magnitudes usually decrease (Roelvink and Stive, 1989; Faria *et al.*, 2000). With the present undertow formulation it may not be possible to obtain realistic untertow values for shallow water depths.

It should also be noted that the undertow values only affect the mean currents in the transport equation, whereas a complete approach would require their inclusion in the whole model. When wave-current interaction is considered as well, it can be expected that with both these effects the resulting flow and wave fields would be significantly altered. With wave-current interaction, besides depth-limited wave breaking current-limited breaking would be affective, too. This causes a variation of the breaking line and in turn an additional variation in the radiation stress terms. Considering all these effects may produce more realistic transport rates.

The test case presented is a one-dimensional problem. No changes in the longshore direction occur. Increasing the longshore domain length with the number of grid points can produce different results. Preliminary simulations carried out for the same wave and beach conditions, only with a longer longshore domain length and more collocation points show that the same bar-trough configuration may not arise. The results which are not shown here, show that a rather complicated bed evolution happens where a series of longshore bumps and holes form. These form very close to the shoreline and since with normally incident waves a significant longshore flow does not develop, they do not propagate in the longshore direction but spread towards the offshore. It is difficult to tell how periodic these formations are in the longshore direction. The resulting bed resembles cases where a longshore continuous bar is destroyed by the fornmation of channel-like scours similar to rip channels. At this point we are not certain how much of this inherent instability in the system is due to numerical reasons and what portion of it has some physical meaning. Considering that the same conditions are used in previous simpler simulations and that the number of grid points is large enough to assure spatial accuracy, it may be difficult to associate this rather chaotic bed evolution

with numerical effects.

Many field studies focus on two- and three-dimensional bar behaviour under varying wave conditions or specifically on the formation of certain bed features like rip channels. Two recent studies by Brander (1999) and Ruessink *et al.* (2000) are of this type. One of the important goals of such studies is to determine the associated morphodynamic variability of beaches as a sequence. Wright and Short (1984) were able to form a sequence of beach plan and profile configurations based on observations and measurements obtained over a period of three years. A more recent study based on video imaging data collection by Lippmann and Holman (1990) shows that the sequence developed by Wright and Short can be extended with additional intermadiate beach configurations. Both of these sequences are based on the formation of a bar, its longshore variability and cross-shore movement. Although detailed bathymetric data is not avialable from these studies, length and time scales of the morphodynamic processes can be used in simulations for changing wave conditions in order to investigate if similar beach sequences can be modelled.

It is necessary to test the preformance of the present model first with certain cases before carrying out simulations for changing wave conditions. The inclusion of wave-current interaction is essential, especialy if wave conditions are significant. The accuracy of the weak- and strong-current approximations has to tested. A case for obliquely incident waves where strong alongshore currents develop can be used as a test case. It is important to keep the longshore domain length long enough to ensure two-dimensionality. The number of grid points has to be large enough for spatial accuracy. A similar test case can be carried out for an initially barred beach.

In order to investigate the evolution of bed instabilities and longshore rhythmic bedforms under waves and currents, cases similar to the ones presented in Chapter 6 can be used. One thing to note in this case is that the same most unstable wavenumber used previously can not be used now. Since the sediment transport equation is different the resulting wavenumber-frequency relations most probably will be different as well. The onset of the growth of bed instabilites and their evolution is governed by the transport equation used, so it may be possible that an unstable condition in Chapter 6 may not be unstable with the extended transport model. In order to follow an accurate approach based on analytical results, a similar stability analysis perfomed by Falqués *et al.* with the present transport model has to be carried out. Considering that this analysis is mathematically very involved even with a simpler transport equation, such an analysis is obviously very difficult.

Chapter 8

CONCLUSIONS AND FUTURE WORK

A hydrodynamic model based on the depth- and wave-averaged shallow water equations was extended with sediment transport capability to study the evolution of bed perturbations as rhythmic bedforms.

Two different cases were considered. The model was first applied to a rectangular channel geometry with impermeable and nonerodible side walls. For this case a standard linear stability analysis was carried out for the morphodynamic instabilities based on the study by Schielen *et al.* (1993).

The stability analysis was first performed for an one-dimensional channel. The results showed that instability is not possible, therefore growth of bed instabilities can not happen. In order for instability to happen a phase difference between the bedforms and the velocity or the water surface is necessary (Kennedy, 1963). It was also found that lifting the rigid-lid and quasi-steady assumptions in the analysis did not result in significant changes in terms of the stability of the system. The same analysis was carried out for a two-dimensional channel, resulting in unstable bed perturbations for certain wavenumber ranges and combinations of parameters involved in the analysis. The results consist of wavenumber-frequency relations for the bed perturbations. The effect of the parameters on the dispersion curves were investigated as well. Three parameters were investigated; the bottom friction factor, the channel depth-to-width ratio and the velocity power in the transport equation. Increasing the magnitudes of these parameters had more-or-less the same effect on the results. An increase of the parameters was associated with an increase of the unstable wavenumber range and values.

The sediment transport routine was first tested with a basic case where a cross-channel slope and a constant along-channel flow were introduced. The channel cross-section was seen to reach equilibrium in time. For the rest of the numerical simulations the unstable wavenumbers obtained were used to initially perturb the channel bed. For a fixed depth-to-width ratio, friction factor, transport coefficient and velocity power the most unstable wavenumber was used and the effect of different channel lengths was investigated. Simulations for an unstable wavenumber slightly larger and smaller than the maximum one were also carried out.

It was seen that the initial bed perturbation evolved into a pattern referred to as alternate bars. This type of bedforms is commonly observed in alluvial channels and laboratory flume experiments with stabilized side walls. This corresponds to early stages of channel meandering. As this pattern formed, the bed perturbations which can be considered as sand waves attained a very steep wave front, similar to a shock wave form. Depending on the propagation speed of the sand waves and the steepness of the wave front, fluctuations formed right before and after the wave front. These were detected as separating and pairing depth contours. We are currently uncertain on the physical significance of these fluctuations, or if any numerical reasons are causing them to form.

Bedforms in a longer channel evolve more freely and can propagate with higher speeds than predicted by the linear stability analysis. Contour pairing and separation also happens more often and faster. The fluctuations around the wave front, mentioned above, form in each case independent of the channel length. The corresponding flow field which consists of a meandering along-channel stream can gain more strength in its meandering nature for longer channels.

For unstable wavenumbers higher and lower than the maximum, the general alternate bar pattern formed in each case. For the larger wavenumber the resulting bar pattern was smoother than the previous results. More fluctuating depth contours happened for a longer channel with the same wavenumber. Spit-like features developed at high sections of the bars which were formed as part of separating contours when the smaller wavenumber was used. The growth and propagation predicted by the stability analysis matched the numarical results within acceptable limits, especially when the channel length was equal to one perturbation wave length. The propagation speeds of the bedforms were determined by a lag-correlation method from the simulations. Considering nonlinearities present in the system, rather than being a constant value as predicted by the linear stability analysis, the propagation speeds changed as the bed evolved.

For very small and very large values of the friction factor c_f, the bed instabilities may evolve into different patterns and the linear stability analysis may be applicable only to a certain extend. Two different friction factor values were tested. The flow field for smaller c_f values has a less energetic nature, so the stream is less meandering. For larger c_f values the meandering flow field was more pronounced. For a larger value of c_f, although the stability analysis predicted growth, the bed forms reached equilibrium within a period of 10 hours and did not resemble the alternate bar pattern as before.

The velocity power b in the transport equation seems to be critical in the formation of alternate bars. As shown in Chapter 3, for $b = 2$ and $k = 1.05$ growth of bed instabilities did not happen. The numerical results confirm that the bedforms decay in time, but the same alternate bar pattern did not form for this case. For $b = 4$ the resulting patterns were very similar to the previous results.

Two different initial bed perturbation forms were tested. The effect of including higher harmonics in the initial bed perturbation was in the form of significant deformations of the bar structure until the final configuration consisting of the same alternate bar pattern was attained. Including one wavelength plus half of one wavelength in the initial perturbation did not have a significant impact. A similar alternate bar pattern formed, this time with a larger sand wave followed by a smaller one.

It was possible to simulate alternate bar patterns very close to the pattern observed in the experimental study carried out by Uchijima (1990). The bar deformation observed at low flow was not predicted by the model. Bed patterns qualitatively similar to observations and experimental results were obtained, but the bar deformation obviously involves other mechanisms which were not strong enough or not present in our simulations. More accurate comparisons require the appropriate determination of ν and c_f, or a more sophisticated transport model which considers effects like suspended sediment load or grain size distribution. The present model is very sensitive to very low flow depths due to its numerical scheme. At very low depths maintaining spatial accuracy with a sufficient number of grid points requires a very small time step which in turn results in extended simulation periods making long time bed evolution simulations impractical.

A further improvement for the channel cases can be made by replacing the wall boundary conditions with moving boundaries. With the correct implementation of this boundary condition the side walls can be sloped and can be allowed to erode or accrete. In this case the model should be modified such that it can handle accretional regions where small islands or shoals form. With a moving boundary and sediment transport happening, the channel should eventually start to meander which means that the sides of the channel will significantly erode and accrete.

The second geometry used in the simulations was a planar beach. For this case wavenumber-frequency curves obtained by Falqués *et al.* (1996a, 1996b) were used to determine the initial bottom perturbation.

Two wave and beach conditions were considered, and within each case two different instability types. The first case was for a mild sloping beach with low wave height and incident wave angle. The second one was for a steep beach with higher wave height and incident angle values. The two instability types were described in Chapter 2 according to the definitions by Falqués *et al.* (1996a, 1996b). They consist of bed-flow instability where the bed instabilities do not change the momentum forcing terms, and bed-surf instability where the forcing terms are affected by the changing bed.

In the first case the bed evolved into a complicated pattern of bumps and channel-like holes in which some longshore periodicity was detectable. The growth of the bedforms was very fast and within a very short period shoals formed at the shoreline, eventually growing out of the water surface. A similar case was considered where the initial bed instability is placed farther offshore. The results show no significant difference, other than that the resulting bedforms are more organized and that it takes longer for the shoreline shoals to form. The flow field in both cases matches the bed evolution. A meandering alongshore flow forms where strong vorticies emerge over the shoals. The meandering flow becomes more energetic with increasing vorticity magnitudes when the initial bed perturbation is placed closer to the shore, but it shows some decrease for the other case.

The bed pattern for these two cases is comparable to laboratory observations of the development of skewed rhythmic topography under oblique waves as described by Sonu (1973). The alongshore length scales of the bedforms are very close to the values observed at Seagrove, Florida (Sonu, 1973). Although in the field this evolution happens over a period of several days and the wave angle changes from oblique to shore normal, the simulated channel-like scour and bump regions are similar to the observed bed evolution.

When constant momentum forcing terms were considered (bed-flow instability) the bed evolution was more organized and slower. The shoals at the shoreline did not form as fast as in the previous cases. The overall trend of bed evolution was in the form of cross-shore spreading as oblique bars and channel-like scours formed. Longshore periodicity was easily recognizable. The flow field consisted of a longshore meandering flow where velocity vectors converge over holes and diverge over bumps. Vorticies as in the previous examples did not form.

The second case for a steep beach with higher waves and incident angles shows significantly different results. The initial bed instability was again quickly spread over the profile. Large cusp-like sand waves formed towards the shoreline. The bed slope in this region decreased significantly due to erosion and the sand eroded from this section was majorly deposited offshore to form a slightly wavy bar region, but not as significant as the sand waves at the shoreline. The flow field was surprisingly different than the previous cases and it did not directly match the bed evolution. The overall flow field rather unaffected by the bed features still included an instability in the longshore current, obviously caused by the bedforms. For the case of bed-flow instability the results show almost no difference. The only difference was that the bedforms grow and propagate faster.

The bed slope seemed to play an important role in the formation of longshore periodic bedforms. This was especially evident in the results for a steeper beach and pronounced wave conditions. Significant sand waves evolved over the region where the bed slope decreased, whereas for the cases with a milder beach slope longshore periodic features were significant almost over the entire profile.

The effects of the longshore domain length, the friction factor, the form of the initial bed perturbation and lateral mixing can be investigated for future work. Similar to the channel simulations choosing a longer longshore domain and including higher or lower harmonics in the bed perturbation may cause different patterns to evolve. In all of the previous simulations the bed was initially perturbed. Another approach can be investigating the effects of an initially perturbed flow field on the bed evolution. In the previous simulations it is obvious that instabilities in the flow field arose due to the bed perturbations, but whether or not a perturbation in the flow field would have a similar effect on the bottom is not obvious.

The effects of the moving shoreline were not investigated. The condition for sediment transport at the moving shoreline boundary is crucial since it may cause problems if bed features eventually start growing out of the water. As mentioned in earlier chapters, as a preliminary trial the same condition of zero transport at the moving shoreline can be imposed to investigate its effect on the bed evolution.

It has to be noted that this sediment transport model does not take into account transport due to waves, therefore cross-shore transport effects can not be modeled accurately. It is possible to study longshore rhythmic bedform evolution and it also seems possible to predict length scales of the bedforms up to a certain accuracy, but an accurate quantitative comparison with field data may be difficult to accomplish. First of all detailed data specifically focused on rhythmic bedforms may be hard to find. Such a comparison would also involve the determination of the transport coefficient ν, bottom friction coefficient c_f and also the effects of lateral mixing, which makes it even more difficult. Considering that waves are a dominant driving force in the coastal zone, a transport model including effects of both

currents and waves is necessary to model beach changes.

An extended sediment transport model based on the total transport load consisting of bedload and suspended load was used to improve the model (Bailard, 1981; Bailard and Inman, 1981). This type of a transport model is more suitable for the coastal region. It may be possible to study beach configuration changes under different wave conditions. These may include changes from two-dimensional configurations where cross-shore equlibriation is pronounced to more three-dimensional ones like the evolution of rhythmic bedforms, and vice versa. Several field studies have focused specifically on beach change sequences and the transformation of longshore uniform beaches to more complicated 3D configurations (Wright and Short, 1984; Lippmann and Holman, 1990; Brander, 1999; and Ruessink *et al.*).

The incorporation of this transport equation into the model required certain approximations, like the strong- and weak-current approximations to evaluate the terms with velocity moments arising due to the wave-averaging process. The evaluation of the second moment and the skewness were achieved by Stokes first-order theory and an empirical equation obtained by Doering and Bowen (1995), respectively. An average undertow formulation was used, too, but only in the transport equation.

A test case of this extended model was run for a planar beach. The region between the shoreline and point of breaking waves eroded as the sand was transported offshore to form a bar under the wave breaking region. This bar-trough formation under breaking waves is commonly observed in the field.

Further simulations to address the capability of the extended model are essential. With the undertow formulation included only in the transport equation the results seem promising. In order to account for the undertow in the whole system, this formulation has to be included in the hydrodynamic model as well. Another point about the undertow is that the cross-shore magnitudes increase towards the shoreline, which cause extreme offshore transport leading to very steep scour regions at the shore. As an initial remedy for this problem the zero cross-shore sediment transport condition was replaced by zero cross-shore transport gradient. For further applications the basic average undertow formulation may have to be replaced with a more accurate one, especially towards the shore where water depth decreases significantly.

The weak- and strong-current approximations as well as the equations for the velocity moments have to be tested, too. The effect of a strong-current situation can be investigated by allowing obliquely incident waves to approach a plane beach. Longshore periodic bed patterns can be studied by initially perturbing the bottom, similar to the simulations in Chapter 6.

Following the results by Lippmann and Holman (1990), beach change sequences under changing wave conditions can be studied by first allowing a bar to form on a planar reflective beach, similar to the preliminary test case mentioned above. This topography can then be used as input to further simulate the bed evolution by changing the wave incidence accordingly. According to the classification scheme by Lippmann and Holman (1990), the longshore uniform bar eventually evolves into a non-rhythmic, attached bar and later to a rhythmic one.

In order to accurately simulate the effects of both currents and waves, the inclusion of wave-current interaction is essential. Presently the model considers wave-current interaction

only up to the point when the wave height inside the domain is fully developed.

The bed instabilities and the simulated bed evolution are obviously sensitive to the transport equation. This study focused on the evolution of coupled hydrodynamic and bed instabilities rather than directly addressing the accuracy of the transport equations used. For more accurate comparisons the determination of the parameters in the transport equations is crucial. Due to the complex numerical computations involved in the model, the simulations may become impractical considering computational time and power, especially when the changing bottom coupled to the hydrodynamic part is computed at every time step. For certain situations the changing bottom could be computed only at specified times within the simulation. The bottom change can be computed at time steps matching the morphological time scale, which can be approximated depending on the transport equation used. Considering that complex interactions between waves, currents and the bottom can exist in very energetic situations where the morphological time step is small, it still may be necessary to calculate the bed level at every time step of the simulation.

Bibliography

Allen, J. S., Newberger, P. A., and Holman, R. A. (1996). Nonlinear shear instabilities of alongshore currents on plane beaches. *J. Fluid Mech.*, **310**, 181–312.

Anderson, A. G., Parker, G., and Wood, A. (1975). The flow and stability characteristics of alluvial channels. Technical Report 161, St. Anthony Falls Hydraulic Laboratory, University of Minnesota.

Bagnold, R. A. (1966). An approach to the sediment transport problem from general physics. *U.S. Geol. Surv. Prof. Pap.*, **422-1**.

Bailard, J. A. (1981). An energetics total load sediment transport model for a plane sloping beach. *J. Geophys. Res.*, **86**, 10938–10954.

Bailard, J. A. and Inman, D. L. (1981). An energetics model for a plane sloping beach: Local transport. *J. Geophys. Res.*, **86**, 2035–2043.

Battjes, J. (1975). Modeling of turbulence in the surf zone. *Proc. Symposium on Modeling Techniques*. San Francisco, 1050-1061.

Blondeaux, P. (2001). Mechanics of coastal forms. *Annu. Rev. Fluid Mech.*, **33**, 339–370.

Bowen, A. J. and Holman, R. A. (1989). Shear instabilities of the mean longshore current. 1. theory. *J. Geophys. Res*, **94**, 18023–18030.

Brander, R. W. (1999). Field observations on the morphodynamic evolution of a low-energy rip current system. *Marine Geology*, **157**, 199–217.

Canuto, C., Hussaini, M. Y., Quarteroni, A., and Zang, T. A. (1987). *Spectral Methods in Fluid Dynamics*. Springer-Verlag, New York, N.Y. 567 pp.

Chang, H. Y., Simons, D. B., and Woolhiser, D. A. (1971). Flume experiments on alternate bar formation. *Journal of Waterway, Port, Coastal and Ocean Engineering*, **97**(WW1), 155–165.

Christensen, E. D., Deigaard, R., and Fredsøe, J. (1994). Sea bed stability on a long straight coast. In *Proc. 24th Intl. Conf. Coastal Engineering*, Kobe, 1865-1879.

Colombini, M., Seminara, G., and Tubino, M. (1987). Finite-amplitude alternate bars. *J. Fluid Mech.*, **181**, 213–232.

Deigaard, R., Christensen, E. D., Damgaard, J. S., and Fredsøe, J. (1994). Numerical simulation of finite amplitude shear waves and sediment transport. In *Proc. 24th Intl. Conf. Coastal Engineering*, Kobe, 1919-1933.

Deigaard, R., Drønen, N., Fredsøe, J., Jensen, J. H., and Jørgensen, M. P. (1999). A morphological stability analysis for a long straight barred coast. *Coastal Engineering*, **36**, 171–195.

Doering, J. C. and Bowen, A. J. (1995). Parametrization of orbital velocity asymmetries of shoaling and breaking waves using bispectral analysis. *Coastal Engineering*, **26**, 15–33.

Engelund, F. (1981). A simple theory of weak hydraulic jumps. Technical Report No.54, Institute of Hydrodynamics and Hydraulic Engineering, ISVA, Technical University Denmark.

Falqués, A. and Iranzo, V. (1994). Numerical simulation of vorticity waves in the nearshore. *J. Geophys. Res.*, **99**, 825–841.

Falqués, A., Montoto, A., and Iranzo, V. (1996a). Bed-flow instability of the longshore current. *Continental Shelf Res.*, **16**, 1927–1964.

Falqués, A., Montoto, A., and Iranzo, V. (1996b). Coastal morphodynamic instabilities. In *Proc. 25th Intl. Conf. Coastal Engineering*, Orlando, 3560-3573.

Falqués, A., Calverte, D., Swart, H. E. D., and Dodd, N. (1998). Morphodynamics of shoreface-connected ridges. In *Proc. 26th Intl. Conf. Coastal Engineering*, Copenhagen, 2851-2864.

Falqués, A., Coco, G., and Huntley, D. A. (2000). A mechanism for the generation of wave-driven rhythmic patterns in the surf zone. *J. Geophys. Res.*, **105**, 24071–24087.

Faria, A. F. G., Thornton, E. B., Lippmann, T. C., and Stanton, T. P. (2000). Undertow over a barred beach. *J. Geophys. Res.*, **105**, 16999–17010.

Fredsøe, J. (1978). Meandering and braiding of rivers. *J. Fluid Mech.*, **84**, 609–624.

Hulscher, S. J. M. H. (1996). Tidal-induced large-scale regular bed form patterns in a three-dimensional shallow water model. *J. Geophys. Res.*, **101**, 20727–20744.

Kennedy, J. F. (1963). The mechanics of dunes and antidunes in erodible-bed channels. *J. Fluid Mech.*, **16**, 521–544.

Komarova, N. L. and Hulscher, S. J. M. H. (2000). Linear instability mechanisms for sand wave formation. *J. Fluid Mech.*, **413**, 219–246.

Lippmann, T. C. and Holman, R. A. (1990). The spatial and temporal variability of sand bar morphology. *J. Geophys. Res.*, **95**, 11575–11590.

Lippmann, T. C., Brookins, A. H., and Thornton, E. B. (1996). Wave energy transformation on natural beaches. *Coastal Engineering*, **27**, 1–20.

Longuet-Higgins, M. S. and Stewart, R. W. (1964). Radiation stress in water waves, a physical discussion with application. *Deep Sea Res.*, **11**, 529–563.

Oltman-Shay, J., Howd, P. A., and Birkemeier, W. A. (1989). Shear instabilities of the mean longshore current. 2. field observations. *J. Geophys. Res.*, **94**, 18031–18042.

Özkan-Haller, H. T. (1997). *Nonlinear evolution of shear instabilities of the longshore current*. Ph.D. thesis, University of Delaware. 268 pp.

Özkan-Haller, H. T. and Kirby, J. T. (1997). A Fourier-Chebyshev collocation method for the shallow water equations including shoreline runup. *Appl. Ocean Res.*, (19), 21–34.

Özkan-Haller, H. T. and Kirby, J. T. (1999). Nonlinear evolution of shear instabilities of the longshore current: A comparison of observations and computations. *J. Geophys. Res.*, **104**, 25953–25984.

Parker, G. (1976). On the cause and characteristic scales of meandering and braiding in rivers. *J. Fluid Mech.*, **76**, 457–480.

Phillips, O. M. (1977). *The dynamics of the upper ocean*. Cambridge University Press. 336 pp.

Putrevu, U. and Svendsen, I. A. (1992). Shear instability of longshore currents: A numerical study. *J. Geophys. Res.*, **97**, 7283–7303.

Putrevu, U. and Svendsen, I. A. (1999). Three-dimensional dispersion of momentum in wave-induced nearshore currents. *Eur. J. Mech. B/Fluids*, **18**, 409–427.

Roelvink, J. A. and Stive, M. J. F. (1989). Bar-generating cross-shore flow mechanisms on a beach. *J. Geophys. Res.*, **94**, 4785–4800.

Ruessink, B. G., van Enckevort, I. M. J., Kingston, K. S., and Davidson, M. A. (2000). Analysis of observed two- and three-dimensonal nearshore bar behaviour. *Marine Geology*, **169**, 161–183.

Schielen, R., Doelman, A., and Swart, H. E. D. (1993). On the nonlinear dynamics of free bars in straight channels. *J. Fluid Mech.*, **252**, 325–356.

Schumm, S. A. and Khan, H. R. (1972). Experimental study of channel patterns. *Geological Soc. Am. Bull.*, **83**, 1755–1770.

Sonu, C. J. (1972). Field observation of nearshore circulation and meandering currents. *J. Geophys. Res.*, **77**, 3232–3247.

Sonu, C. J. (1973). Three-dimensional beach changes. *J. Geology*, **81**, 42–64.

Svendsen, I. A. and Putrevu, U. (1994). Nearshore mixing and dispersion. *Proc. Roy. Soc. Lond. A*, **445**, 561–576.

Takebayashi, H., Egashira, S., and Jin, H. S. (1999). Numerical simulation of alternate bar formation. In *Proc. 7th Intl. Symposium on River Sedimentation*, Hong Kong, 733-738.

Thornton, E. B. and Guza, R. T. (1983). Transformation of wave height distribution. *Geophys. Res.*, **88**, 5925–5938.

Uchijima, K. (1990). Characteristic deformation of alternate bars due to low flow. In *Proc. of the 1990 National Conf., Hydraulic Eng.*, San Diego, 287-292.

van Rijn, L. C. (1989). Handbook of sediment transport by currents and waves. Technical Report H 461, Delft Hydraulics, Delft, The Netherlands.

Van Dongeren, A. R. and Svendsen, I. A. (1997). An absorbing-generating boundary condition for shallow water models. *Journal of Waterway, Port, Coastal and Ocean Engineering*, **123**, 303–313.

Wright, L. D. and Short, A. D. (1984). Morphodynamic variability of surf zome and beaches: A synthesis. *Marine Geology*, **56**, 93–118.